

NORWEGIAN UNIVERSITY OF LIFE SCIENCES



Preface / Forord

Design av maskinen omtalt i denne masteren, som har gått parallellt med skrivingen av denne masteroppgaven, er et prosjekt med støtte fra OREEC og UMB. Staben i Resonator AS har utført beregninger og simuleringer i designprosessen, og har alltid vært tilgjengelig for mine spørsmål. De har lært meg enormt mye, og det har vært en berikelse for meg å diskutere og jobbe med dem. Brorparten av innholdet i denne masteroppgaven har jeg lært det siste halve året, og mesteparten av det jeg har lært er ikke nevnt i denne teksten. Jeg vil takke Pingju Li, Christopher Grinde og André Dahl Jacobsen for mentorering, korrekturlesning og diskusjoner. Svein Hestevik fortjener en ekstra takk for å ha introdusert meg til et spennende og kunnskapsrikt miljø, og gitt meg muligheten til å arbeide heltid med dette prosjektet.

Tusen takk til hovedveileder Petter H. Heyerdahl. Jeg leste i sin tid et intervju med P.H.H. i Morgenbladet. Innholdet fikk meg til å ringe han og spørre om utdanningstilbudet ved UMB. Samtalen var interessant og inspirerende, som de jevnlige samtalene vi har hatt siden også alltid har vært. Nå, fem år senere, leverer jeg denne masteroppgaven i fagretning miljøfysikk og fornybar energi.

Takk til Pål From for kyndig blick på mine teorier, og takk til Håkon Matre Aasarød for vennskap og hjelp med design.

Stemningen på lesesalen har vært strålende, spesielt den siste tiden. Tusen takk, kamerater, for tips og støtte, for lunsjer og middager, for kaffe og endelig champagne. Dere er mange; ingen nevnt og ingen glemt.

Kjære Kari. Tusen takk for all støtte og hjelp, for tålmodighet og forståelse, for at du er deg.

Familien Bostad stiller opp for meg. Det har dere alltid gjort. Tusen takk, jeg gleder meg til å tilbringe mer tid med dere til sommeren.

Ås, 15.05.2011

Anders Bostad

Abstract

A resonating tubular free-piston synchronous permanent magnet linear machine with gas springs, known as “prototype 2B”, has been designed in collaboration with Resonator AS. This combination of an electric linear machine and gas springs shows promising theoretical results for the intended application: A novel method of creating strong vibrations with high frequency. The intention of building prototype 2B is to contribute to the development of a hammer drill system, suitable for drilling in hard rock formations.

This thesis describes the main characteristics of the machine design, and discusses alternatives to the chosen topology. Performance parameters of 2B are analytically derived, and found suitable for exploring the effects of increasing hammer frequency in hard rock hammer drilling.

An important contribution of this thesis is a new theory, applicable for simple and effective analyses of the mechanical motion of two moving objects in 2B; piston and stator. The theory is defined for an ideal no-load situation with no external influence.

A moving mass equivalent, defined as a function of piston- and stator mass, is suggested and theoretically substantiated. Comparison to results from numerical simulations validates this model for the no-load ideal case.

This theory is applicable for directly relating acceleration, velocity and displacement of piston and stator, to the masses of the two objects. The moving mass equivalent is useful for easily calculating important performance properties, such as hammer amplitude, system energy and resonance frequency.

Table of contents

<u>Preface / Forord</u>	1
<u>Abstract</u>	2
<u>Table of contents</u>	3
<u>Nomenclature</u>	7
<u>1 Introduction</u>	12
<u>2 Scope</u>	15
<u>3 Background theory</u>	16
3.1 Relations of sinusoidal movement	16
3.2 Back-iron.....	17
3.3 Lorentz' force	17
3.4 Varying B -field power loss theory	18
3.4.1 Magnetic saturation – hysteresis losses	18
3.4.2 Eddy currents	19
3.5 DC resistance	19
3.7 AC resistance	20
3.7.1 Skin effect.....	20
3.7.2 Proximity effect	20
3.7 AC / DC resistance in rectangular conductors	21
3.8 Drilling.....	21
3.9 Gas springs.....	22
3.9.1 Force exerted by an ideal gas spring	22
3.9.2 Non-linearity of gas springs	23
3.9.3 Force exerted by dual gas springs	23
3.9.4 Resonance frequency of a free-piston gas spring system	24
3.10 The Resonator concept and prototypes	25
3.10.1 Patents	25
3.10.2 System presentation	25
<u>4 Description of the 2B design</u>	30
4.1 Reference hammers	30
4.2 Design requirements	31
4.2.1 Frequency and energy per blow	31
4.2.2 Thrust force requirement.....	32
4.3 Initially set parameters.....	32

4.4	Electromagnetic design	33
4.4.1	Permanent magnets	34
4.4.2	Back-iron	34
4.4.3	Magnet piston iron	37
4.4.4	Main copper coils	37
4.4.5	Sensor coils.....	39
4.4.6	Single phase module analysis	40
4.5	Gas springs.....	46
4.5.1	Initial low pressure test	46
4.5.2	Gas spring design for 2B	46
4.6	Assembly of 2B	50
4.6.1	Piston assembly	50
4.6.2	Stator assembly	52
4.6.3	Gas spring assembly	56
4.6.4	System assembly	56
4.7	New and adjusted machine parameters	57
5	<u>System analysis and performance expectations</u>	59
5.1	Power loss and efficiency calculations	59
5.1.1	Copper losses	59
5.1.2	Iron losses.....	60
5.1.3	Magnet piston friction loss	60
5.1.4	Heat transfer	61
5.1.5	Gas spring losses.....	61
5.1.6	Total power loss as a function of stator current.....	62
5.1.7	System efficiency.....	63
5.2	Force output	64
5.2.1	Stator current	64
5.2.2	Induced voltage and stator voltage	65
5.2.3	Thrust force	66
5.2.4	Energy pr blow.....	66
5.2.5	Mechanical power output	66
5.2.6	Hole-size	67
5.3	Moving mass equivalent theory	68
5.3.1	Initial assumptions.....	68
5.3.2	Analogy.....	69
5.3.3	Statement.....	69
5.3.4	Mathematical proof.....	69
5.3.5	Analytical verification	71
5.3.6	Some parameters decided by application of the mass equivalent theory	72
5.4	Resonance frequency simulation	73
6	<u>Discussion.....</u>	75
6.1	Mechanical design	75

6.2	Electromagnetic design	76
6.3	Moving mass analysis	77
7	<u>Conclusion</u>	<u>78</u>
7.1	Design and assembly	78
7.2	Performance	78
7.3	Applicable analysis method	78
7.4	Epilogue - Further work	79
	<u>Reference list</u>	<u>80</u>
	<u>Appendices</u>	<u>83</u>
A	Basic theory	83
A.1	Newton`s 2. law	83
A.2	Newton`s 3. law	83
A.3	Friction force	83
A.4	Work, power and force.....	84
A.5	Magnetic flux density	84
A.6	Biot-Savart law	84
A.7	Ohm`s law for magnetic circuits	85
A.8	Magnetic permeance and reluctance.....	85
A.9	Faraday`s law.....	85
A.10	Electric linear machines.....	85
A.11	Lenz` law.....	86
A.12	Voltage induced in a conductor.....	86
A.13	Fill factor.....	86
A.14	Efficiency	87
A.15	Hooke`s law	87
A.16	Definition of pressure.....	87
A.17	Heat transfer	87
B	Calculations	88
B.1	Gas spring area increase:.....	88
B.2	Gas spring piston area difference:.....	88
B.3	Moving mass equivalent.....	88
B.4	Hammer amplitude	89
B.5	Maximum stator acceleration	89
B.6	Copper fill factor.....	89
B.7	Copper coil DC resistance	89
B.8	AC / DC resistance	90
B.9	Mid section casing outer surface.....	90
B.10	Gas spring surface	90
B.11	Gas spring max temperature.....	91
B.12	Stator mass.....	92
B.13	Piston mass.....	92
B.14	Gas spring pressures, constant amplitude 15.9 mm and frequency 100 Hz.....	93

B.15	Efficiency calculations, nominal case.....	93
C	List of tables and figures.....	94
D	Figures	95
D.1.	Induced voltage	95
D.2	Resonance frequency for different initial pressures	Error! Bookmark not defined.
D.3	Resonance frequency for different gas spring chamber lengths	Error! Bookmark not defined.
D.4	Performance chart.....	Error! Bookmark not defined.
E	Script.....	96
E.1	Analytical script of 2B motion by Grinde (2011).....	96

Nomenclature

Symbol	Explanation	Unit
$(\dot{\quad})$	Flow accent	-
$(\bar{\quad})$	Average accent	-
$(\vec{\quad})$	Vector accent	-
a	Acceleration	m/s^2
a_{max}	Maximum acceleration	m/s^2
a_p	Piston acceleration	m/s^2
a_{rel}	Relative acceleration	m/s^2
a_s	Stator acceleration	m/s^2
A	Area	m^2
A_c	Coil area	m^2
A_G	Air gap area	
A_{GSP}	Gas spring piston area	m^2
A_{GSS}	Gas spring surface area	m^2
A_h	Hole area	m^2
B	Magnetic flux density	T
B_r	Remanent magnetic flux density	T
B_G	Air gap magnetic flux density	T
B_I	Back-iron magnetic flux density	T
B_{rad}	Radial magnetic flux density	T
B_x	Axial magnetic flux density	T
d	Depth	m
e	Emissivity, $0 < e < 1$	-
E	Energy	J
\dot{E}	Energy flow	W
E_b	Energy per blow	J
E_{in}	Input energy	J
E_{loss}	Energy loss	J
E_{out}	Output energy	J
f_h	Hammer frequency (mechanic)	Hz
f_{el}	Electric frequency	Hz
F	Force	N
f	Variabel force	N
F_{AM}	Magnetic attraction force	N
F_d	Damping force	N
F_L	Lorentz' force	N
F_{MMMS}	Magnetomotive force	A
F_{RM}	Magnetic repelling force	N
F_T	Thrust force	N

Symbol	Explanation	Unit
G	Global reference frame	-
h	Conductor wire height	m
H	Magnetic field strength	A/m
i	Stator AC current	A
I	Stator DC current	A
I_{EC}	Eddy current	A
j	AC current density	A/m ²
J	DC current density	A/m ²
J_S	Surface current density	A/m ²
k_C	DC / AC resistance factor	-
k_{comp}	Gas spring compression factor	-
k_S	Spring stiffness constant	N/m
k_T	Thermal conductivity	W/mK
K_T	Heat transfer per area and ΔT	W/m ² K
L	Machine length	m
l_C	Copper wire length of one coil	m
l_{EM}	Length of electromagnetically active machine	m
l_{TOT}	Total length of copper wire	m
m_{EQ}	Mass equivalent	kg
m_P	Piston mass	kg
m_S	Stator mass	kg
n_C	Number of coils	-
n_m	Number of magnets	-
n_t	Number of turns pr coil	-
P_{EC}	Eddy current power loss	W
P_{in}	Input power	W
P_L	Power loss	W
$P_{L,C}$	Copper power loss	W
$P_{L,EM}$	Electromagnetic power loss	W
$P_{L,GS}$	Gas spring power loss	W
$P_{L,I}$	Iron power loss	W
P_m	Permeance (magnetic property)	H
P_{out}	Output power	W
p_0	Initial pressure	MPa
p_A	Ambient pressure	MPa
p_{GS}	Gas spring pressure	MPa
p_{max}	Maximum pressure	MPa
Q	Heat transfer	J
Q_C	Heat transfer from casing	J
r	Radius	m
R_{AC}	AC resistance	Ω
R_{DC}	DC resistance	Ω

Symbol	Explanation	Unit
R_{el}	Resistance (electric property)	Ω
R_m	Reluctance (magnetic property)	A/Wb
R_{TOT}	Total stator resistance	Ω
R_u	= 8.314. Universal gas constant	J/(mol · K)
S	Stator reference frame	-
t	Conductor wire thickness	m
T	Time period	s
T_A	Ambient temperature	K or C°
T_{GS}	Gas spring temperature	K or C°
T_{max}	Maximum temperature	K or C°
u	Voltage, variable	V
U	Voltage, constant	V
U_N	Nominal voltage	V
U_R	Voltage drop over resistance R_{el}	V
U_X	Voltage drop over reactance X	V
\vec{v}	Velocity	m/s
v	Speed	m/s
v_{max}	Maximum speed	m/s
v_p	Piston speed	m/s
v_{rel}	Relative speed	m/s
v_s	Stator speed	m/s
V	Volume	m ³
V_0	Initial gas spring chamber volume	m ³
V_C	Copper coil volume	m ³
V_G	Air-gap volume	m ³
$V_{\bar{G}}$	Min. gas spring chamber volume	m ³
W	Work	J
x_c	Critical displ. of gas spring piston	m
x_{GSC}	Gas spring chamber length	m
x_{max}	Amplitude	m
x_p	Piston displacement	m
x_{rel}	Relative (internal) displacement	m
x_s	Stator displacement	m
$x(t)$	Displacement along machine axis	m
\emptyset_{mi}	Magnet inner diameter	m
\emptyset_{mo}	Magnet outer diameter	m
\emptyset_{bi}	Back-iron inner diameter	m
\emptyset_{bo}	Back-iron outer diameter	m
\emptyset_c	Casing diameter	m
\emptyset_h	Hole diameter	m

Symbol	Explanation	Unit
γ	Polytrophic coefficient	-
δ	Skin depth	m
ε	Induced voltage	V
ε_{peak}	Induced voltage, peak-value	V
ε_{rms}	Induced voltage, rms-value	V
η	Efficiency	-
η_E	Energy efficiency	-
η_P	Power efficiency	-
μ	Permeability	H/m
μ_f	Friction coefficient	-
μ_0	$= 4\pi \cdot 10^{-7}$. Magnetic constant	H/m
μ_r	Relative permeability	-
ρ	Resistivity, electric	Ωm
σ	$= 5.6703 \cdot 10^{-8}$. Stefan`s constant	$\text{W}/\text{m}^2\text{K}^4$
τ_m	Magnet pitch	m
τ_C	Coil pitch	m
τ_p	Pole pitch	m
τ_f	Magnet separator pitch	m
Φ	Magnetic flux	Wb
ω	Angular frequency	s^{-1}

Abbreviation	Explanation	Unit
2B	The Resonator prototype described in this master thesis	
Back-iron	Magnetic material (Ch. 3.2)	
DCF	Dynamic chip formation (Ch. 3.8)	
DTH	Down-the-hole, drilling method (Ch. 3.8)	
MSE	Mechanical specific energy (Ch. 3.8)	J/m ³
NdFeB	Neodymium-iron-boron	
No 2	Former Resonator prototype	
O-ring	Mechanical gasket, torus-shaped	
PEEK	Polyether ether ketone	
ROP	Rate of penetration (Ch. 3.8)	m/h
SMC	Soft magnetic compound. Back-iron material.	
SmCo	Samarium cobalt	
UMB	Norwegian University of Life Sciences	
WOB	Weight on bit (Ch. 3.8)	

1 Introduction

In the search for low emission energy sources, geo-thermal energy has been increasingly actualized as an alternative. Geo-thermal energy can be defined as heat stored in the earth's crust, generated by convection from the earth's core and local decay of radioactive isotopes. The average temperature increase per km depth is 20 - 30 °K. In Norway, the earth surface emits an average power of 40 - 65 mW/m². The world wide average is approx. 80 mW/m² (Evensen et al., 2010).

Part of this flow of geo-thermal energy can be utilized, for production of electricity and for direct use, i.e. heating and cooling. The main advantages are:

- Generally good availability.
- Supply stability, independent of seasonal and local meteorological variation.
- Minimal local environmental impact.
- Minimal emission of greenhouse gases.

World-wide annual production from geo-thermal sources is 67 TWh electric energy and 122 TWh heating / cooling energy (Evensen et al., 2010). The world geo-thermal technical potential for identified geothermal sources is estimated by Stefansson (2005). 3.5 % of the electricity generation potential, and 0.2 % of the potential direct use was already utilized. The technical potential amounts to more than half the world-wide annual energy consumption of today.

To increase the profitability of using geo-thermal energy as an energy source, the main technological challenges are (Evensen et al., 2010):

- Mapping of temperatures and potential heat reservoirs.
- Decreasing the cost of deep drilling in hard bedrock.

Rotary drilling has proven effective for deep-hole drilling, and is the preferred method for the oil and gas industry in the North Sea. For hard, abrasive rock formations, the universal rotary cutting method shows a low rate of penetration (ROP) and high mechanical specific energy (MSE), resulting in high time consumption and cost (Bartnik, 2006). Hiring of drill rigs constitute 37 % of the total cost in drilling operations on the norwegian continental shelf (Åm et al., 2010). Saving time is essential for decreasing the costs, and to make geo-thermal energy sources a competitive alternative for heating and production of electric power.

Another method of deep-hole drilling is the down-the-hole (DTH) percussion drilling method. This method requires a down-hole piston, often driven by a pressurized drill fluid, to hit a

drill bit in contact with the rock. Each blow to the rock must transfer sufficient energy to fracture the rock; the dynamic chip formation (DCF). Rotation increases efficiency by not allowing the bit inserts to hit the same spot in subsequent blows. The cuttings are transported to the surface by means of the drill fluid. See theory background chapter for conceptual clarifications.

Several studies show that percussion drilling can increase ROP in hard rock formations (Han et al., 2005) (Teodurio and Cheuffa, 2011). Also, less contact time with rock decreases the drill bit abrasion, leading to an increased life time and decreased service time, contributing to increase the overall ROP further.

Topelian (1958) stated more than 50 years ago that increasing hammering frequency and maintaining a sufficient energy pr blow increases ROP. Green et.al (2005) supports this statement:

It also appears that impacts great enough to exceed the cutter DCF force are critical, but that greater impacts are less effective, since much less rock breakage occurs for increasing loads. It is expected that once the DCF force is reached, better use of energy can be made by increasing the blows per minute (Green et al., 2005).

From these arguments it can be suggested that adaptive impact load limitation will increase bit life time, and that increasing the hammering frequency will result in an increased ROP and a decreased MSE. It is a fair assumption that a hammer drill with such performance ability will substantially decrease the cost of deep-hole drilling.

The concept of a resonating linear electric synchronous permanent magnet machine with gas springs can provide a solution for further enhancement of the advantages of DTH percussion drilling. This thesis presents the possibility of building a hammer drill that will be able to deliver hammering frequencies exceeding 100 Hz, while still transferring sufficient energy pr blow to cause rock fracture.

In general, electric machines are characterized by the possibility of high torque/force, precision, efficiency and adaptability. These properties are valuable tools for realizing a hammer drill as discussed. Linear electric machines have been made since the 1840`s (Laithwaite, 1975), and the concept of gas springs is also well tested. The combination of these is not common. The basic concept of such a machine is that the electromagnetic part of the machine provides efficient energy conversion and high power, while the gas springs constitute a compact storage of energy. Using this combination of properties, it should be possible to provide a sufficient mechanical energy transferred to the rock, and repeat this action with high frequency.

The patented Resonator concept describes an industrial vibrator; an electromagnetically active piston moving between two gas springs. Several prototypes have been made, and

several applications have been discussed, the hammer drill being one of them. This thesis describes the next step in the Resonator high frequency drill hammer project; the design of the Resonator prototype 2B.

Concept-proving Resonator prototypes have previously been made and tested. Simulations and testing have proved several important properties of the Resonator concept:

- Short term energy storage in mechanical springs.
- Resonance of the piston between two mechanical springs with a frequency mainly influenced by the spring stiffness.
- Electromagnetic energy transfer between coils and permanent magnet piston helps to maintain and reinforce the resonant behavior.
- The ability to remain in resonance during drilling operation.

2B is an evolution of the prior prototypes. The design of 2B is conducted in a team consisting of the staff of Resonator AS. The emphasized design criteria, in a prioritized order, are:

- Develop gas springs to increase the hammering frequencies.
- Perform a mechanical power output sufficient to break rock.
- Enhance the efficiency of the electromechanical energy transfer and minimize heat development.
- Design the interior and chassis to withstand the forces involved in accelerating the moving mass and impacting a rock surface.
- Approach a power density comparable to existing hammer drill systems used in the drilling industry.

2 Scope

The scope of this thesis is to connect the design process to the subsequent building and testing of the 2B prototype.

This can be described in six main parts:

- Present the Resonator concept and describe how a drill hammer can be developed based on it.
- Describe the collaborative design process:
 - Define target parameters.
 - Present machine components and discuss topological issues.
 - Discuss alternative machine components of interest.
- Suggest methods for machine assembly based on knowledge of the machine design.
- Present how resonance frequency and mechanical power output can be analytically predicted.
- Estimate parameters for an assumptive performance chart, for guidance to dimensioning of test equipment.
- Suggest methods for analyzing relevant parameters.

3 Background theory

The theory and conceptual clarifications presented in this chapter are considered essential for understanding the relations and discussions presented in this thesis. Relevant basic theory is included in appendix A.

3.1 Relations of sinusoidal movement

A sinusoidal movement in x -direction with the amplitude x_{max} can be expressed as displacement:

$$\vec{x}(t) = x_{max} \sin(\omega t) \quad (3-1)$$

Velocity $\vec{v}(t)$ is found by differentiating displacement:

$$\vec{v}(t) = \frac{d\vec{x}(t)}{dt} = \omega x_{max} \cos(\omega t) = v_{max} \cos(\omega t) \quad (3-2)$$

Displacement and velocity can be related as:

$$\begin{aligned} \frac{\vec{x}(t)}{\vec{v}(t)} &= \frac{x_{max} \sin(\omega t)}{\omega x_{max} \cos(\omega t)} = \frac{\sin(\omega t)}{\omega \cos(\omega t)} \\ \rightarrow \vec{x}(t) &= \vec{v}(t) \frac{\tan(\omega t)}{\omega} \end{aligned} \quad (3-3)$$

Acceleration $\vec{a}(t)$ is the time derivative of velocity. This relates acceleration, velocity and displacement:

$$\vec{a}(t) = \frac{d\vec{v}(t)}{dt} = -\omega^2 x_{max} \sin(\omega t) = -\omega^2 \vec{x}(t) \quad (3-4)$$

The maximum values are related by:

$$\begin{aligned} \vec{v}(t) &= v_{max} \cos(\omega t) = \omega x_{max} \cos(\omega t) \\ \vec{a}(t) &= -a_{max} \sin(\omega t) = -\omega v_{max} \sin(\omega t) \\ \rightarrow a_{max} &= \omega v_{max} = \omega^2 x_{max} \end{aligned} \quad (3-5)$$

3.2 Back-iron

Back-iron consists of a material with high magnetic permeability μ , hence a conductor of magnetic fields. In electric machine design it is used to control the magnetic field path, and minimize the drop in magnetomotive force F_{mmf} .

3.3 Lorentz' force

An electrical wire of length l carrying the current \vec{I} in a magnetic field with the field density \vec{B} experiences the Lorentz' force \vec{F}_L (Wildi, 2006):

$$\vec{F}_L = \vec{B} \times \vec{I} \cdot l \quad (3-6)$$

The direction of the force is a result of the direction of the right hand rule, as shown in figure 3-1. In this figure, the velocity v ($= \vec{v}$) is analogous to the flow of positive charge in the conducting wire.

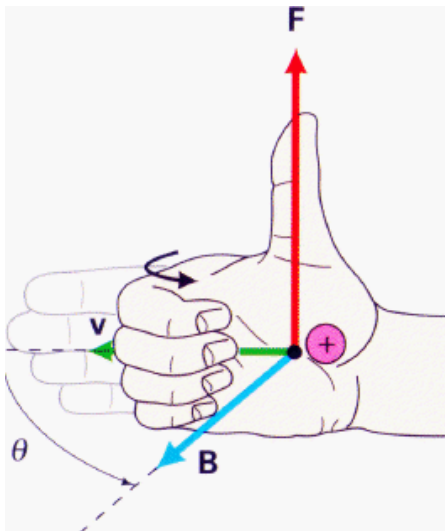


Figure 3-1 Right hand rule (brinkster.com)

3.4 Varying \vec{B} -field power loss theory

3.4.1 Magnetic saturation – hysteresis losses

To achieve a desired flux density $\vec{B} = \mu\vec{H} = \phi/\hat{n}A$ (see appendix A.5), the cross section area A of part of the magnetic path can be adjusted. The flux should be dense to optimize the force density, but not to a significant degree of saturation.

In the saturated state, an increase in the magnetic field strength \vec{H} does not increase the magnetic flux density \vec{B} in a given area of the magnetic material. The consequence of saturation is increased hysteresis losses. \vec{H} is increased and decreased by supplying current to a coil wire around an iron bar. The B - H -curve is then plotted, as in figure 3-2.

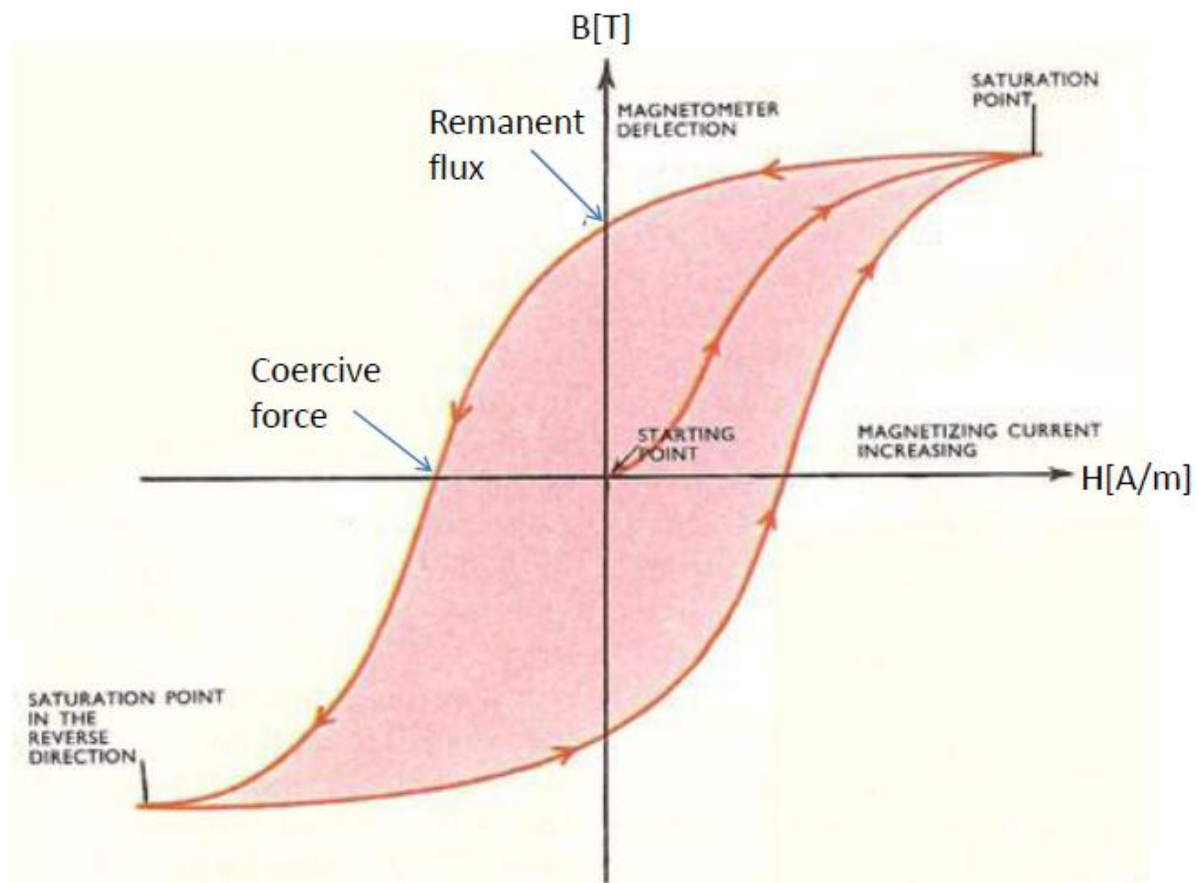


Figure 3-2: Hysteresis loss B-H-curve. The area between the magnetizing curve and the demagnetizing curve represents the hysteresis energy loss in joules (daviddarling.info, 2011).

The magnetic orientation of the iron turns according to the frequency. Increasing \vec{H} magnetizes the iron. When decreasing \vec{H} a remanent flux remains in the iron, and the iron

piece is at this point a magnet in itself. Increasing \vec{H} towards zero, the flux density is reduced to zero by means of the coercive force. At this point, the iron is fully demagnetized.

The hysteresis power loss is represented by the area of the B - H loop for every period. Hence; hysteresis losses are proportional to frequency. Typically for materials used as back-iron, local extreme values approaching 2 T would call for a design review (Hanselman, 2006).

3.4.2 Eddy currents

Eddy currents occur as a result of varying magnetic fields inducing uneven voltage potentials in electrically conducting materials, as stated in Faraday's law. If the material has a low electric resistivity $\rho = R_{el} \cdot A/l$ (see appendix A.9), big currents $I = U/R_{el}$ will flow in the plane perpendicular to the varying magnetic field, in a direction as to oppose the magnetic flux change (Lenz's law, appendix A.11). These currents produce heat as electric power loss $P_{EC} = I_{EC}^2 R_{el}$, at the expense of the magnetic flux density (Wildi, 2006, Tipler and Mosca, 2008).

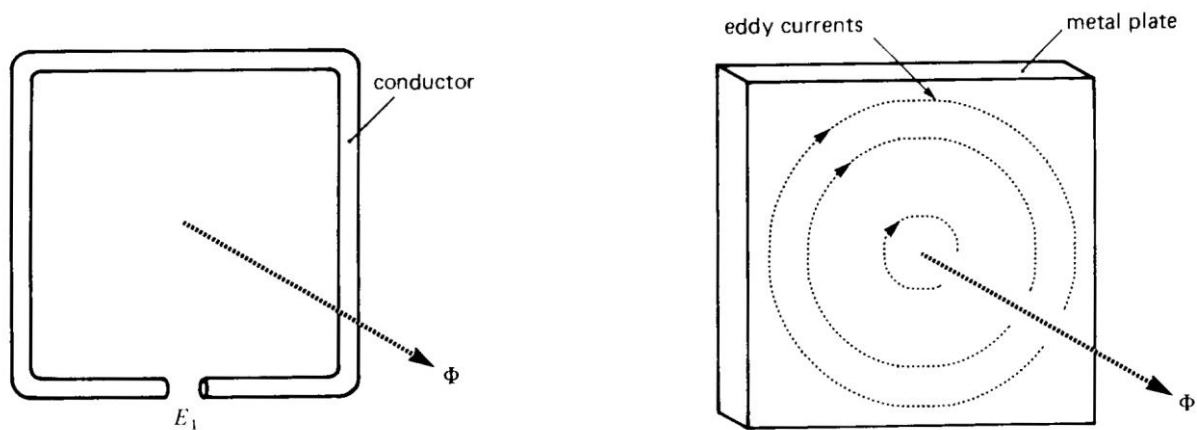


Figure 3-3: Eddy currents, induced by a varying magnetic field, in an electrically conducting metal plate (Wildi, 2006).

3.5 DC resistance

The DC resistance R of a conductor is simply given by conductor resistivity ρ and the cross-section area A and length l of a conductor (Hanselman, 2006):

$$R_{DC} = \rho \cdot l/A \quad (3-7)$$

For copper coils, the conductor resistivity is typically $1.7 \cdot 10^{-8} \Omega\text{m}$, with a temperature coefficient of $3.9 \cdot 10^{-3} \text{K}^{-1}$. Copper is the only conductor material considered during the work of this thesis.

3.7 AC resistance

The AC resistance is the additional resistance experienced when applying an alternating current to the same conductor. It can be related to DC resistance with the factor k_C , adding the effects of alternate current:

$$R_{DC} = k_C R_{AC} \quad (3-8)$$

k_C depends on current frequency, magnetic permeability of the conductor material, conductor thickness and neighboring conductors. The resulting total resistance R_{TOT} is then:

$$R_{TOT} = R_{DC} + R_{AC} = R_{DC} \cdot (1 + k_C) \quad (3-9)$$

3.7.1 Skin effect

The skin effect is due to opposing eddy currents induced by a variable magnetic field resulting from an alternating current in the conductor. The current is denser at the surface of the inductor, with the value J_S . The current density J decreases exponentially with depth d :

$$J = J_S \cdot e^{-d/\delta} \quad (3-10)$$

δ is the skin depth, defined as the depth below the conductor surface that the current density is at $1/e \approx 0.37$ of the value at the conductor surface J_S . A good approximation, depending on conductor resistivity ρ , angular frequency ω and the magnetic constant μ_0 is:

$$\delta = \sqrt{2\rho/\omega\mu_0} \quad (3-11)$$

In other words, the effective resistance of the conductor core increases, yielding an increased total resistance.

3.7.2 Proximity effect

Alternating currents in a conductor yields an alternating magnetic field surrounding the conductor. This causes additional skin effect and eddy currents in adjacent conductors, altering the current density distribution and increasing the AC resistance (Nilssen, 2008).

3.7 AC / DC resistance in rectangular conductors

Hanselmann (2006) derives an approximation for calculating the AC resistance component R_{AC} of the total resistance compared to DC resistance component R_{DC} in a rectangular wire, depending on conductor skin depth δ , thickness t and height h :

$$k_C = \frac{R_{AC}}{R_{DC}} = \left(\frac{t \cdot h}{3 \cdot \delta^2} \right)^2 \quad (3-12)$$

The AC resistance component occurs due to a sinusoidal variable magnetic field in the y -direction (Figure 3-4).

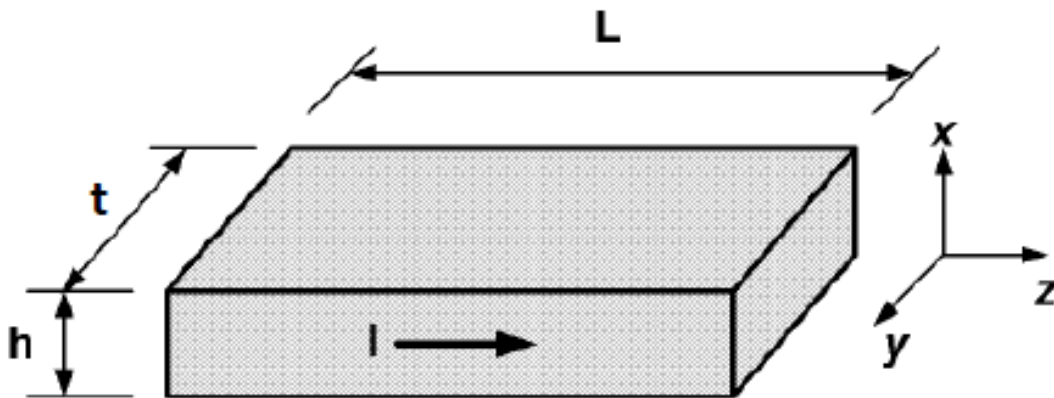


Figure 3-4: Rectangular conductor geometry for calculating AC resistance (El Shahat et al., 2010).

3.8 Drilling

Dynamic chip formation (DCF) is the required impact load for rock deformation and breakage (Green et al., 2005).

The down-the-hole (DTH) hammer drilling method uses a down-hole drill hammer to deliver mechanical energy directly to the back-side of the drill bit.

Mechanical specific energy (MSE) is the energy used to remove a volume of rock, measured in Joule / cubic meter.

Rate of penetration (ROP) is the speed at which a drill penetrates rock and deepens the borehole, measured in meters / hour.

Weight on bit (WOB) is the average force pushing the drill bit towards the rock. The minimum value must exceed the return force from the blows to the drill bit.

3.9 Gas springs

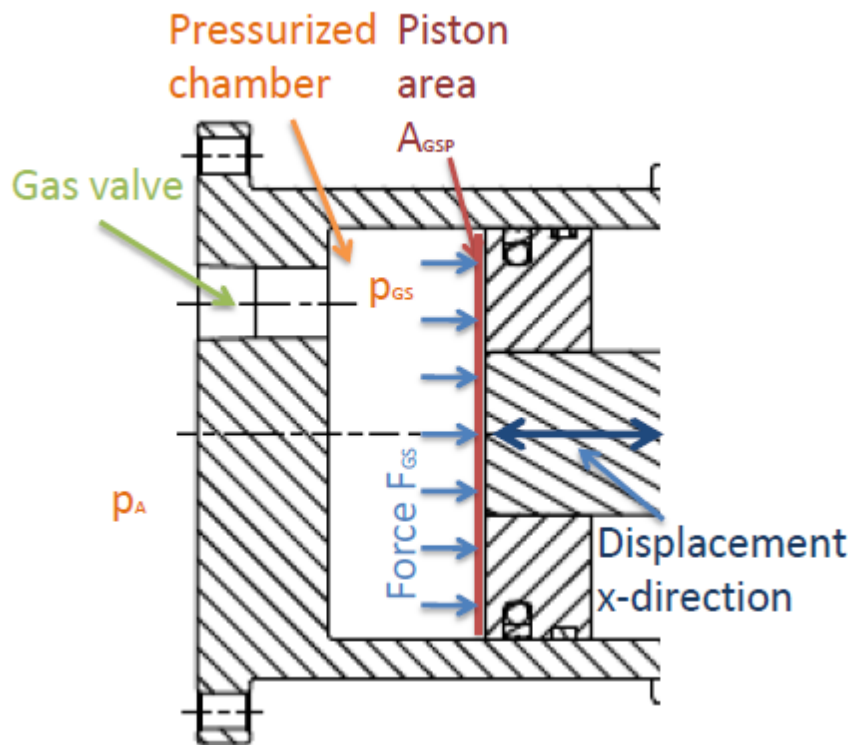


Figure 3-5: Gas spring topology. Piston displacement yields compression / expansion of the gas inside the chamber. The vacant gas volume behind the gas spring piston is ignored in this presentation.

3.9.1 Force exerted by an ideal gas spring

In an ideal gas spring there are no leakages, no heat transport and perfect stirring of the working gas. The piston acts with an effective area A_{GSP} , to compress the gas contained in the chamber. In this example, A_{GSP} is a constant. The pressure inside the gas spring chamber p_{GS} compared to the ambient pressure p_A increases, and the gas spring force F_{GS} exerted on the gas spring piston likewise (Lu and Chang, 2008):

$$F_{GS} = (p_{GS} - p_A)A_{GSP} \quad (3-13)$$

3.9.2 Non-linearity of gas springs

Gas springs show highly non-linear characteristics (Donahue et al., 2005). Considering the air variation in the gas springs as quasi-static adiabatic processes, this can be understood by using the ideal gas law (Tipler and Mosca, 2008):

$$pV = n_G R_U T \quad (3-14)$$

$R_U = 8.314 \text{ J / (mol} \cdot \text{K)}$ is the universal gas constant, equal for all gases.

Moving the piston compresses the n_G moles of gas contained in the gas spring chamber. The volume V decreases when work is done on the gas from the piston. Part of this energy yields an increase of the pressure p . The rest of the work done on the gas will be used for increasing the temperature T of the working gas. This is dependent on properties of the working gas, expressed as the polytropic coefficient γ . The quasi-static adiabatic process is described as (Tipler and Mosca, 2008):

$$pV^\gamma = \text{constant} \quad (3-15)$$

The result is a further increase of pressure, and a nonlinear relationship between piston displacement x and gas spring force $F_{GS}(x)$.

3.9.3 Force exerted by dual gas springs

The force exerted by two opposite and equal gas spring chambers with initial pressure p_0 on a piston area A_{GSP} , can be expressed as a function of displacement x on the x -axis. x_{GSC} is the length of the gas spring chamber (Zhang, 2009):

$$F_{GS} = A_{GSP} p_0 \left(\left[\frac{x_{GSC}}{x_{GSC}+x} \right]^\gamma - \left[\frac{x_{GSC}}{x_{GSC}-x} \right]^\gamma \right) \quad (3-16)$$

A typical example of a nonlinear dual gas spring characteristic is given in figure 3-6, which is based on simulations for an adiabatic system.

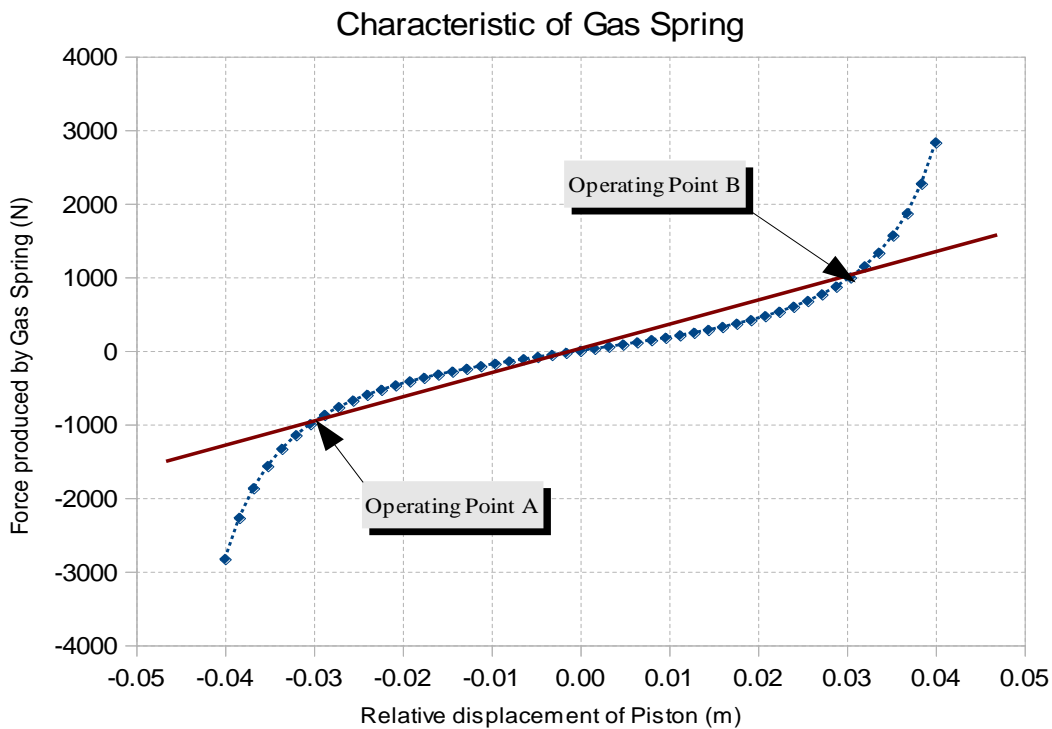


Figure 3-6: Example of a gas spring force versus amplitude characteristic (Li, 2011b).

Up to a certain displacement $\pm x_C$, between operating points A and B, the characteristic is close to linear. Exceeding these critical x -values yields a high temporary temperature increase and a strong increase in force produced by the gas spring F_{GS} .

3.9.4 Resonance frequency of a free-piston gas spring system

Free-piston machines move a piston between combustion- or gas spring chambers, with the advantage of low friction and high power density.

Xiao (2010) has derived an expression for the natural resonance frequency f_0 of a free-piston gas spring system, depending on the spring stiffness coefficient k_{GS} and the moving mass m :

$$f_0 = \frac{1}{2\pi} \sqrt{k_{GS}/m} = \sqrt{\left(\frac{1}{-\gamma+1}\right) \left(\frac{1}{2^\gamma} - 1\right) \left(\frac{p_0 \cdot A_{GSP}}{x_{max} \cdot m}\right)} \quad (3-17)$$

The non-linear spring stiffness coefficient k_{GS} is a function of the gas specific polytrophic coefficient γ , the initial pressure in equilibrium position p_0 , the piston area A_{GSP} and the oscillation amplitude x_{max} .

3.10 The Resonator concept and prototypes

3.10.1 Patents

A patent of August 2005 (Brennvall and Nilssen) describes an electromechanical converter of tubular shape with a permanent magnet translator effective towards a row of surrounding annular coils. Gas chambers on each end provide the means for the simplest forms of application; the vibration-driven generator and the vibration-enforced motor. An axial bar holds the piston elements in a free-piston design, or connects externally through one end for a fixed-piston or loaded-piston design.

3.10.2 System presentation

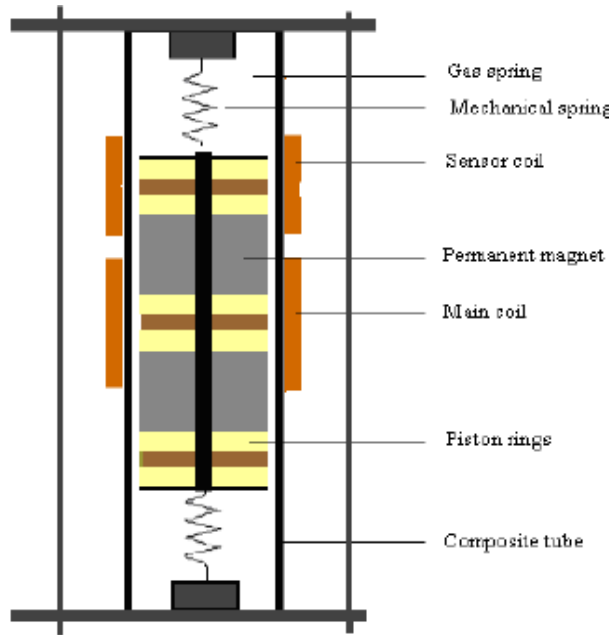
A generic prototype made in 2008, hereby called no 2, was analyzed by Jaillot (2008), Ummaneni (2009) and Zhang (2009). It defines the basic functioning principle and uses several of the same components as 2B. A presentation of no 2 will therefore serve as guidance to an understanding of the Resonator system.

3.10.2.1 Structure and operation principle

The basic structure and dimensions of no 2 is presented in figure 3-7 and table 3-1. No 2 is a tubular AC single-phase linear machine with two axial flux permanent magnets separated by Teflon rings and mounted oppositely on a rod of stainless steel. They produce a radial magnetic flux through the main coil. The radial magnetic field and the tangential current produce an axial Lorentz' force.

A sensor coil is wound in the same axial position as the end of the magnetically active piston. The movement of the magnet piston causes an induced voltage ϵ . The neutral point of the piston movement is the point of maximum speed and therefore the point of maximum magnetic flux change. In the outer positions of piston movement, the induced voltage equals zero, and the signal switches polarity. The resulting electric signal serves to analyze the movement of the piston quite accurately.

Both coils are mounted on a composite tube made from PEEK material, chosen for its machinability, tensile strength, thermal stability, low permeability and high electrical resistivity. The smooth surface minimizes the friction against the magnet piston, and o-rings against the end plate (not visible on the figure) seal the piston chamber from gas leakages.



Parameter	Value
Stator	
Total Machine Diameter	100.0 mm
Total Length of Machine	220.0 mm
Coil Inner diameter	26.0 mm
Coil outer diameter	31.0 mm
Coil length	40.0 mm
Number of Turns	507.0 mm
Conductor Diameter	0.4 mm
Electrical resistivity	$1.72 \times 10^{-8} \Omega \cdot m$
Peak Current density	14 A/mm^2
Rotor	
Length of Piston	110.0 mm
Length of Magnet	40.0 mm
Length of pole Pitch	50.0 mm
Outer diameter of magnet	45.0 mm
Inner diameter of magnet	6.0 mm
Flux density	1.2 T
Frequency	30 Hz

Figure 3-7: Basic structure of the no 2 prototype (Jaillot, 2008)

Table 3-1: Dimensions of the no 2 prototype. Mark: "Rotor" refers to the magnetic piston (Ummaneni et al., 2009)

On each end of the piston chamber are mechanical springs between the piston and the end plates. The stiffness of these springs yield the resonance frequency of the system to be 30 Hz (Ummaneni et al., 2009).

3.10.2.2 Positive feedback control system

An adjustable positive feedback loop can be created by using the signal from the sensor coil as an input signal to a low frequency range audio amplifier (< 200 Hz). The amplifier output is connected to the main coil. The motor is started by displacing the piston manually to induce an initial signal in the sensor coil, or sending an electric start impulse through the main coil. The system will then find a steady-state condition where the dissipated heat, radiation and eventual load balances the electric input power at a given amplitude and resonance frequency (Jaillot, 2008).

3.10.2.3 No load force analysis

The net axial forces acting on the free piston and the stator during no load operation can be expressed using Newton's second and third law (Tipler and Mosca, 2008, Ummaneni et al., 2008):

$$\vec{F}_{net,piston} = m_p \cdot \vec{a}_p = \vec{F}_{EMF} + \vec{F}_{spring} + \vec{F}_f = -\vec{F}_{net,stator} = -m_s \cdot \vec{a}_s \quad (3-18: \text{Force balance})$$

The forces of gravity will act on both the piston and the stator. An equal upward force is acting on the stator housing, from the suspension or a rig, offsetting gravity. Given a vertical

axis rig, the similar upward force acting on the piston will be a static component of the total spring force \vec{F}_{spring} . The gravity force will offset the piston, but only to a negligible degree. Simplified, the forces working on the piston are acting equally opposite on the stator.

3.10.2.4 Single cycle energy flow analysis

Adding a load to the system, by hitting on rock, will inflict abrupt disturbances to the harmonic stability of the no load state. The net energy flow, where $\dot{E} = \frac{dE}{dt}$, of one cycle under steady-state conditions is:

$$\dot{E}_{EMF} = \dot{E}_{rock} + \dot{E}_{spring} + \dot{E}_{kin} + \dot{E}_f + \dot{E}_{vibr} \quad (3-19: \text{One cycle net energy flow})$$

The two energy storages of the system, E_{spring} , and E_{spring} , periodically transfer the energy between storages two times pr cycle. However; the net energy flow to the gas springs, \dot{E}_{spring} , is equal to the heat transferred from the gas springs to the surroundings as a result of the compression and expansion of one cycle. Similarly, net flow of kinetic energy into the system in one cycle \dot{E}_{kin} is zero, and the energy absorbed in the piston movement is the energy dissipated as mechanical friction, \dot{E}_f . The vibration energy flow \dot{E}_{vibr} ends up as heat in the surrounding support structure that is being forced to vibrate. In a reasonably functioning drill hammer, these are all relatively small compared to the energy transferred to the rock, \dot{E}_{rock} . To be able to deliver the same amount of energy in every stroke, the energy transferred to the rock in one stroke must be replaced by the energy added electromechanically during the following period before the next stroke.

$$\dot{E}_{EMF} \geq \dot{E}_{rock} \quad (3-20: \text{Simplified energy flow relation})$$

Neglecting losses allows replacing \geq with $=$.

\dot{E}_{EMF} is the input energy flow \dot{E}_{in} subtracted the electromagnetic losses $\dot{E}_{EM,loss}$. For one cycle during steady-state operation, the hammer efficiency can be expressed in several ways:

$$\eta = \frac{\dot{E}_{rock}}{\dot{E}_{in}} = \frac{\dot{E}_{rock}}{\dot{E}_{EMF} + \dot{E}_{EM,loss}} = \frac{\dot{E}_{rock}}{\dot{E}_{rock} + \dot{E}_{spring} + \dot{E}_f + \dot{E}_{vibr}} \quad (3-21: \text{Hammer efficiency})$$

3.10.2.5 Resonant behavior

Another aspect of the load state is the system ability to remain in resonance. This depends on the available energy to move the piston and stator immediately after a blow. Simulations by Zhang (2009) suggest that the remaining potential energy in the gas springs and the kinetic energy of the free piston will allow the system to maintain its resonant behavior and

provide sufficient energy to repeat the collision in the next period. Zhang assumes inelastic collisions with no losses.

The graphic representation in figure 3-8 can only be considered an ideal case of the hammering operation mode. In the model, the casing velocity abruptly falls to zero when hitting the rock. All the kinetic energy is assumed transferred to the rock. As the simulation in figure 3-8 shows, the movement of the piston is not much affected by the system energy loss. The energy stored in spring compression and kinetic energy of the piston restarts the movement of the casing. The electromagnetic energy added equals the energy transferred to the rock. As a result, the system remains in resonance (Zhang, 2009).

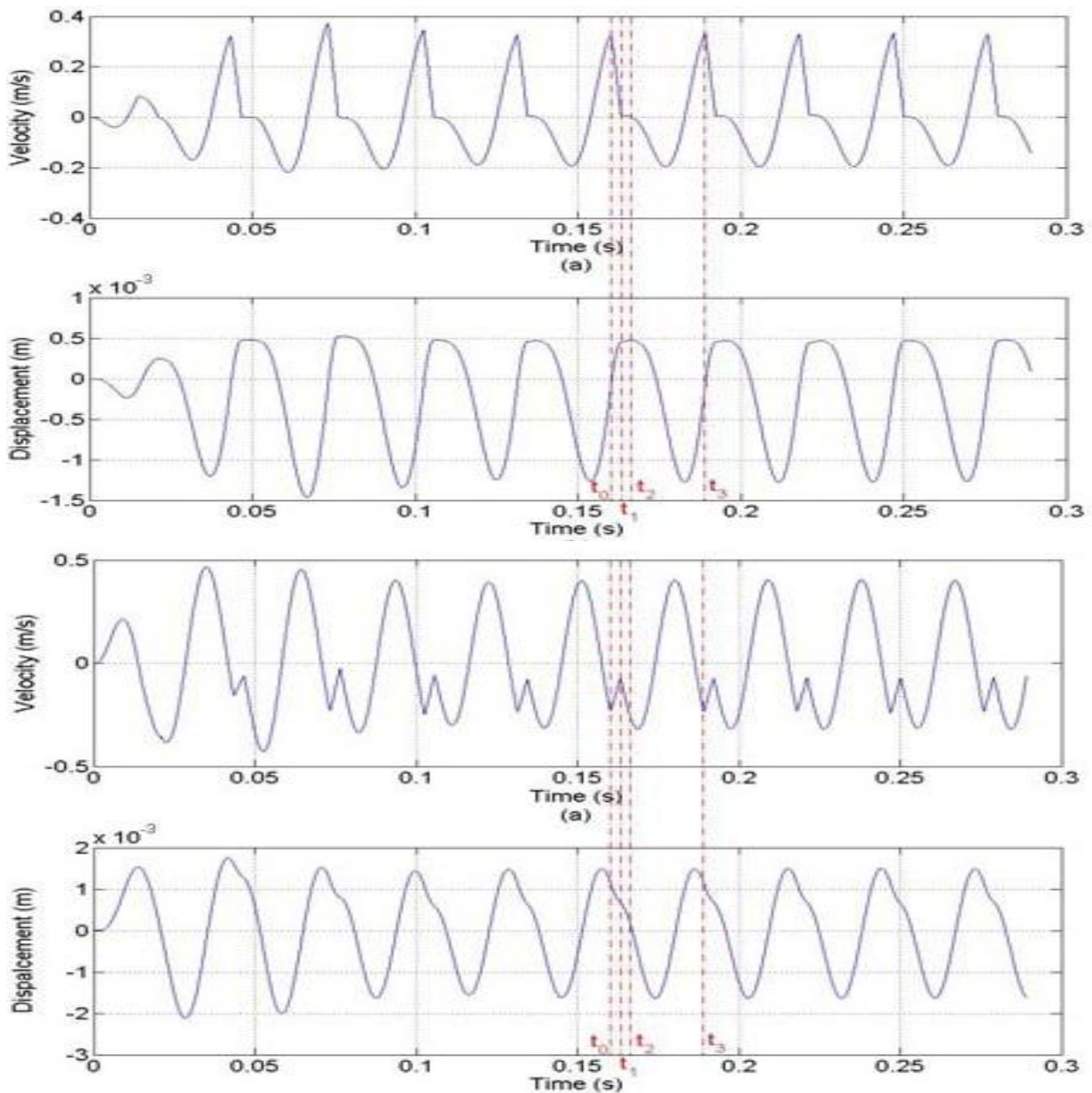


Figure 3-8: Simulation of the velocity and displacement of the casing (top) and the piston relative to casing (bottom) suggesting that prototype no 2 will be able to remain in resonance during load operation (Zhang, 2009).

The analysis indicates that there exists a critical relationship between the energy conserved in the system and the energy transferred pr blow. If the abrupt energy transfer drains the energy storage more than to a critical degree, the resonance frequency will be significantly affected. Such vibro-impact systems are studied elsewhere, one example is Luo (2007).

4 Description of the 2B design

The topology of no 2 has proven interesting, and a suitable base for the design of 2B. The operating principle has been proved, and the sensor coil signal is suitable for triggering a positive feedback loop. The theory presented in the previous chapter is essential for setting the initial criteria prior to the design process.

By adding additional magnets (n_m = number of magnets) to a longer rod, multiple radial magnetic fields corresponding to tangentially wound coils will increase the input power proportionally to the number of coils $n_c = n_m - 1$. Adding back-iron to encapsulate the coils and using iron in the pole separating pieces between the magnets will help increasing the power density. Realizing functioning gas springs will increase the energy density and the hammering frequency. Designing a powerful machine also presses the need to take material wear and mechanical / thermal stability into account. These are the main features distinguishing 2B from no 2.

The data sheet draft in appendix D.4 presents a system drawing of the 2B prototype. This chapter presents the design process; the background for choice of topology and machine parts, including alternatives. Details of material properties will also be presented.

4.1 Reference hammers

The Resonator concept should eventually be able to compete with conventional hammer systems. The Wassara concept is a DTH hammer system powered by high pressure water. The technical specifications for two of their smallest hammers are presented in figure 4-1. The targets for the design of Resonator 2B is to be comparable in size to Wassara W80, in performance to Wassara W50 (2009).



Wassara 50		Wassara 80	
Parameters	Value	Parameters	Value
Total machine length	895 mm	Total machine length	977 mm
Outer diameter	50 mm	Outer diameter	80 mm
Power output	7.5 kW	Power output	14 kW
Hammer frequency	75 Hz	Hammer frequency	65 Hz
Energy pr blow	100 J	Energy pr blow	210 J
Hole size diameter	60-64 mm	Hole size diameter	95 mm

Figure 4-1: Technical specifications for reference hammers: Wassara W50 and W80 .

An indication to the relation between energy per blow and bit diameter is found by analyzing the Wassara W50 through W150 hammers (2009). Dividing energy per blow by drill bit area, derived from hole-size, yields an average:

$$E_b/A_{db} = 0.04 \text{ J/mm}^2 \quad (4-1: \text{Energy per blow per drill bit area})$$

4.2 Design requirements

The target values for machine performance, stated in table 4-1, reflect and quantify the main goals mentioned initially. These are approximate target values, some set to match reference specifications. Others are set for practical reasons, such as availability of components. Some of the table values depend on other requirements, and these relations are clarified here.

4.2.1 Frequency and energy per blow

Energy pr blow E_b is the desired mechanical work transferred pr time period $T = 1/f$. P_{out} is the power output from the electromechanical energy conversion, averaged over one cycle:

$$E_b = \int_0^T P_{out} dt \rightarrow E_b = P_{out}/f \quad (4-2: \text{Energy pr blow})$$

By increasing the resonance frequency f at constant power, the energy pr blow will decrease. High hammering frequency is considered the primary design requirement, and will therefore be the preferred property to enhance. The target frequency is set to $f = 100$ Hz, outperforming the reference hammers. The power output is set to match Wassara 50: $P_{out} = 7,5$ kW. The target value for energy per blow is then:

$$E_b = P_o / f = \frac{7,5 \text{ kW}}{100 \text{ Hz}} = 75 \text{ J} \quad (4-3: \text{Energy pr blow})$$

4.2.2 Thrust force requirement

In a free piston engine, analyzed over one time period T , the variable thrust force f_L is acting on a total distance x of 4 times the amplitude; $4x_{max}$. Ignoring friction, the work done equals the energy pr blow. An averaged thrust force can be defined:

$$E_b = \int_0^{4x_{max}} f_T(x) dx \approx \bar{F}_T \cdot 4x_{max} \quad (4-4: \text{Averaged thrust force})$$

The maximum allowed top speed tolerated by the chosen dynamic seals is set to $v_{rel,max} = 10 \text{ m/s}$ by the manufacturer (Trelleborg, 2010). Hence, the maximum allowed relative amplitude between piston and stator is:

$$x_{rel,max} = \frac{v_{rel,max}}{\omega} = \frac{10 \text{ m/s}}{2\pi \cdot 100 \text{ Hz}} = 15.9 \text{ mm} \quad (4-5: \text{Maximum relative amplitude})$$

The average electromagnetic thrust force requirement for 2B is then:

$$\bar{F}_T = \frac{E_b}{4x_{max}} = \frac{75 \text{ J}}{63,6 \text{ mm}} = 1.18 \text{ kN} \quad (4-6: \text{Required force input})$$

Parameters	Symbol	Value	Comment
Total machine length	L_{2B}	< 1 m	Similar to ref. hammer W80.
Outer diameter	\varnothing_{2B}	~ 80 mm	Similar to W80, given by back-iron rings.
Power output	P_{out}	7.5 kW	Equal to ref. hammer W50.
Hammer frequency	f_h	> 100 Hz	Depends on stiff gas springs.
Energy pr blow	E_b	75 J	Comparable to W50. $E_b = P_{out} / f$
Phases		1	No 2 configuration, all coils connected in series.
Voltage	U	< 230 V	Drive unit requirement.
Average thrust force	\bar{F}_T	1.18 kN	$\bar{F}_{emf} = E_b / 4x_{max}$

Table 4-1: Target performance values for prototype 2B

4.3 Initially set parameters

Every process has a point of origin, and in this case the inventory list was a natural base. Using parts already owned by Resonator AS saves both cost and time, making the project possible in terms of budgets and deadlines. The available components assessed are:

- Axial flux neodymium-iron-boron (NdFeB) permanent magnets. Dimensions in mm:
 $\varnothing_i = 10 / \varnothing_o = 46.5 / \tau_m = 40$.

- Soft magnetic compound (SMC) rings as back-iron (See chapter 4.4.2.2). Dimensions in mm: $\varnothing_i = 62 / \varnothing_o = 70 / H = 25$.
- Rectangular DAMID two-layer insulation copper conductor wire. Dimensions in mm: $h = 2.35 \text{ mm} / t = 1.85 \text{ mm}$.

Choosing to use these parts affects and limits several parameters.

Table 4-2 presents the key dimensions of the parts governing the design of the prototype. The degrees of freedom are decreased, reducing the number of dimensions to consider in the design process.

<u>Parameter</u>	<u>Symbol</u>	<u>Limitation / explanation</u>	<u>Value</u>
Magnet pitch	τ_m	Magnet height	40 mm
Magnet inner diameter	\varnothing_{mi}	Set parameter	10mm
Magnet outer diameter	\varnothing_{mo}	Set parameter	46.5 mm
Min. inner coil diameter	\varnothing_{ci}	Magnet outer diameter	47 mm
Max. outer coil diameter	\varnothing_{co}	SMC-ring inner diameter	62 mm
Back-iron inner diameter	\varnothing_{bi}	SMC-ring inner diameter	62 mm
Back-iron outer diameter	\varnothing_{bo}	SMC-ring outer diameter	70 mm
Max relative amplitude	$x_{rel,max}$	Max. allowed seal speed	15.9 mm

Table 4-2: Initially set parameters for prototype 2B

The composition of the cross section of the electromagnetically active part of the machine is decided due to the chosen components. It follows that an attempt to achieve the target performance values (Table 4-1) must focus on electromagnetic axial properties and gas spring topology.

4.4 Electromagnetic design

The only power input to the system is the electromechanical interaction between the tubular main coils and the permanent magnets. The total input power needed to approach the target output power as specified, can be achieved by means of increasing power density and extending the electromagnetically active length.

This sub-chapter includes presentations of the components involved in the electromechanical energy transfer of 2B, and methods for analysing electromagnetic loss phenomena. This provides the understanding needed for a single phase module analysis, concluded with a proposed optimal geometrical design.

4.4.1 Permanent magnets

Two types of rare-earth permanent magnets, with the dimensions mentioned, are available in the Resonator workshop: Neodymium-iron-boron (NdFeB) and samarium cobalt (SmCo) magnets, both delivered by Sura Magnets AB. Rare-earth magnets show high flux density, high coercivity and close to linear demagnetization curves (El Shahat et al., 2010). For this prototype the NdFeB magnets are chosen because they possess a greater remanent flux density ($B_r = 1.14$ T) and are cheaper than the SmCo magnets. The latter are more temperature stabile (< 350 °C), less fragile, slightly more coercive and show a higher resistance to oxidation. Hence, they are more suitable for tests in harsh environments (SuraMagnets, 2011).

4.4.2 Back-iron

Designing 2B without back-iron and iron pole pieces will result in a low permeability μ in most of the magnetic path, yielding high total reluctance R and low flux density B with a proportionally low electromagnetic force, F_{mmf} . According to Jacobsen's (2011a) evaluation of no 2, adding back-iron will increase the thrust force per coil by 40 %.

Back-iron subjected to magnetic fields experience several processes leading to core losses: electric energy converted to heat. The magnetic properties of different materials are essential when considering their application as part of the magnetic path in an electrical machine. Back-iron material should ideally possess the following properties:

- Narrow B-H curve (Figure 3-2).
- High magnetic permeability.
- High electrical resistance.
- Equal performance for magnetic flux in all directions.

As explained in chapters 3.2 through 3.7, iron losses in a given material are mainly affected by two external factors: Magnetic flux density and frequency of the variable magnetic field.

4.4.2.1 Electric steel laminations

Laminations of electric steel as back-iron would be a mechanically stabile alternative, but the spatial properties must be carefully analyzed to avoid unnecessary core losses. The layers of insulation (Figure 4-2 4-2) increase the resistivity. This results in a substantial decrease in eddy current losses, though effective only in one or two dimensions (Hanselman, 2006). A perfectly stacked lamination structure, taking into account the local variations in magnetic

flux direction, would probably provide the best possible back-iron solution. Naturally, this might be hard to obtain.

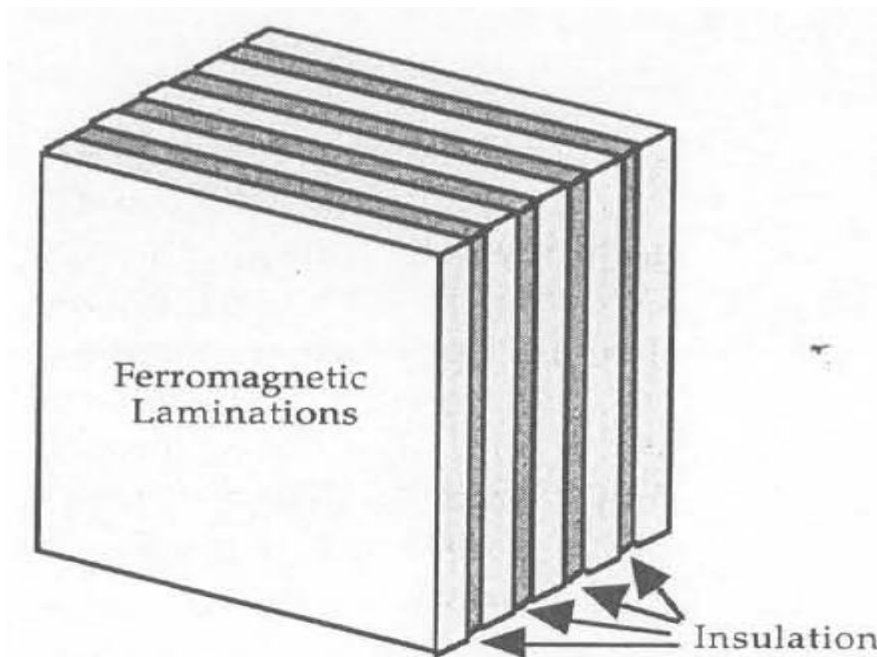


Figure 4-2: Structure of laminated ferromagnetic material (Hanselman, 2006).

4.4.2.2 Soft magnetic compound

The soft magnetic compound (SMC) materials consist of iron powder particles separated with an electrically insulating material (Figure 4-3).

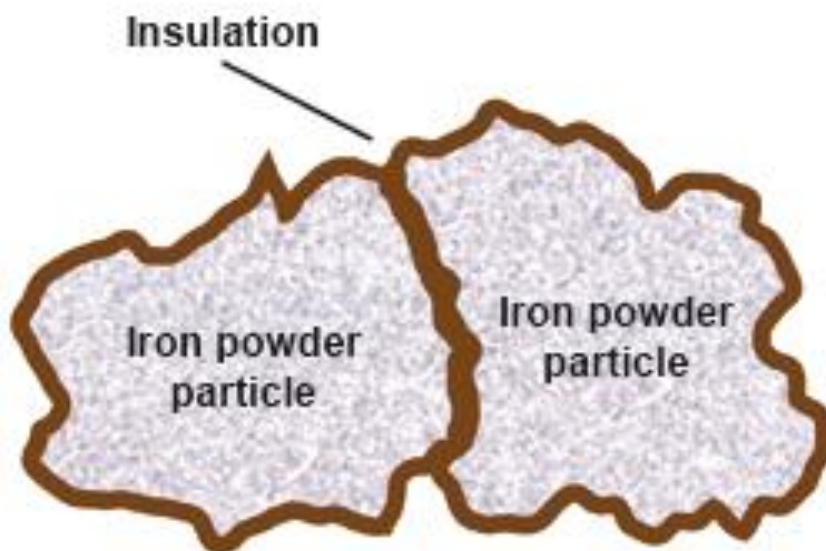


Figure 4-3: SMC material composition (Höganäs, 2011a)

The SMC material is brittle compared to steel, but due to a high pressure packaging method, the core losses should be significantly less. The result is a material of high permeance and high resistivity in all directions. (Höganäs, 2011a).

The material mix undergoes a two-step process:

- High pressure (up to 800 MPa) compaction provides mechanical strength and small dimensional tolerances.
- Heat- / steam treatment to evaporate lubricants contained in the components, and to obtain partial stress relief and gain additional strength. Details of the treatment are available in a confidential document from Höganäs AB (2009).

The last process is done in batches because of the size of the oven. Every batch is tested separately, and the results for the components used in the first version of 2B are listed in table 4-3. Compared to datasheets (available by contacting Höganäs AB), the density of the material in the delivered batch is relatively low, and the actual value of the resistivity is significantly lower than what is stated to be a typical value. Also, control measurements suggest bigger dimension tolerances than measured by Höganäs. According to Dahlström (2011), the components can be carefully grinded (< 0,3mm) after heat treatment without critically affecting the performance.

Magnetic DC properties	B@4000A/m [T]	1,12
	B@6000A/m [T]	1,23
	Hc [A/m]	245
	μ_{\max}	568
	Resistivity [$\mu\text{Ohm}\cdot\text{m}$]	70 ± 13
Magnetic AC properties	Frequency	Core losses 1T [W/kg]
	50Hz	6
	100Hz	13
	200Hz	28
	400Hz	63
	600Hz	105
	800Hz	152
	1000Hz	206
Physical properties	Density [g/cc]	$7,23 \pm 0,03$
	Outer diameter [mm]	70,13
	Inner diameter [mm]	62,00
	Height [mm]	$24,89 \pm 0,04$
	Weight [g]	$145,86 \pm 1,70$

Table 4-3: Somaloy 700 3P soft magnetic compound material properties, first batch (Höganäs, 2011b).

The core losses are measured by Höganäs, using the AC/DC testing equipment “Messtechnik Brockhaus Messtechnik MPG100 D” (Dahlström, 2011). Measured values deviate from the

data sheet values with < 35 % in the targeted frequency range for 2B. Increasing the magnetic flux density from 1.0 T to 1.5 T typically results in a 100 % increase in core losses. Table 4-3 and the mentioned datasheet give a fair description of the expected SMC power loss in the prototype.

The SMC rings are the back-iron components chosen for 2B, due to their, in theory, satisfying performance.

4.4.3 Magnet piston iron

The magnet separators and magnet piston end pieces move along with the permanent magnets. Using magnetic iron in these components a better magnetic flux path for the magnetic field originated in the magnets. Jacobsen (2011a) has estimated a thrust force increase of 12 % when using magnetic iron between the magnets, compared to a non-magnetic material.

The coil current creates a magnetic field, experienced as a varying field to the piston iron components. The core losses yielded are assumed negligible compared to back-iron losses and copper losses, and are therefore ignored in the upcoming power loss estimation.

4.4.4 Main copper coils

Copper losses lead to decreased efficiency and heating of the machine. Alternatives for wire types are discussed here, with respect to different kinds of loss mechanisms and availability. Advantages and disadvantages are briefly summarized in table 4-4 at the end of this sub-chapter.

Generally stated, DC resistance is a product of copper fill factor. A high fill factor is achieved by tight stacking and limited use of internal insulator material. The AC resistance is a product of eddy currents resulting from an external magnetic field, and from those explained by skin effect and proximity effect as results of alternating current in the wires. Consequently, the logic of comparing wire types concerns spatial and geometrical considerations.

4.4.4.1 Copper foil

Berge (2005) chose to use copper foil in his Resonator design project. It has a large surface area and shallow conductor depth, reducing proximity effect and skin effect. The only practical solution for using copper foil is winding every turn tangentially in full axial height, like a roll of paper. The radial direction of the alternating magnetic field from the permanent

magnets is unfortunate, since eddy currents will occur in the plane normal to the direction of the magnetic field.

4.4.4.2 Single circular wire

The most commonly available wire type is the circular kind. An alternative for 2B is using the thickest possible circular wire to fit the available air gap volume with the calculated number of turns. Stacking the wire is not very efficient, yielding a poor fill factor. A relatively thick wire would cause unfortunate eddy currents. Nonetheless, the immediate availability of assorted wire diameters makes circular wire an alternative for testing different coil pitches, air gaps and coil turns.

4.4.4.3 Litz wire

To minimize eddy current losses at high frequencies in conductors, an alternative is to use multiple, separately isolated and twisted, conductor strands, so called Litz wire. A lot of these wire types are intended for frequencies in the kHz and MHz range, so the diameter of each conductor strand is not necessarily much bigger than the insulation surrounding it. Hence, the copper fill factor becomes small (pack-feindraehte.de, 2011). A better alternative would be bundles of rectangular strands, where the cross section dimensions where in the proximity of 0.5 - 1.0 mm, and the bundle dimensions would fit the air gap dimensions. This is not readily available, and would require a special order and longer delivery time.

Wire types	DC resistance	AC resistance	Availability
Copper foil	+	-	-
Single circular wire	-	-	+
Litz wire	--	+	--
Rektangular wire	++	-	++

Table 4-4: Summary of discussion regarding choice of wire type for 2B

4.4.4.4 Single rectangular wire

A rectangular wire of matching size would result in a fill factor superior to all other alternatives. A possible disadvantage is copper losses, because of the relatively big cross section dimensions.

As mentioned, rectangular copper wire of dimensions $t = 1.85 \text{ mm} / h = 2.35 \text{ mm}$ is available. These dimensions proved useful for stacking the wire as shown in figure 4-4, although the winding process resulted in a slightly bigger gap between the wire strands.

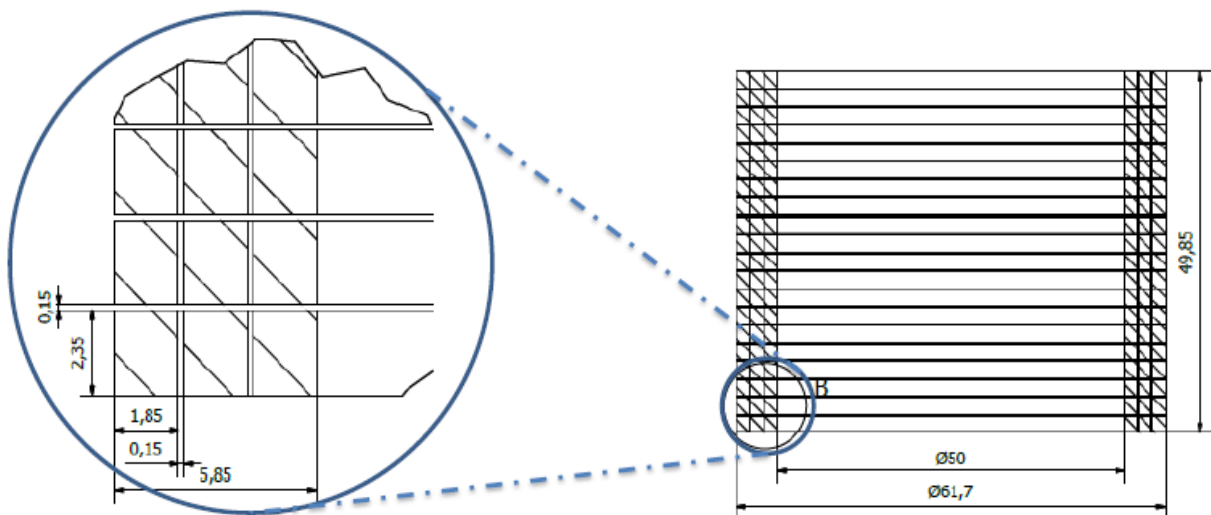


Figure 4-4: Details of 2B main coil structure (Li, 2011b).

The readily available rectangular wire is chosen for this version of the 2B prototype, because of high fill factor, low resistance and easy availability.

4.4.5 Sensor coils

Two identical sensor coils, as described in chapter 3.10.2.1 are embedded in the stator, one on each side. According to Faraday's law, the number of turns scales the amplitude of the induced voltage. Hence, a thin copper wire should be used to induce the best possible signal. On the other hand, thin copper wire is quite fragile, which is disadvantageous considering the high mechanical strains planned for this prototype. The compromise for the first version of the 2B stator is a circular wire ($\varnothing = 0,4$ mm) with 130 turns.

The movement sensor application is known from prototype no 2. In addition, these sensors will be tested as position sensors, using the Hall sensor principle. The piston is considered an iron core. Applying an AC current in the kHz range to the main coils, yields alternating magnetic flux in the iron core. The piston will not move significantly for high frequencies that do not match the resonance frequency of the system. Also, low currents will not produce a sufficient magnetic force to move the piston. The distribution of the magnetic flux depends on the piston position, because of the high permeability of iron compared to both air and the permanent magnets. A voltage is induced in the sensor coils. The voltage amplitude difference in the two identical sensor coils indicates piston displacement (Ramsden, 2006).

Another Hall sensor type is possibly achieved by splitting one sensor coil into three parts. The total height must axially correspond to the end iron component of the piston. An AC current can be applied to the mid section, making position detectable through the induced voltage signal in the two equal sections on each side.

4.4.6 Single phase module analysis

Since the magnet size and total coil area are fixed parameters, it is useful to define a single phase module. It consists of two adjacent magnet poles of equal polarity, a magnet separator dividing them, and one coil with surrounding back-iron (Figure 4-5). The module should be optimized for high power density and low losses.

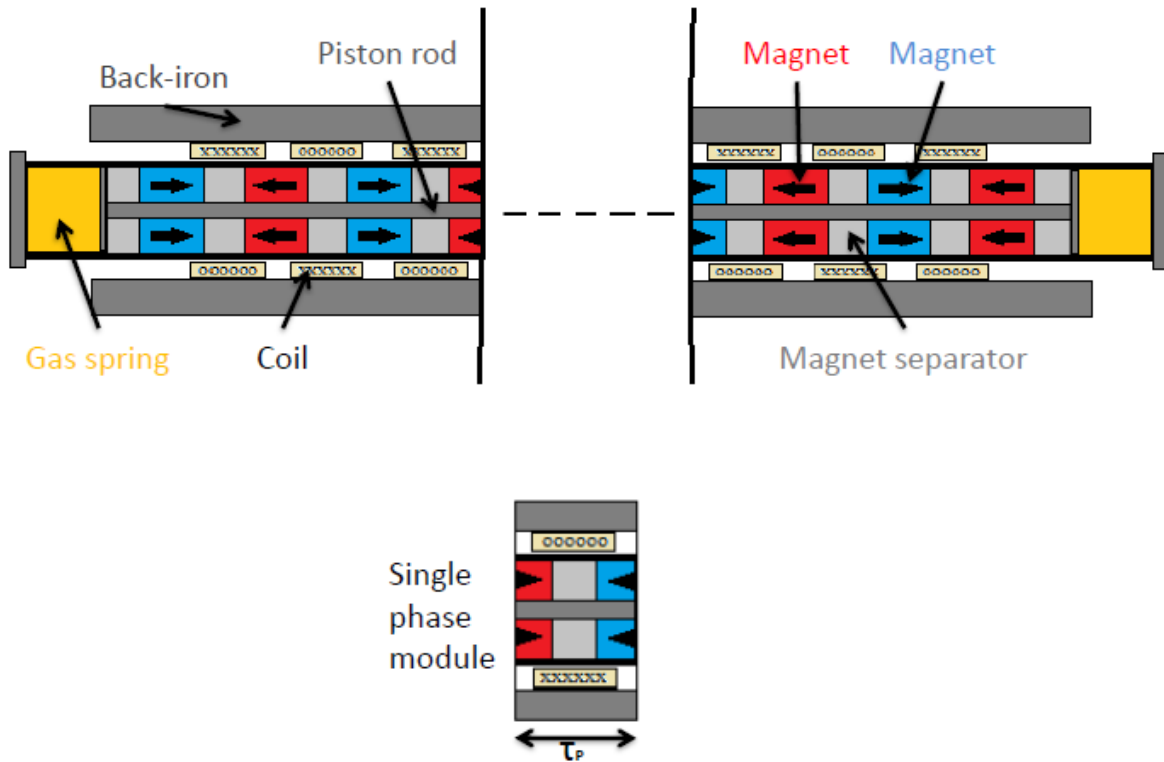


Figure 4-5: Over: Multiple modules combined. Under: Single-phase module (Jacobsen, 2011c).

4.4.6.1 Current density

A section of the copper coils normal to the tubular wires makes the air gap cross section area A_G , containing one copper coil, visible (Figure 4-6). This area does not include the space between adjacent coils, but it does include the area occupied by the plastic tube. The total flow of current in the n_t turns of one coil perpendicular to this plane, $n_t \vec{l}$, can be described as the current density in the copper coils:

$$\vec{j}_G = n_t \vec{l} / A_G \quad (4-7: \text{Current density})$$

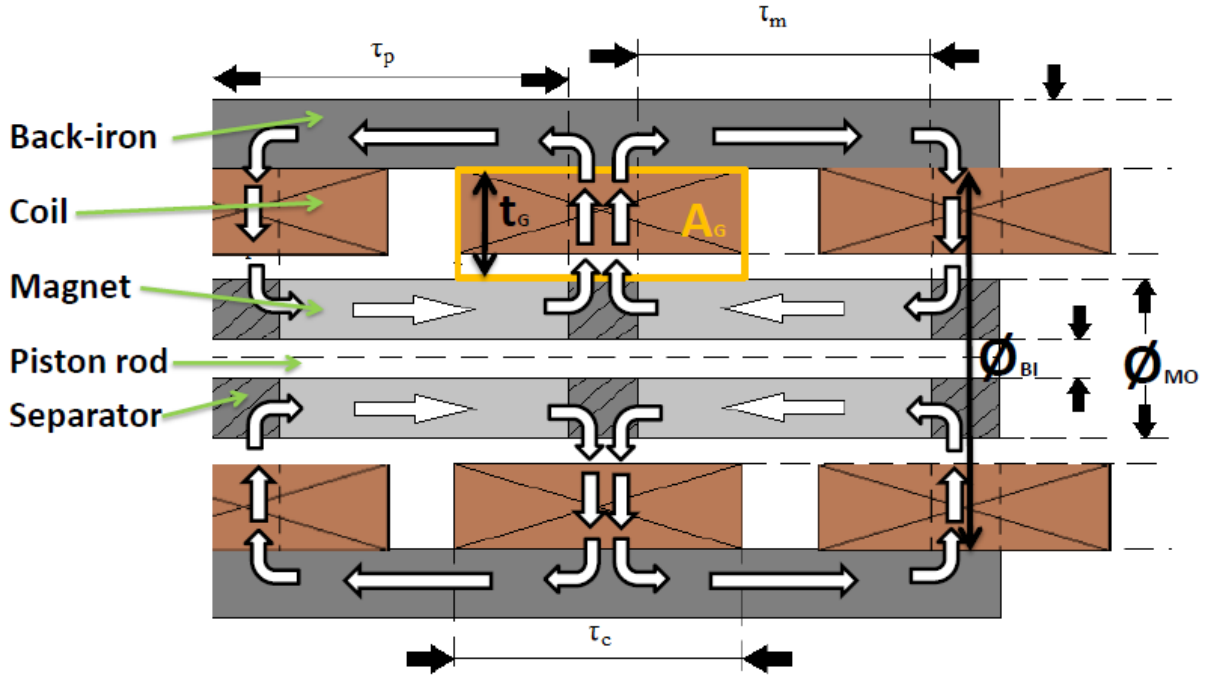


Figure 4-6: Machine geometry showing geometric design parameters used in the single module analysis (Jacobsen, 2011b). The main magnetic field direction is marked as white arrows, more detailed in figure 4-7.

4.4.6.2 Lorentz' force per module

An average radial magnetic flux density in the coil volume, \bar{B}_{rad} , is assumed. The wire length l involved in force production equals the average circumference \bar{O}_C of the coil. The Lorentz' force per electric machine module, $F_{L,M}$, can be expressed:

$$\begin{aligned} \vec{F}_{L,M} &= \bar{B}_{rad} \times \vec{I} \cdot l = \bar{B}_{rad} \times \vec{J}_G \cdot A_G \bar{O}_C \\ &= \bar{B}_{rad} \times \vec{J}_G \cdot t_G \tau_C \bar{O}_C \end{aligned} \quad (4-8: \text{Lorentz' force per machine module})$$

This expression allows describing how to obtain a maximum force output:

- The wire length l involved in producing magnetic force equals the average circumference \bar{O}_C .
- \vec{J}_G , t_G and τ_C are assumed constant for a given nominal current in a given wire type.
- The magnetic flux density \vec{B} increases when τ_f decreases. However, the saturated state should be avoided. Also, a small τ_f creates big variance in the distribution of the \vec{B} -field, while a bigger τ_f yields a smoother distribution. This affects the time-dependent force distribution and the mechanical movement of the machine.

Generally it can be stated that decreasing the magnet separator length increases the force per machine length, to the point where saturation of the magnet separator iron diminishes the effect.

4.4.6.3 Pole pitch optimum

The mentioned physical relations are compiled in a script by Jacobsen (2011b), and used for a finite-element-method analysis. One result of this analysis is an optimal relation between the magnet pitch τ_m and the pole pitch τ_p , which sets a value to the magnet separator pitch τ_f , and hence the pole pitch:

$$\left| \frac{\tau_m}{\tau_p} \right|_{opt} \approx 0.73$$

$$\tau_f = \tau_p - \tau_m = \frac{40 \text{ mm}}{0.73} - 40 \text{ mm} = 15 \text{ mm} \quad (4-9: \text{Magnet separator pitch})$$

$$\tau_p = \tau_f + \tau_m = 55 \text{ mm} \quad (4-10: \text{Pole pitch})$$

The coil should cover the surface area of the magnet separator at all times. The target amplitude is $x_{max} = 15.9 \text{ mm}$, so the coil pitch should be at least $\tau_p = 2 \cdot 15.9 \text{ mm} + 15 \text{ mm} = 46.8 \text{ mm}$. On the other hand, the coil should be as small as possible to avoid unnecessary copper losses. For a prototype, higher amplitudes could be relevant for testing, so a coil pitch close to 47 mm should be applicable.

4.4.6.4 Machine length limitation decides number of modules

A slight radial misalignment of the magnet piston will cause radial forces because of axial leakage flux through the copper coils (figure 4-8). This can cause strain on the magnet piston bearings, and also the gas spring seals (Jacobsen, 2011b). The magnet piston length should therefore be moderately chosen. 9 copper coils and 10 magnets, yielding a magnet piston length $< 600 \text{ mm}$, are chosen for the 2B design.

4.4.6.5 Magnetic flux density distribution

The magnetic flux density in the coil is found through an analysis using Comsol software. A representation of the magnetic flux density distribution is given in figure 4-7 (Jacobsen, 2011b).

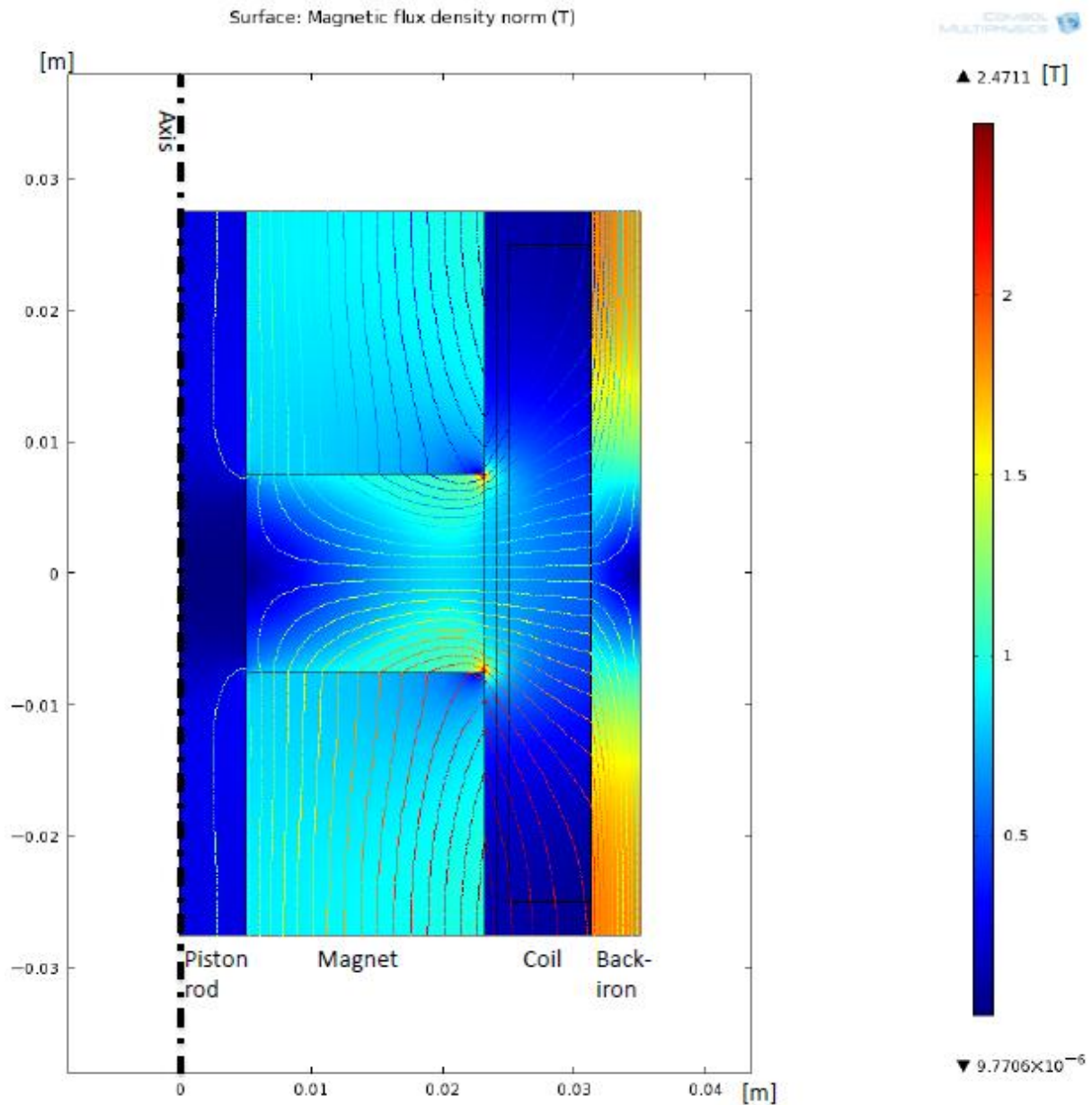


Figure 4-7: Magnetic flux density distribution of one machine module (Jacobsen, 2011b). Colors (dark blue through dark red) act as visual indication of flux density.

4.4.6.6 Air gap flux density

The radial and axial components of the magnetic flux in the coil volume are given in figure 4-8. The average radial magnetic flux density in the entire coil volume is calculated to $\overline{B}_{rad} = 0.3 \text{ T}$.

The axial leakage flux density $B_x = B_z$ is also shown, and it is implied in the contour-lines of figure 4-7. \vec{B}_x contributes to a radial force component. In the neutral position, however, the netto force component is zero, since the positive B_x balances the negative B_x .

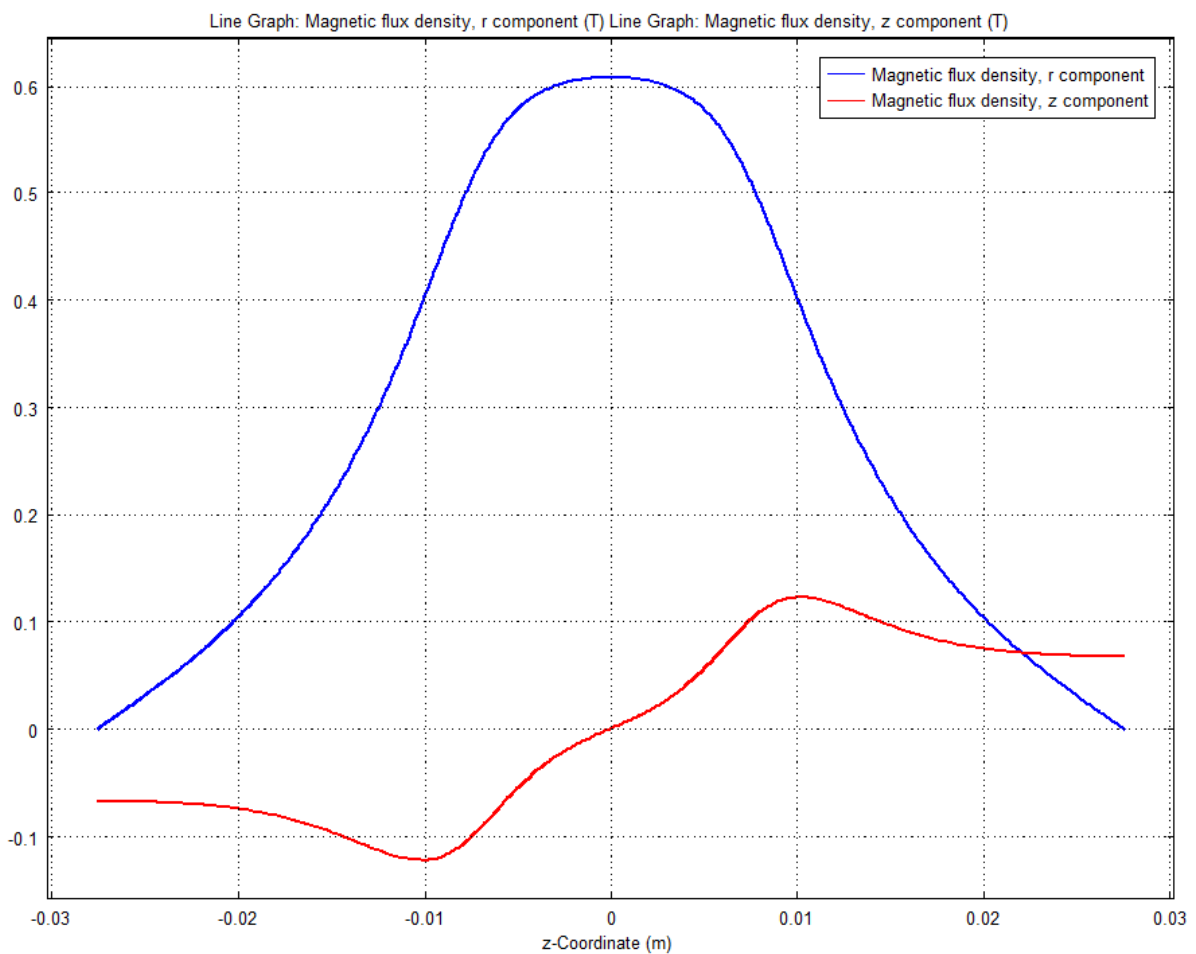


Figure 4-8: Magnetic flux density in the coil corresponding axially to a magnet separator. Blue: Radial component. Red: Axial component. z in the figure equal the axial x-direction (Jacobsen, 2011b).

4.4.6.7 Back-iron flux density

An estimation of the back-iron flux density \vec{B}_I corresponding axially to a magnet separator is presented in figure 4-9. An average value of $\overline{B}_I = 1.3$ T can be stated. This can also be seen in figure 4-7.

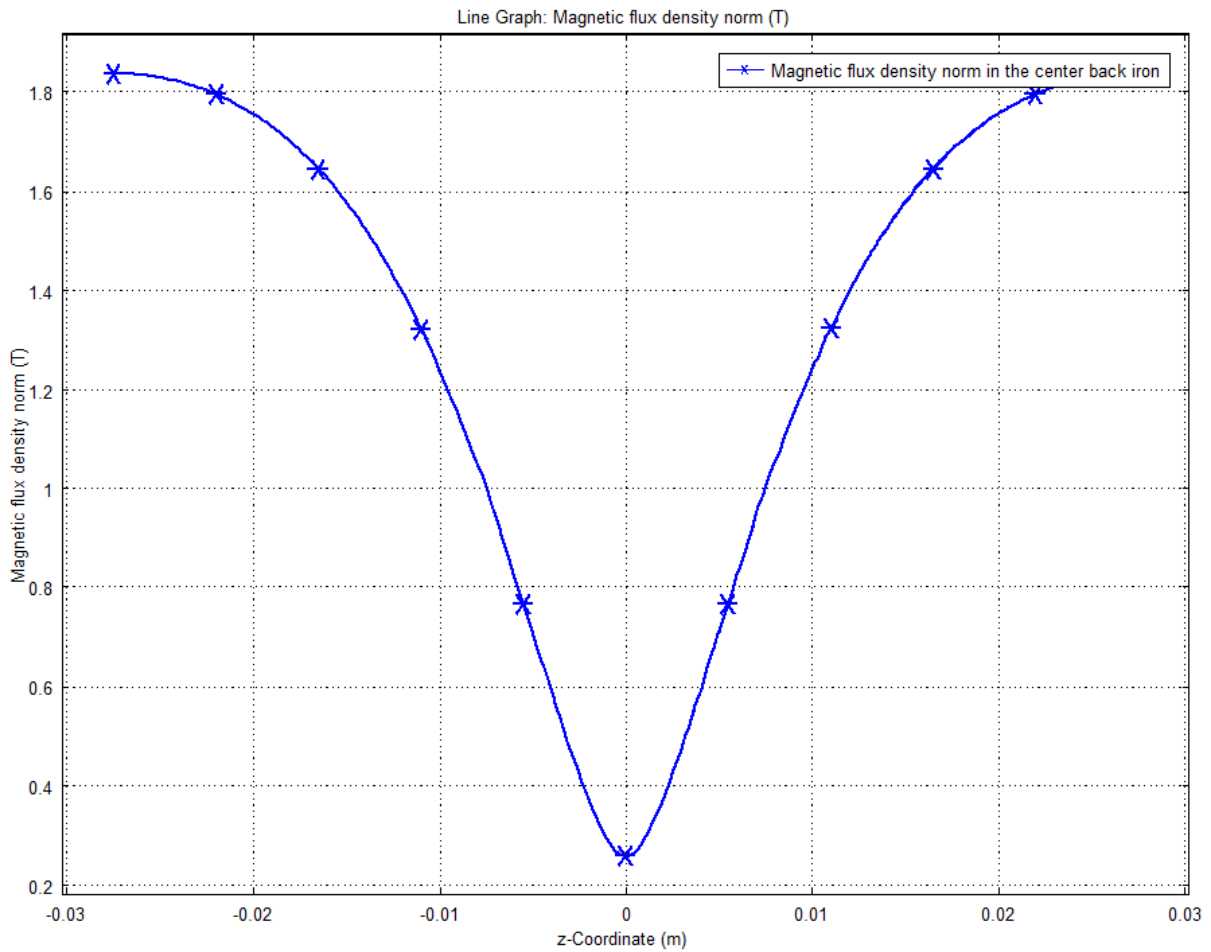


Figure 4-9: Magnetic flux density in the center of the back-iron material, corresponding to a magnet separator (Jacobsen, 2011b).

4.5 Gas springs

The gas springs on each end of magnet piston cause the system to resonate and temporarily store energy in the potential difference of the gas pressure in gas chambers and the kinetic energy of the moving masses. They are essential to the Resonator concept. Up to this date, they have not been successfully realized in any of the existing prototypes.

Realizing gas springs with torus-shaped dynamic seals is attempted in the 2B design.

4.5.1 Initial low pressure test

Low pressure tests performed on no 2 shows a correlation between gas pressure variations and resonating frequency (Table4-5).

Initial pressure [MPa]	Pressure after test [MPa]	Resonance frequency [Hz]	Power input [W]
0.1	0.1	26	15
0.3	0.3	32	15
0.4	0.36	34	15
0.5	0.42	34	15
0.7	0.53	34	16
0.8	0.58	32	16

Table 4-5 Pressure / resonance frequency test on the no 2 prototype (Bostad and Li, 2010).

The test object had no dynamic seals acting against the PEEK tube on the gas piston, except for the hard plastic plate on the magnet piston ends. These are not ideal for sealing purposes, but the resonance frequency does increase when increasing the chamber pressure up to 0.4 MPa. Increasing up to 0.7 MPa, the piston seems to leak. The pressure decrease at 0.7 - 0.8 MPa suggests an increased friction due to the higher density of air molecules. Also; the valves show noticeable leakage by initial pressure > 0.4 MPa (Bostad and Li, 2010).

4.5.2 Gas spring design for 2B

Since the gas springs are not thermally isolated, the compression/expansion process in the 2B gas spring chambers is completely not adiabatic. There will be some heat transport Q from the gas spring chamber to the exterior. This further complicates the analysis of the gas spring force. For a good example of such analysis, considering the heat transfer process, the reader is referred to Lu and Chang (2008).

In order to achieve high frequencies, a strong gas spring force is required. This is directly related to the pressure inside the gas spring chambers, suggesting high mechanical strength requirements.

4.5.2.1 Resonance frequency

The natural resonance frequency for a free piston gas spring system (Xiao et al., 2010) presented in the theory chapter reveals certain relations:

$$f_0 \propto \sqrt{p_0 \cdot A_{GSP} / x_{max} \cdot m} \quad (\text{Equation 4-11: Resonance frequency relations})$$

This can be used as a rule of thumb, where:

- The gas spring piston area A_{GSP} can be increased by means of separate gas spring chambers and multiple gas springs acting in the same direction.
- An increase of the initial pressure p_0 requires a stronger chamber.
- The practically obtainable amplitude x_{max} is limited by the length of the magnets and iron spacers.
- Moving mass m is mainly a result of the masses of stator and piston, in addition to the external suspension. An analysis of the moving mass follows in a separate chapter.

4.5.2.2 Chamber requirements

Depending on the length of the gas spring and the stroke length of the piston, a high maximum gas pressure inside the gas spring chamber is expected. The main challenges identified are:

1. Sufficiently strong chamber walls to withstand the maximum pressure force.
2. Ability to transfer heat, from gas chambers near the electromagnetically active machine part and to the exterior. This can be discussed, since heat transfer equals energy loss. However, the main concern is not exceeding the temperature tolerance range of the seals.
3. Smooth surface acting against the dynamic seals.
4. Temperature stable structure up to minimum 180 °C.

4.5.2.3 Topology - separate gas spring steel chambers

A plastic or PEEK tube can not easily fulfill these requirements. The wall thickness of the tube demanded for containing high pressures would exceed the acceptable amount of lost copper coil volume. The best way to provide sufficient solutions to these challenges were assumed to be using steel instead of plastic and separating the chambers. Answering to the four points for chamber requirements:

1. The pressure tolerance of steel exceeds that of PEEK.

2. The thermal conductivity of PEEK materials ranges from 0.25 to 1 W/mK (VINK, 2010), while typical values for stainless steel are between 12 and 45 W/mK. Also; separating the chambers will relocate the heat production of the gas springs away from the electric machine.
3. The machinability of steel is superior to the PEEK material.
4. The thermal stability of steel is superior to the PEEK material.

The separate gas spring steel chamber solution presents other advantages and challenges. See assembly figure 4-17 to easier follow the arguments:

- The total gas spring area increases for two reasons:
 - The diameter can be increased from 47 mm to 63 mm without increasing the total diameter of the machine.
 - Two additional gas springs are introduced, with a slightly smaller area due to the 25 mm diameter rod in center of the spring.

This increases the total gas spring area with a factor of 3.3 (Appendix B.1). Since $f \propto \sqrt{A_{GSP}}$ (Xiao et al., 2010) this will lead to an increase in resonance frequency of approx. 80 %.

- The magnet piston chamber will not be pressurized. In case of leakage, a channel for pressure release can be designed. This gives two advantages:
 - The possibility of increased friction on the magnet piston due to higher density of gas molecules is eliminated.
 - The risk of explosion due to pressurized gas decreases significantly. The steel chamber can be built as a normal hydraulic cylinder with a security factor, leaving the risk of material fracture by unexpected overpressure negligible.
- The stability of the rod increases. With one gas spring in each end of the machine, the rod must always withstand the pressure force from both springs through its consistent length. With two springs on each side, the piston closer to center (piston 2) experiences force on an area A_2 , relative to the outer piston (1) area A_1 by the factor 0.84 (Appendix B.2). Piston 1, on one side, acts parallel with piston 2 on the other side. Hence, assuming no leakages and equal initial pressure and gas spring nonlinearity on both springs, it can be assumed that $0.84 / 1.84 = 46\%$ of the gas spring force is acting as a tensile force component, resulting in significantly less total strain on the piston rod. Local variations on the piston rod must still be accounted for.
- The increased number of gas springs increases the number of valves and associated equipment, increasing the possibility of failure. It also increases the number of dynamic seals. The functionality of these seals is hard to predict.
- Given the same electromagnetically active length, the separate gas spring chamber design demands a longer machine. This causes a lower power density pr length unit,

since the gas springs do not constitute an additional energy input to the system. It does not, however, decrease the energy storage density, since the gas springs become more voluminous and the piston area bigger.

- The weight increases, roughly by the weight of the gas spring chambers. Since

$f \propto \sqrt{1/m}$ this results in a frequency decrease.

Conclusively; changing the design to separate gas spring chambers leads to more advantages than disadvantages. The possible doubling of resonance frequency and the increased mechanical robustness outweighs the increase of topological complexity and machine size.

4.6 Assembly of 2B

The assembly of 2B is done in steps. Assembly of piston, stator, gas spring and chassis require different considerations, separately presented in this sub-chapter. Alternatives are presented for possible incorporation in later work.

4.6.1 Piston assembly

Forces acting between permanent magnets with equal poles facing each other increase with decreasing distance. Jacobsen (2011d) has calculated the axial repelling forces between to magnets of the size used in the 2B piston, presented in figure 4-10.

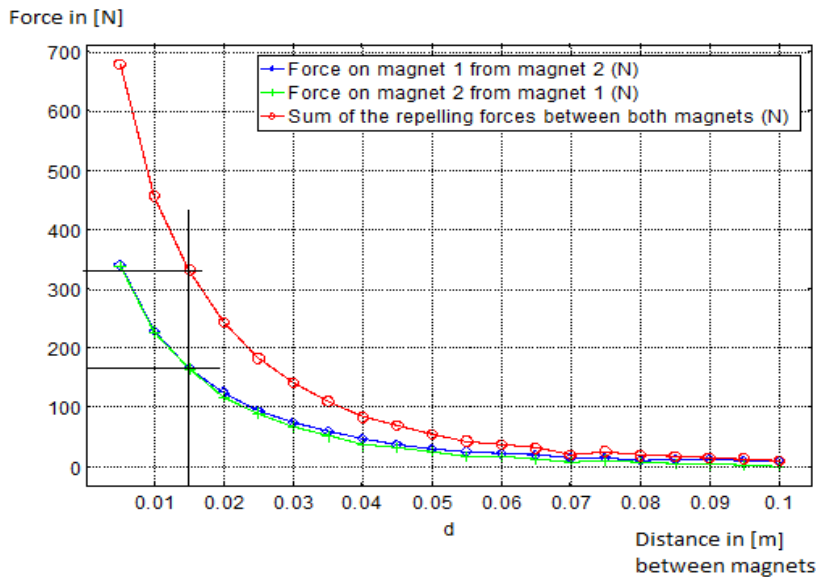


Figure 4-10: Repelling forces between two permanent magnets as a function of distance between the magnet surfaces of equal polarity. Calculated for the magnet types used in the 2B piston (Jacobsen, 2011d).

The repelling force between two magnets is $F_{RM} \approx 340$ N. However, between the repelling magnets are the magnet separators, made of magnetic iron. Connecting the magnet separator to one of the magnets must be done carefully because of the attraction force between the permanent magnet and iron. In contact with the north pole of one permanent magnet, the magnet separator is magnetized to a nearly linear flux, and hence attracted by the permanent magnet, as in figure 4-11 B.

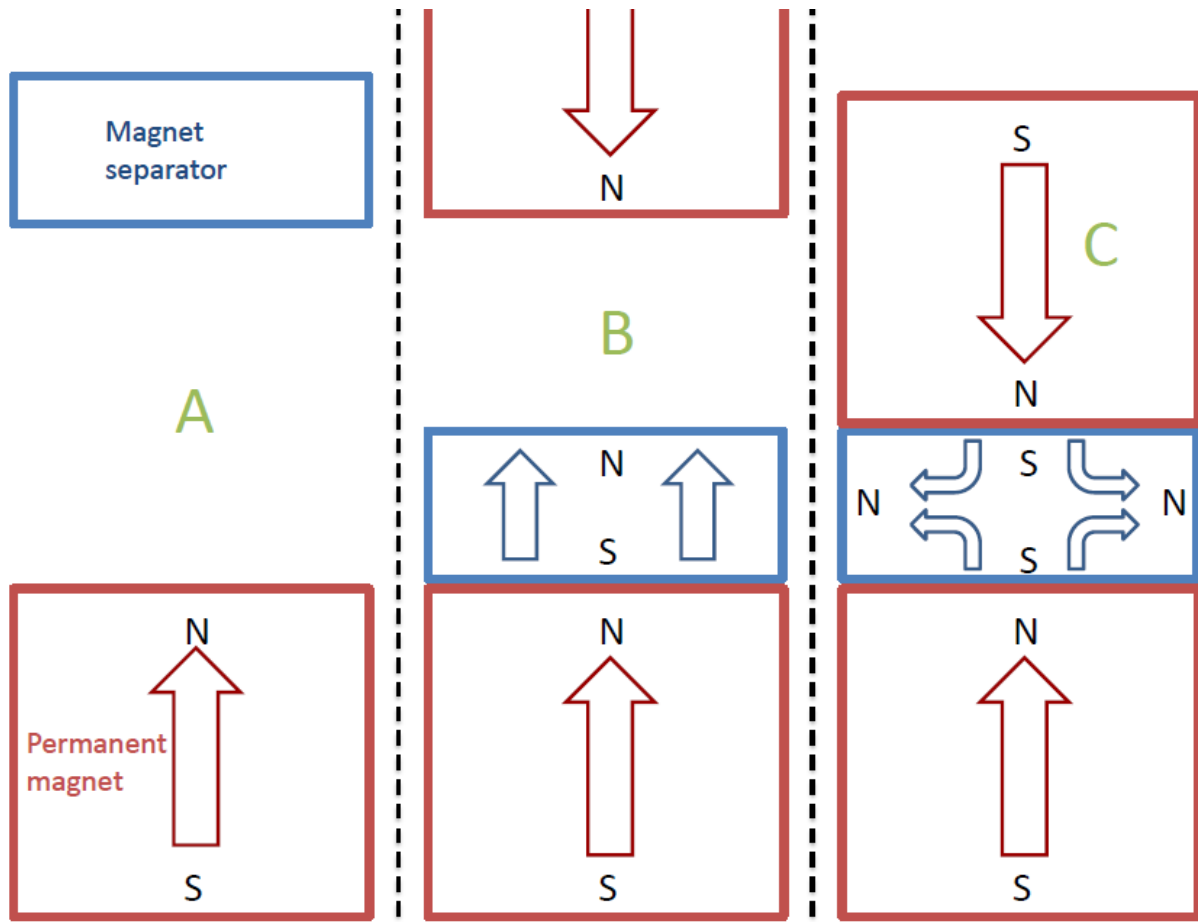


Figure 4-11: Magnetizing an iron piece. Polarity N/S marked. Arrows symbolize magnetic field directions.

A: Permanent magnet has not magnetized the magnet separator.

B: Magnet separator is magnetized by one permanent magnet.

C: Magnet separator is magnetized by two permanent magnets.

By moving the next permanent magnet closer, the separating iron piece also becomes magnetized by another north pole. It ends up being magnetized to polarity south on the surfaces in contact with the permanent magnet's north poles, and polarity north on the surfaces against air, as in figure 4-11 C. Hence, an attraction force F_{AM} acts between the iron separator and each of the permanent magnets. Initial testing shows that for this particular case, F_{AM} exceeds the repelling force F_{RM} .

For radial stabilization, all the piston elements should be connected using araldite 2014 (Huntsman, 2007).

The assembly rod must have low dimension tolerances to ensure a straight piston. A hydraulic tube of non-magnetic steel is bought for this purpose. 10 magnets with 9 spacers and 2 end iron pieces are connected in the axial direction (Figure 4-12).

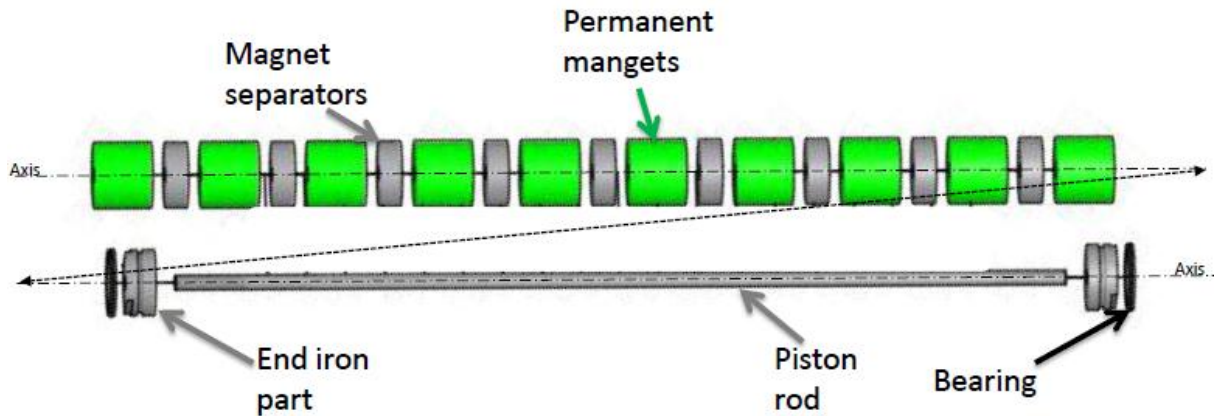


Figure 4-12: Rotor assembly, exploded view. Axial centerline prolonged for simpler graphical presentation. All parts are mounted on the piston rod (Li, 2011b).

The end iron pieces serve several purposes:

- Close the magnetic path for the end magnets.
- Tighten the magnetic piston assembly with a threaded connection to the magnet piston rod.
- Connect the magnet piston to the gas spring piston, also with a threaded connection.
- Support bearings for a controlled contact between the magnet piston and the stator inner surface.

4.6.2 Stator assembly

Different alternatives for controlling the critical surface between piston and stator can be discussed. Electromagnetically speaking, the distance from the permanent magnets to the coils should be as small as possible to maximize the coil volume. On the other hand, the radial displacement of the piston is difficult to predict. Mechanical contact could, in the worst case, yield electrical contact between magnets and copper wire.

4.6.2.1 Carbon fiber layer

An alternative for reinforcing the piston outer surface and / or the coil inner surface is by adding a layer of carbon fiber. An example is presented by Wang et al. (2007), where a 0.4 mm layer of carbon fiber was added to a permanent magnet piston. A similar solution has been tested, as research in the design process. A steel bolt, similar in size and surface structure to the actual piston, was covered with carbon fiber axial sleeve material. The fiber was wrapped around the steel bolt, saturated in SP Ampreg 21 epoxy, and vacuum-packed at Morild Marin AS. The fiber added approx 0.5 mm to the radius of the bolt.

This concept could show useful, if the fiber surface was plastered and smoothed. Also, a similar layer could be added to the inside of the copper coils. Further investigation of these options is left for later prototypes, because another solution, discussed in the next chapter, seemed easier to obtain.

4.6.2.2 Plastic tube stator support

The workshop at UMB was able to machine a plastic tube with dimensions as in Figure 4-13. The tube is honed on the inside, trying to create a smooth surface for the piston to act against. The result of the honing is questionable. The material is a polyamide plastic, PA66, which can withstand 160 °C without deforming. This sets the maximum temperature of the electric part of the machine to $T_{max} = 150$ °C.

An alternative support tube can be delivered by VINK AS. The tube is made from PEEK-1000 material, with an outer diameter $\varnothing = 49.0$ mm. The PEEK material should outperform PA66 in terms of temperature stability, tensile strength and smoothness of the inner surface. Long delivery time and high cost postponed an order until initial tests are done. A PEEK tube does possibly constitute the best available tube solution for stator support, and it is an alternative in case the PA66 tube proves deficient for the task.

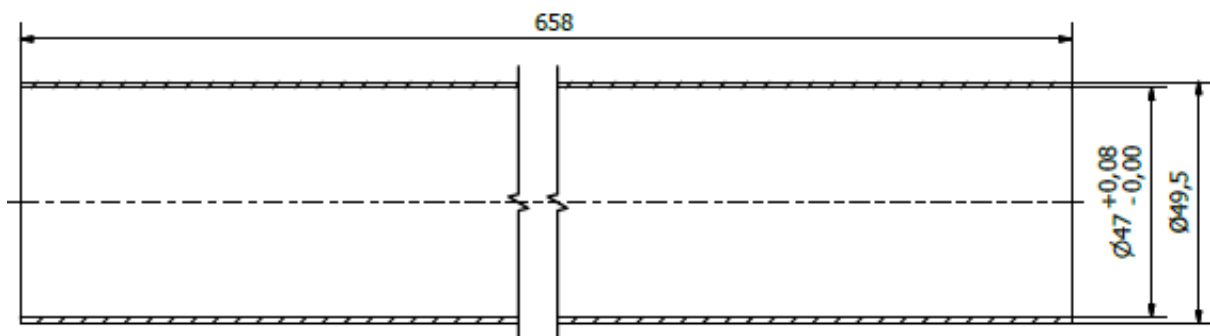


Figure 4-13: Tube of polyamid (nylon) PA66 material for stator support (Li, 2011b).

The thin walls of the plastic tube leave enough room for the main coils to be wound in three layers (Figure 4-14). This way, the wire enters the coil on one side and leaves on the other side, making a series connection of the coils possible.

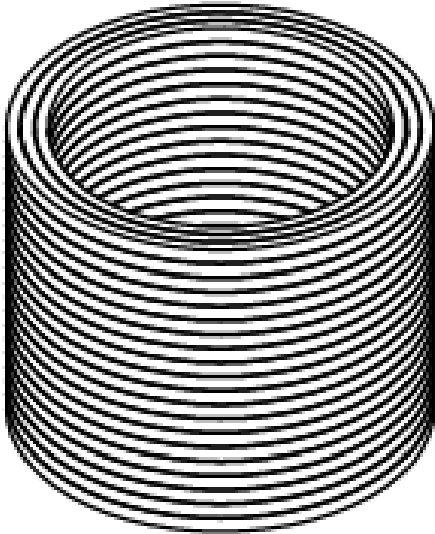


Figure 4-14: Three-layer winding of main coil, makes series connection possible.

The stator was assembled at Norsk Elektromotor AS (NE). A jig was made, to tightly wind the main coils so they could fit in between the plastic tube and the back-iron rings. An average of $\tau_c = 47$ mm axial height and $n_t = 54$ turns per coil was achieved. Including the plastic support tube, a copper fill factor of 0,68 is calculated in appendix B.6.

To avoid gas pockets and room for internal movement within the stator, loctite 3421 (Loctite, 2003) is used to fill all vacant volumes between the back-iron and the plastic support tube.

Temperature sensors were added on both sides, in between the last main coil and the sensor coil. The plastic end parts are also made of PA66. A groove in the longitudinal direction leaves room for leading through main wires and sensor wires.

During the work of assembling the stator, tests showed electric contact between the coils and the surrounding back-iron rings. A layer of insulating paper needed to be added in between, which required grinding of 0.3 mm of the inside radius of the SMC-rings. This alters the SMC inner diameter to $\varnothing_{bi} = 62.6$ mm.

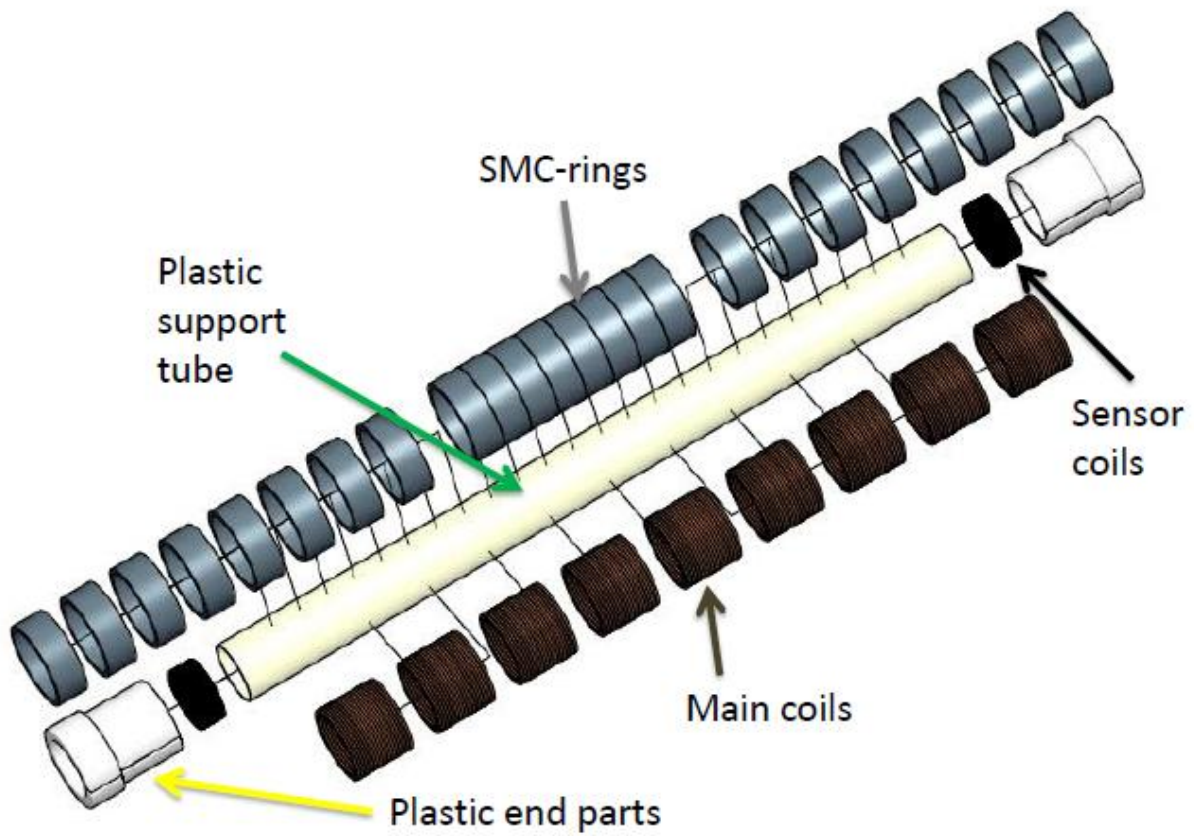


Figure 4-15: All stator parts (Li, 2011b).

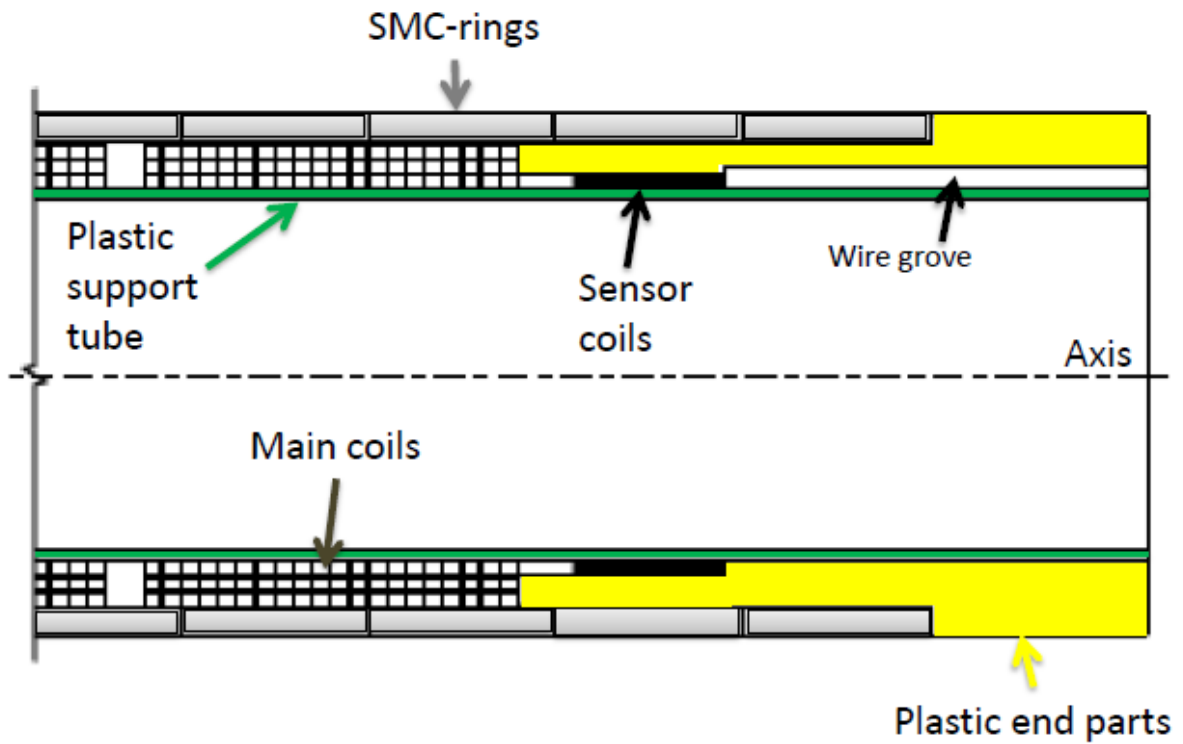


Figure 4-16: Assembly of one stator end, showing the arrangement of the different parts. Both stator ends are equal.

4.6.3 Gas spring assembly

The gas spring assembly is shown in Figure 4-17. The gaskets and seal rings are delivered by Trelleborg (Trelleborg, 2010).

The steel chamber wall thickness is sufficient to contain high pressures. The seals require a low roughness to act against. The seals have a low tolerance for particles bigger than the surface roughness, so assembling the gas springs must be done in a controlled environment.

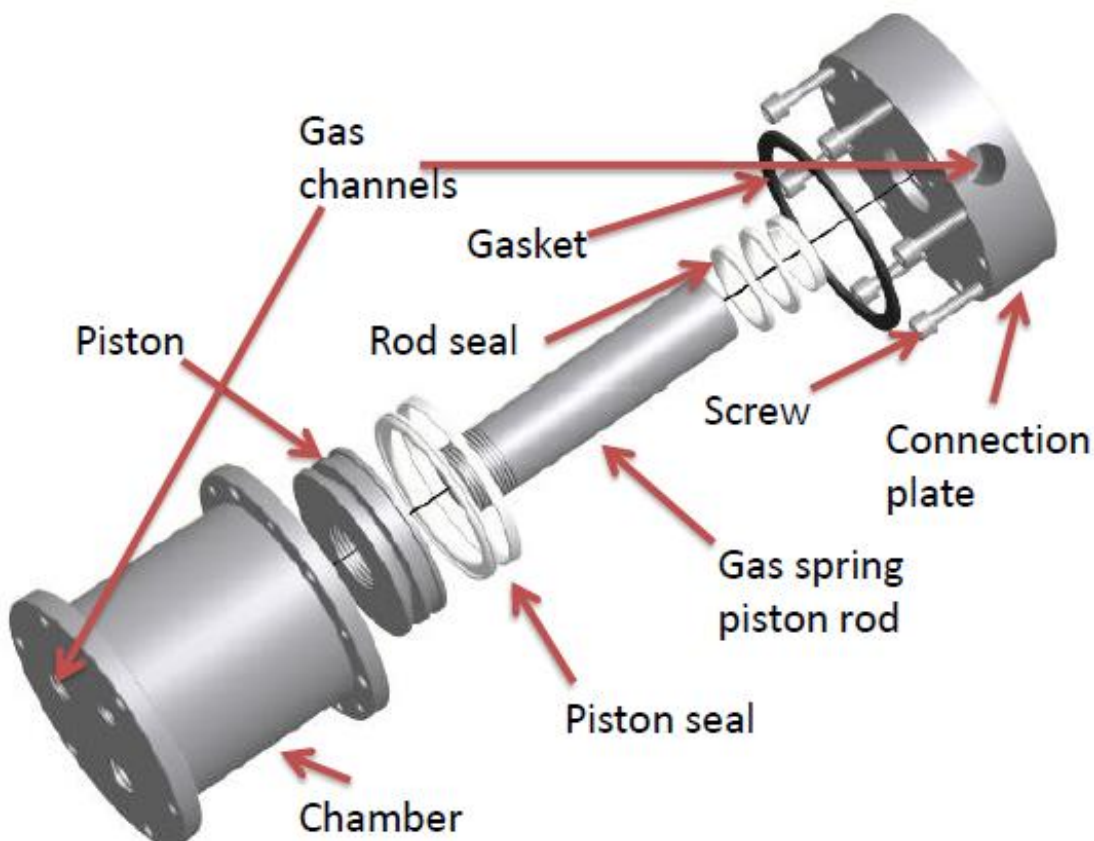


Figure 4-17: Gas spring assembly, exploded view (Li, 2011b).

To change the gas spring chamber length, only two components need to be changed: The steel chamber and the gas spring piston rod. Initially, there will be built two different versions, where the chamber length per gas spring will be 24 mm or 36 mm. Simulation results used later in this thesis are mainly based on a chamber length $x_{GSC} = 24$ mm.

4.6.4 System assembly

Comparing to the reference hammers; the outer diameter of the back-iron approaches the Wassara 80 hammer when including an outer steel casing. The prototype will not be used for

actual down-hole drilling, so the outer diameter is pertinent only as a reference point. The casing solutions chosen include flanges exceeding the reference diameter. The flange solution is chosen because of easy access and assembly. This does not exclude the relevance of the comparison. Other solutions can be found for future products designed for industrial mass production.

Appendix D.4 provides an axial cross-section view of an assembled 2B prototype. The flanges connect the gas springs to the stator, and the magnet piston rod is attached directly to the gas spring piston rod (Figure 4-18) with matching threads.

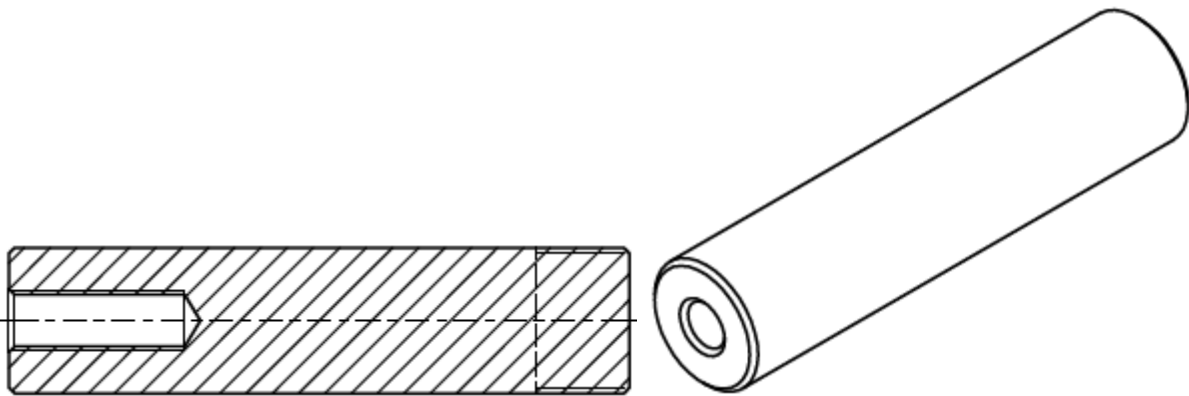


Figure 4-18: Gas spring piston rod (Li, 2011b).

Left: Cross-section. Threads for connecting to the magnet piston rod ($\varnothing_{mi} = 10$ mm) are seen on the left side
Right: Isometric 3D representation.

4.7 New and adjusted machine parameters

In the course of the design process, several parameters have been decided. By collecting the decisions regarding parameters in this chapter, Table 4-2 can now be updated to Table 4-6.

Parameter	Symbol	Value	Limitation / explanation
Magnet pitch	τ_m	40 mm	Magnet height
Pole pitch	τ_p	55 mm	Single phase module optimization
Magnet separator height	τ_f	15 mm	Single phase module optimization
Coil pitch	τ_c	47 mm	Optimal available solution
Magnet inner diameter	\varnothing_{mi}	10 mm	Set dimension
Magnet outer diameter	\varnothing_{mo}	46.5 mm	Set dimension
Min. inner coil diameter	\varnothing_{ci}	49.5 mm	Plastic tube outer diameter
Max. outer coil diameter	\varnothing_{co}	62.6 mm	New SMC-ring inner diameter
Back-iron inner diameter	\varnothing_{bi}	62.6 mm	New SMC-ring inner diameter
Back-iron outer diameter	\varnothing_{bo}	70 mm	SMC-ring outer diameter
Max relative amplitude	$x_{rel,max}$	15.9 mm	Max. allowed seal speed
Remanent flux density	B_r	1.14 T	B_r of NdFeB magnets
Average radial flux density	\overline{B}_{rad}	0.3 T	Flux distribution model
Average back-iron flux density	\overline{B}_{BI}	1.3 T	Flux distribution model
Electric machine max. temp.	$T_{max,el}$	155 °C	PA66 max. temp.
Number of magnets	n_m	10	Length limitation
Number of coils	n_c	9	Length limitation
Copper wire height	h_c	2.35 mm	Optimal available solution
Copper wire thickness	w_c	1.85 mm	Optimal available solution
Number of turns per coil	n_c	54	Optimal available solution
Number of gas springs	n_{GS}	4	Separate gas spring chambers
Gas spring piston area	A_{GSP}	31.2 cm ²	Separate gas spring chambers
Piston mass	m_p	8.60 kg	From technical drawings
Stator mass	m_s	17.58 kg	From technical drawings
Max. gas spring pressure	p_{max}	> 30 MPa	Steel chambers

Table 4-6: Machine parameters updated according to design requirements.

5 System analysis and performance expectations

With the use of the theoretical background and system understanding presented in chapter 3, and the design parameters derived in chapter 4, this chapter presents an analytical approach to derive the performance of 2B.

Power losses as a function of stator current are derived. Resonance frequency is set to 100 Hz in this analysis. Qualified assumptions for system efficiency and maximum stator current and voltage are made. Values for thrust force and energy per blow are estimated.

For analyzing the resonance frequency, the moving mass must be defined. This chapter includes the description of a moving mass equivalent, which is used in a simulation of resonance frequency and maximum gas spring pressure depending on initial gas spring pressure.

5.1 Power loss and efficiency calculations

The efficiency of the machine is critical to its performance. Low efficiency leads to high temperature despite low current. Higher efficiency allows a higher power output. This sub-chapter discusses power losses in copper and iron as a function of stator current I . Friction losses and heat transfer are also discussed.

Accurate values are difficult to state. Only general simplifications are used here. All loss calculations are based on the assumption that the machine operates under steady-state conditions with $f = 100$ Hz electrical and mechanical frequency and a variable applied AC current $i(t)$.

5.1.1 Copper losses

The simplified way to estimate the copper power loss is:

- Calculate the DC power loss based on copper wire resistivity and geometrical parameters.

- Calculate AC resistance component. The coils do not experience a sinusoidal magnetic field change, which increases the uncertainty of the result.
- State power loss in the copper wire as a function of stator AC current i .

For the rectangular wire used, the DC resistance is at 25 °C is $R_{DC,25} = 0.334 \Omega$. The DC resistance value compensated for temperature increase to the maximum allowed temperature in the electric machine is $R_{DC,150} = 0.497 \Omega$ (Appendix B.7). For copper, skin depth is $\delta_c = 6.58$ mm at $f = 100$ Hz. For the rectangular wire used, $k_c = 0.0012$ (Appendix B.8). The total copper wire resistance is then:

$$R_{TOT} = R_{DC,150}(1 + k_c) = 0.497 \Omega(1 + 0.0012) = 0.497 \Omega \quad (5-1: \text{Total copper wire resistance})$$

Copper power loss can be expressed as:

$$P_{L,C} = i^2 R_{TOT} \quad (5-2: \text{Copper power loss})$$

5.1.2 Iron losses

Iron losses in the magnet separators are considered negligible compared to copper losses and back-iron losses in the SMC material. Also; the SMC-rings are assumed to conduct the entire return flux, not allowing the magnetic field to enter the outer steel casing. Hence; iron losses is estimated through assuming an average back-iron \vec{B} -field, varying with frequency.

Table 4-3 states that $f = 100$ Hz yields a back-iron copper loss of 13 W / kg for a variable magnetic flux $\vec{B} = 1.0$ T. It is fair to assume that a magnetic flux density back-iron average $\bar{B}_{BI} = 1.3$ T results in a loss increase of approx 50 %, therefore the back-iron power loss per kg mass is set to 20 W / kg. Total mass of the 24 SMC rings used is 3.60 kg, so the back-iron loss at target frequency is:

$$P_{L,I} = P_{L,B} / m_{SMC} \cdot m_{SMC} = 20 \text{ W/kg} \cdot 3.6 \text{ kg} = 72 \text{ W} \quad (5-3: \text{Back-iron loss})$$

5.1.3 Magnet piston friction loss

Power losses as a result of gliding friction (appendix A.3) will occur between the piston and the stator. Both the friction coefficient and the normal force between magnet piston and plastic tube are hard to quantify, due to possible radial misalignment and uncertainties regarding plastic surface and contaminating particles. Using grease or oil can reduce friction, but to an unknown extent. Therefore, the gliding friction loss is ignored in this discussion, well knowing that this loss can prove significant. The magnitude of the friction loss is best determined practically.

5.1.4 Heat transfer

The power losses in copper and back-iron are considered to be contributions to uniformly heat the mid section of 2B. The maximum allowed temperature in mid section is $T_{max} = 150\text{ °C}$, due to the plastic tube. The ambient temperature is assumed to be $T_A = 25\text{ °C}$, yielding $\Delta T_{max} = 125\text{ K}$. The mid section casing surface $A_C (= 0.154\text{ m}^2)$, excluding the connections to the gas springs on each end, emits heat energy to the surroundings. Typical values of heat transfer coefficients for similar linear machines are given by Wang (2011). Using fans to create a forced convection of the surrounding air yields a heat transfer per surface area and temperature difference of minimum $K_T = 20\text{ W} / (\text{m}^2 \cdot \text{K})$. An interesting comparison is a water cooled system typically exceeding $K_T = 100\text{ W} / (\text{m}^2 \cdot \text{K})$.

To hinder the temperature of the electric machine from exceeding the allowed $T_{max} = 150\text{ °C}$, the power loss must be transferred to the surroundings. The maximum allowed power loss in the electric machine $P_{L,EM,max}$ is equal to the heat power $|dQ_C/dt|_{max}$ emitted from the casing at maximum allowed machine temperature:

$$P_{L,EM,max} = P_{L,C,max} + P_{L,I} = \left| \frac{dQ_C}{dt} \right|_{max} = K_T \cdot A_C \cdot \Delta T_{max}$$

$$= 20\text{ W}/(\text{m}^2\text{K}) \cdot 0.154\text{ m}^2 \cdot 125\text{ K} = 385\text{ W} \quad (5-4: \text{Max. heat transfer emitted from casing})$$

5.1.5 Gas spring losses

The power loss in the gas springs $P_{L,GS}$ is radiated from the end sections, and not considered to contribute to the temperature increase in the electric machine.

The gas spring chambers are 24 mm in the neutral position. With an amplitude of 15.9 mm, as planned, the compression ratio is $(24 + 15.9) / (24 - 15.9) \approx 5$. During the first cycle initiated in room temperature at initial pressure, the minimum temperature at minimum pressure can be assumed quite low. The system will, however, become warmer. Given a very general assumption of an adiabatic process under such steady-state conditions, the minimum temperature can be set to $T_{GS,min} = 300\text{ °K}$, and the maximum temperature to $T_{GS,max} = 670\text{ °K}$ (Appendix B.11). Given the exponential growth of pressure and temperature during compression, it is fair to assume an average temperature in the gas spring chamber walls: $\bar{T}_{GS} = 450\text{ K}$, yielding a temperature difference to the surroundings of $\Delta T_{GS} = 152\text{ K}$. Using the same heat transfer factor as for the mid section and an estimated surface area A_{GSS} (Appendix B.10), the sum of heat transfer from the gas spring sections is:

$$P_{L,GS} = \frac{dQ_{GS}}{dt} = 20 \text{ W}/(\text{m}^2\text{K}) \cdot A_{GS} \cdot \Delta T_{GS}$$

$$= 20 \text{ W}/(\text{m}^2\text{K}) \cdot 51.9 \cdot 10^{-3} \text{ m}^2 \cdot 152 \text{ K} = 158 \text{ W} \quad (5-5: \text{ Gas spring losses})$$

The gas spring power loss is considered constant. The energy transferred in one cycle is:

$$E_{L,GS,C} = P_{L,GS} / f = \frac{158 \text{ W}}{100 \text{ Hz}} = 1.58 \text{ J} \quad (5-6: \text{ Energy transfer per period from gas springs})$$

The average damping force due to the gas spring power losses can be found by calculating the energy transferred through 1 cycle and using eq. 4-6:

$$\bar{F}_{d,GS} = \frac{E_{L,GS,C}}{4x_{max}} = \frac{1.58 \text{ J}}{4 \cdot 0.0159 \text{ m}} = 24.8 \text{ N} \quad (5-7: \text{ Average damping force due to gas spring power loss})$$

5.1.6 Total power loss as a function of stator current

The sum of power losses can be presented as a function of the main parameter affecting it; the stator current I :

$$P_L = P_{L,C} + P_{L,I} + P_{L,GS} = (i^2 0.497 + 72 + 158) \text{ W}$$

$$P_L(i) = [0.497 \cdot i^2 + 230] \text{ W} \quad (5-8: \text{ Total power loss})$$

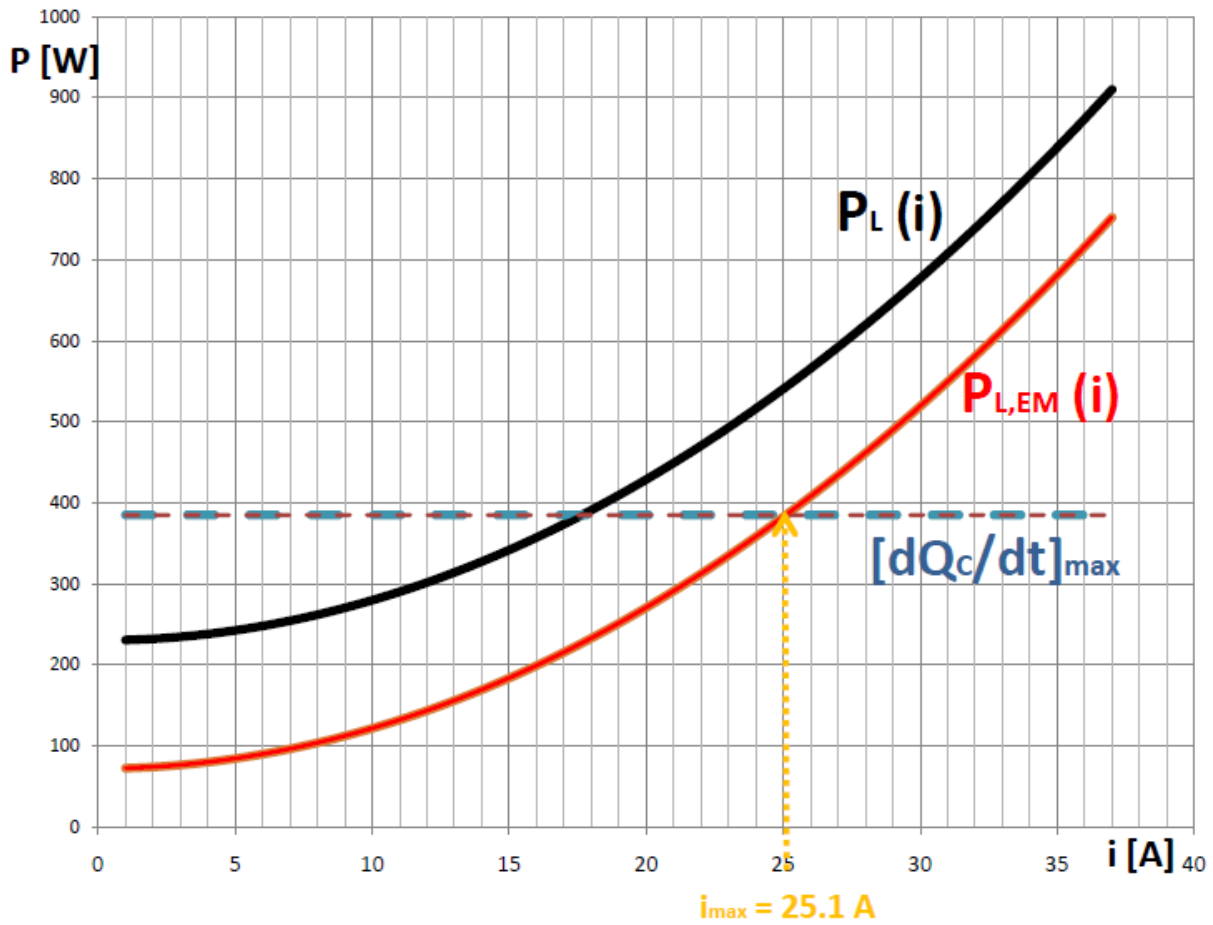


Figure 5-1: Total power loss P_L and power loss in the electric machine $P_{L,EM}$ (mid section) as functions of stator current i . Maximum heat transfer from mid section casing surface $[dQ_C/dt]_{max}$ limits the maximum electric machine power loss, and hence the maximum steady-state current i_{max} .

5.1.7 System efficiency

The system efficiency is the mechanical power output divided by the power input. The power that is not lost is transferred to the drill bit. The system efficiency as a function of input current i is then:

$$\eta = \frac{P_{out}}{P_{in}} = 1 - \frac{P_L}{P_{in}} = 1 - \frac{P_{L,C} + P_{L,I} + P_{L,GS}}{P_{in}}$$

$$\eta = 1 - \left(\frac{i^2 \cdot 0.497 + 230}{i \cdot u} \right)$$

(5-9: Current dependent efficiency)

5.2 Force output

Finally, the performance of 2B as a drill hammer can be calculated and presented as energy per blow and recommended hole-size diameter.

5.2.1 Stator current

Knowing the power losses and heat transfer, maximum stator current i_{max} can be found:

$$P_{L,C,max} = (i_{max})^2 \cdot R_{TOT} = P_{L,EM,max} - P_{L,I}$$

$$i_{max} = \sqrt{\frac{P_{L,EM,max} - P_{L,I}}{R_{TOT}}}$$

$$i_{max} = \sqrt{\frac{385 \text{ W} - 72 \text{ W}}{0.497 \Omega}} = 25.1 \text{ A} \quad (5-10: \text{Max stator current})$$

The maximum current density in the air gap between magnets and back-iron is then:

$$j_{G,max} = \frac{n_t \cdot i_{max}}{A_G} = \frac{54 \cdot 25.1 \text{ A}}{47 \text{ mm} \cdot 8 \text{ mm}} = 3.6 \text{ A/mm}^2 \quad (5-11: \text{Maximum current density})$$

Considering maximal values as 20 % overload, nominal values are set to:

$$i_N = 21 \text{ A} \quad j_{G,N} = 3.0 \text{ A/mm}^2 \quad (5-12: \text{Nominal current and current density})$$

5.2.2 Induced voltage and stator voltage

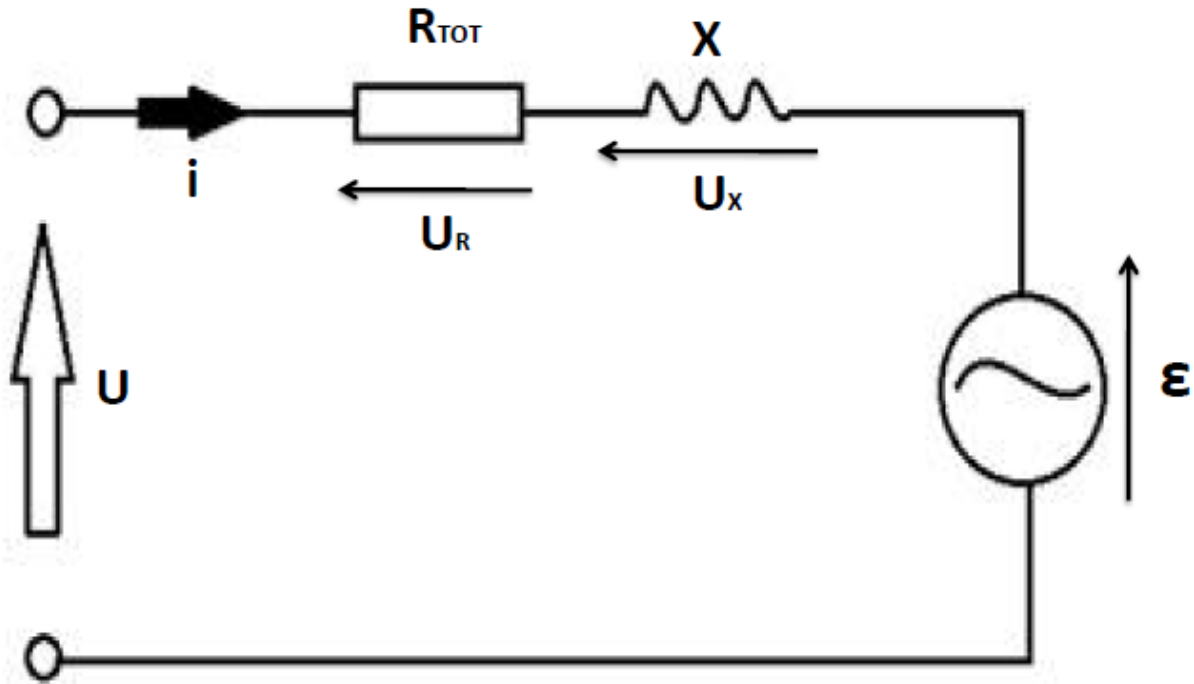


Figure 5-2: Representation of the motor for calculation of stator voltage.

The rms nominal stator AC voltage u_N is the sum of the voltage drop in the machine. Induced voltage ϵ and voltage drop u_R over the total resistance R_{TOT} are active components, and the voltage drop u_X over the reactance X is the reactive component.

The induced voltage ϵ in the conductors depends on relative speed v_{rel} , wire length of one coil l_C , number of modules n_m and the radial magnetic flux density B_{rad} . The rms-value, according to appendix D.1, is:

$$\epsilon_{rms} = \frac{\epsilon_{peak}}{\sqrt{2}} = \frac{294.9 \text{ V}}{\sqrt{2}} = 208.5 \text{ V} \quad (5-13: \text{Induced voltage, rms-value})$$

The voltage drop over R_{TOT} is:

$$u_R = R_{TOT} \cdot i_N = 0.497 \Omega \cdot 20 \text{ A} = 9.9 \text{ V} \quad (5-14: \text{Resistance voltage drop})$$

Average inductance in the coils is simulated and found to be $\bar{L} = 1.42 \text{ mH}$ (Jacobsen, 2011b). The voltage drop over X is then:

$$u_x = i_N X = i_N \omega \bar{L} = 20 \text{ A} \cdot 2\pi \cdot 100 \text{ Hz} \cdot 1.42 \text{ mH} = 17.8 \text{ V} \quad (5-15: \text{Reactive voltage drop})$$

Consequently, the nominal stator voltage is:

$$u_N = \sqrt{(\epsilon_{rms} + u_R)^2 + u_x^2} = \sqrt{(208.5 \text{ V} + 9.9 \text{ V})^2 + (17.8 \text{ V})^2}$$

$$u_N = 219.1 \text{ V} \quad (5-16: \text{Nominal stator voltage})$$

5.2.3 Thrust force

Using the derived values for nominal AC current density in the air gap j_{GN} , it is now possible to calculate the Lorentz' force pr machine module $\vec{f}_{L,M}$, varying with the current. Since the AC current j_N is given as an rms-value, the force can be considered an average force $\bar{F}_{L,M}$. See figure 4-6 for geometrical parameter reference.

$$\begin{aligned} \bar{F}_{L,M} &= \vec{f}_{L,M} = \bar{B}_r \times j_{G,N} \cdot t_G \tau_C \bar{O} \\ &= 0.31 \text{ T} \times 3.0 \text{ A/mm}^2 \cdot 8 \text{ mm} \cdot 47 \text{ mm} \cdot \pi \cdot 0.055 \text{ m} \\ \bar{F}_{L,M} &= 60 \text{ N} \end{aligned} \quad (5-17: \text{Lorentz' force pr machine module})$$

The magnetic force output pr electric machine length is then:

$$\begin{aligned} \bar{F}_{L,x} &= \bar{F}_{L,M} / \tau_P = 60 \text{ N} / 0.055 \text{ m} \\ \bar{F}_{L,x} &= 1.09 \text{ kN/m} \end{aligned} \quad (5-18: \text{Lorentz' force pr electric machine length})$$

The number of modules $n_m = 9$ already given, the total electromagnetic force is found to be:

$$\bar{F}_L = \bar{F}_{L,M} \cdot n_m = 57 \text{ N} \cdot 9 = 540 \text{ N} \quad (5-19: \text{2B total Lorentz' force})$$

The gas spring damping force acts opposite of the Lorentz' force, so the average thrust force $\bar{F}_{T,2B}$ is:

$$\bar{F}_{T,2B} = \bar{F}_L - \bar{F}_{d,GS} = 540 \text{ N} - 24.8 \text{ N} = 515 \text{ N} \quad (5-20: \text{2B average thrust force})$$

5.2.4 Energy pr blow

The energy per blow transferred to the drill bit, $E_{b,2B}$, can be found using eq. 4-4:

$$E_{b,2B} = \bar{F}_T \cdot 4x_{max} = 515 \text{ N} \cdot 4 \cdot 15.9 \text{ mm} = 32.8 \text{ J} \quad (5-21: \text{2B energy per blow})$$

5.2.5 Mechanical power output

At nominal frequency $f_N = 100 \text{ Hz}$, the mechanical power output is (eq. 4-2):

$$P_{out,2B} = E_{b,2B} \cdot f_N = 3.28 \text{ kW} \quad (5-22: \text{2B mechanical power output})$$

5.2.6 Hole-size

The average energy per blow per drill bit area (eq. 4-1) is $E_b/A_h = 0.04 \text{ J/mm}^2$. Hence, the suitable drill bit area for testing is:

$$A_{h,2B} = \frac{E_{b,2B}}{E_b/A_h} = \frac{31 \text{ J}}{0.04 \text{ J/mm}^2} = 820 \text{ mm}^2 \quad (5-23: 2B \text{ drill bit area})$$

The corresponding drill bit diameter is:

$$\varnothing_{h,2B} = 2 \cdot \sqrt{A_{h,2B}/\pi} = 2 \cdot \sqrt{775 \text{ mm}^2/\pi} = 32.3 \text{ mm} \quad (5-24: 2B \text{ hole diameter})$$

5.3 Moving mass equivalent theory

This sub-chapter is a description of a simplified and easy applicable analysis of the movement of stator and piston according to their respective masses.

5.3.1 Initial assumptions

- Steady-state no load operation in balanced resonance.
- Friction force and Lorentz' force are opposite and equal at all times: $\vec{F}_L(t) = -\vec{F}_f(t)$.
- Equal ideal springs in both ends.
- Gravity and suspension is ignored. The system can be thought of as acting in weightlessness, thus ignoring the surroundings.

Two reference frames are defined (Figure 5-3). The radial component is irrelevant, as all movement acts along the machine axis, in the x-direction. Reference frame G has a global origin, reference frame S has its origin connected to the stator.

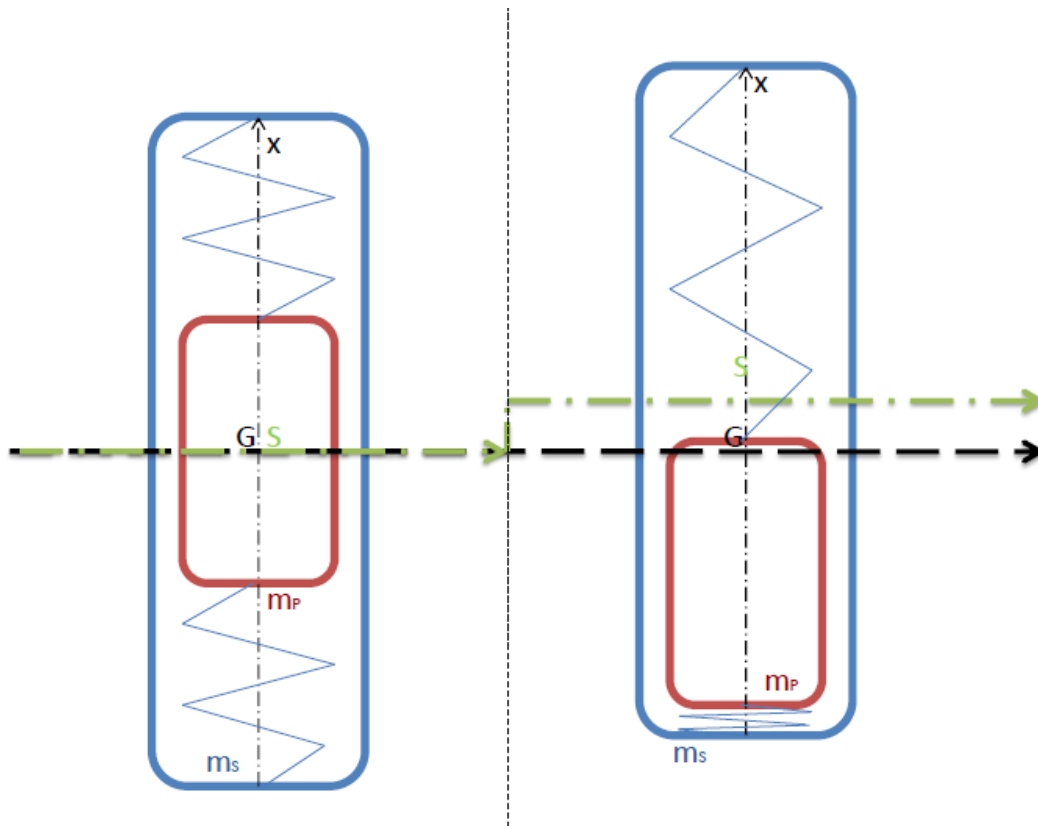


Figure 5-3: Global (G) and stator-bound (S) reference frames. Left: Neutral position / initial state. Right: Maximum amplitude.

Using the stator frame S , only the piston moves. This approach has proven useful for analyzing relative amplitude $x_{max,rel}$ between the stator and the piston. The moving mass of a free piston and free stator system has, however, not been defined.

In the global reference frame G there are two moving objects; piston and stator. Only by defining the stator as an object of infinite mass, G will equal S . Then the only moving mass is the piston mass m_p . The following analysis treats the system in the global reference frame G .

When allowing the stator to move, it is easier for a force to accelerate the piston relative to the stator, because the stator can also be moved. All forces act between the piston and the stator, always opposite in direction on the two objects. Logically, the moving mass used in eq. 3-17 is experienced as smaller, yielding a higher resonance frequency.

5.3.2 Analogy

The decrease of the moving mass can be viewed analogous to the parallel of two electric inductors. Inductors oppose a current change di/dt created by an applied voltage: $U = L di/dt$. Two inductors coupled in parallel allow a higher di/dt than any of the two alone. The inductance equivalent in a parallel circuit is (Paynter and Boydell, 2005):

$$L_{EQ} = \frac{L_1 L_2}{L_1 + L_2} \quad (5-25: \text{Inductance equivalent, parallel connection})$$

5.3.3 Statement

Equally, masses oppose a change in velocity $d\vec{v}/dt = \vec{a}$ created by an applied force $\vec{F} = m\vec{a}$.

A moving mass equivalent m_{EQ} can be suggested as a function of the two moving masses, m_p and m_s :

$$m_{EQ} = \frac{m_p m_s}{m_p + m_s} \quad (5-26: \text{Moving mass equivalent})$$

5.3.4 Mathematical proof

In 2B, energy is stored alternately as potential energy in the compressed gas springs E_{GS} , and as kinetic energy in the moving masses $E_{K,P}$ and $E_{K,S}$, depending on the displacement. Since power input balances power loss at all times, the total energy stored is constant:

$$E_{TOT} = E_{K,P} + E_{K,S} + E_{GS} \quad (5-27: \text{Stored energy})$$

All forces act between the two objects, so the relationship between acceleration and mass can be found with Newton's 2. and 3. law . It follows that $\vec{a}_p(t)$ acts in the opposite direction of $\vec{a}_s(t)$ at all times.

$$\vec{F} = m_p \vec{a}_p(t) = -m_s \vec{a}_s(t) \quad \rightarrow \quad -\frac{\vec{a}_s(t)}{\vec{a}_p(t)} = \frac{m_p}{m_s} \quad (5-28: \text{Acceleration/mass-relation})$$

The relative amplitude between piston and stator is always the difference between the stator and piston positions: $\vec{x}_{rel}(t) = \vec{x}_p(t) - \vec{x}_s(t)$. The relative speed is the absolute value of the difference between the velocities of piston and stator. Due to the oppositely acting force at all times, the movement of the objects are always 180° out of phase:

$$v_{rel}(t) = |\vec{v}_p(t) - \vec{v}_s(t)| = v_p(t) + v_s(t) \quad (5-29: \text{Relative speed})$$

Displacement $\vec{x}(t)$ and acceleration $\vec{a}(t)$ are easily associated due to the constant frequency $f \propto \omega$ of both objects (ref: eq. 3-4):

$$\vec{a}(t) = -\omega^2 \vec{x}(t) \quad (5-30: \text{Acceleration / displacement relation})$$

This allows comparing acceleration, velocity, speed and displacement to the relation of masses (ref: eq. 3-3, 3-4, 5-28 and 5-30):

$$\begin{aligned} \frac{m_p}{m_s} &= -\frac{\vec{a}_s(t)}{\vec{a}_p(t)} = -\frac{-\omega^2 \vec{x}_s(t)}{-\omega^2 \vec{x}_p(t)} = \frac{\vec{x}_s(t)}{\vec{x}_p(t)} = \frac{\vec{v}_s(t) \frac{\tan(\omega t)}{\omega}}{\vec{v}_p(t) \frac{\tan(\omega t)}{\omega}} \\ \rightarrow \quad \frac{m_p}{m_s} &= -\frac{\vec{v}_s(t)}{\vec{v}_p(t)} = \frac{v_s(t)}{v_p(t)} \end{aligned} \quad (5-31: \text{Mass /speed relation})$$

The total kinetic energy in the system is proposed described with the equivalent mass m_{EQ} and the relative speed $v_{rel}(t)$, equal to the sum of the kinetic energy of the two moving masses:

$$E_{K,TOT} = \frac{1}{2} m_{EQ} v_{rel}(t)^2 = \frac{1}{2} m_p v_p(t)^2 + \frac{1}{2} m_s v_s(t)^2 \quad (5-32: \text{Total kinetic energy})$$

Using the mass- and speed relations, appendix B.3 shows that the equivalent mass used to describe the total kinetic energy of the system is $m_{EQ} = \frac{m_p m_s}{m_p + m_s}$, as stated.

The relation of kinetic energy of the two masses is calculated using the relation of masses and speeds:

$$\begin{aligned} E_{K,P} &= \frac{1}{2} m_p v_p(t)^2 = \frac{1}{2} m_s \frac{v_s(t)}{v_p(t)} v_p(t)^2 = \frac{1}{2} m_s v_s(t)^2 \frac{m_s}{m_p} = E_{K,S} \frac{m_s}{m_p} \\ \rightarrow \quad \frac{m_p}{m_s} &= \frac{E_{K,S}}{E_{K,P}} \end{aligned} \quad (5-33: \text{Mass / kinetic energy relation})$$

In the neutral position ($x = 0$), the gas springs have an equal pressure. The acceleration is zero, and the speed is at maximum value v_{max} . At $x = 0$, all stored energy is the kinetic energy of the two moving masses. Given the initial circumstance, the stored energy is constant, so this can be used to calculate the total energy at any time:

$$E_{TOT} = |E_{TOT}|_{x=0} = |E_{K,TOT}|_{x=0} = \frac{1}{2} m_{EQ} (v_{rel,max})^2 \quad (5-34: \text{Total stored energy})$$

5.3.5 Analytical verification

Resonance frequency can be predicted using the mass equivalent in eq. 3-17:

$$f_0 = \frac{1}{2\pi} \sqrt{k_{GS}/m_{EQ}} \quad (5-35: \text{Res. frequency described with mass eq.})$$

An analytical script by Grinde (2011), based on basic laws of mechanical motion is attached in chapter 10.4. Using the same gas spring stiffness constant $k_{GS} = 5 \cdot 10^6 \text{ kg/s}^2$, a constant stator mass and variable piston mass, both methods yield comparable results when calculating resonance frequency (Table 5-1). The relation of piston mass and stator mass ranges from 1/20 to 7/4.

m_S [kg]	m_P [kg]	Resonance frequency according to mass equivalent [Hz]	Numerical estimation of resonance frequency [Hz]	% diff
20	1	364.7	360.0	1,3
20	5	177.9	180.0	-1,1
20	10	137.8	139.9	-1,5
20	15	121.6	119.9	1,4
20	20	112.5	109.9	2,4
20	25	106.8	110.0	-2,9
20	30	102.7	100.0	2,7
20	35	99.8	100.0	-0,2

Table 5-1: Resonance frequencies for various piston masses. Results according to the moving mass equivalent compared to a numerical estimation based on equations of mechanical motion. Script available in chapter10.4.

Table 5-1 shows deviations of < 3 % when comparing the calculated frequency according to the moving mass equivalent theory to the numerical estimation based on the laws of mechanical motion. This result implies that the moving mass equivalent is applicable in analyses of this system of two related moving masses.

5.3.6 Some parameters decided by application of the mass equivalent theory

Using stator mass (Appendix B.13) and piston mass (Appendix B.14) the moving mass equivalent of 2B is:

$$m_{EQ,2B} = \frac{m_P m_S}{m_P + m_S} = \frac{8.60 \text{ kg} \cdot 17.58 \text{ kg}}{8.60 \text{ kg} + 17.58 \text{ kg}} = 5.78 \text{ kg} \quad (5-36: 2B \text{ moving mass equivalent})$$

The total energy stored in the system is:

$$E_{TOT} = \frac{1}{2} m_{EQ} (v_{rel,max})^2 = \frac{1}{2} \cdot 5.78 \text{ kg} \cdot (10 \text{ m/s})^2 = 289 \text{ J} \quad (5-37: 2B \text{ stored energy})$$

The hammer amplitude is (see B.4):

$$x_{S,max} = x_{rel,max} \frac{m_P}{m_S + m_P} = 15.9 \text{ mm} \frac{8.60 \text{ kg}}{26.18 \text{ kg}} = 5.2 \text{ mm} \quad (5-38: 2B \text{ hammer amplitude})$$

5.4 Resonance frequency simulation

Using the stated relations describing gas compression dynamics, Li (2011a) has conducted simulations for estimating the resonance frequency of 2B during operation. Parameters decided during the design process are being used as input values:

- Gas spring piston area $A_{GSP} = 3.12 \cdot 10^{-3} \text{ m}^2$.
- Gas spring chamber length $x_{GSC} = 24 \text{ mm}$.
- Moving mass $m = m_{EQ,2B} = 5.78 \text{ kg}$.

Other assumptions are:

- Helium as gas spring medium. Considered a monatomic ideal gas, helium has a polytropic coefficient $\gamma_{He} = 5/3$.
- Only two gas springs are used.
- Friction is neglected.

The simulation results, presented graphically in appendix D.2, indicate resonating frequency plotted for different initial gas pressures. An initial pressure $p_0 = 6.0 \text{ MPa}$ yields an operating frequency exceeding the target frequency $f = 100 \text{ Hz}$.

Assuming amplitude $x_{rel,max} = 15.9 \text{ mm}$ yields the compression factor $k_{comp} < 1$ describing gas spring volume at maximum compression V_{min} compared to initial gas spring volume V_0 :

$$k_{comp} = \frac{V_{min}}{V_0} = \frac{x_{GSC} - x_{rel,max}}{x_{GSC}}$$

$$\rightarrow k_{comp} = \frac{24 \text{ mm} - 15.9 \text{ mm}}{24 \text{ mm}} = 0.3375 \quad (5-39: \text{Compression factor})$$

Deciding the nominal initial pressure to be $p_{0,N} = 6.0 \text{ MPa}$, and assuming no losses or leakages, the maximum pressure can in this case be calculated according to the adiabatic relation between pressure and volume:

$$\frac{p_{max}}{p_0} = \frac{(V_0)^\gamma}{(V_{min})^\gamma} = \frac{1}{(k_{comp})^\gamma}$$

$$\rightarrow p_{max} = \frac{6.0 \text{ MPa}}{(0.3375)^{5/3}} = 36.7 \text{ MPa} \quad (5-40: \text{Max. gas spring pressure})$$

Appendix D-3 shows resonance frequency plotted for different gas spring chamber lengths. Initial pressure $p_0 = 3.0 \text{ MPa}$ is equal for all chamber lengths. Generally; when doubling the chamber length, and hence the volume, the resonance frequency decreases by the factor 1.4. According to Xiao (2010), this would have to be compensated for by increasing the initial

pressure with a factor $1.4^2 \approx 2$, in order to maintain the same resonance frequency with the same amplitude. In other words; with constant resonance frequency and chamber length there seems to be a 1:1 relation between a change of chamber length x_{GSC} and a compensating change of initial pressure p_0 .

Increasing chamber length and assuming unchanged amplitude and frequency, the compression factor increases. Because of the polytropic coefficient, an increasing $k_{comp} \rightarrow 1$ constitutes a comparably more significant decrease in the pressure relation.

In this special case, increasing the chamber length to the proposed $x_{GSC} = 36$ mm, would require an initial pressure of $p_0 = 9.0$ MPa. The pressure at maximum compression would be $p_{max} = 23.8$ MPa (B.14). This indicates that the alternative chamber length would provide better working conditions for the dynamic seals.

6 Discussion

The presented design and theory of the two previous chapters contain many arguments and discussions. The 2B design is complex, and assessing alternatives yields interesting discussions concerning every detail. Emphasized discussion themes are summarized in this chapter.

6.1 Mechanical design

The separate gas spring chambers topology has many advantages compared to the previous design:

- Higher gas spring pressures are tolerated
- The working conditions for the dynamic seals are improved.
- The piston area and the number of gas springs increase.
- The mechanical stability of the piston rod is improved.

The increased machine length and mass, in addition to the topological complexity are minor disadvantages in comparison. The separate gas spring chamber topology can become the most important contribution for achieving high hammering frequencies.

The gas spring seal system must be considered experimental, and the performance is hard to predict. Theoretically; if the inside chamber surface roughness is very low, and the piston fits perfectly, the result should be satisfying.

The maximum gas spring pressure is an important parameter. Analyses of resonance frequency simulations imply that using the longer alternative of the two proposed gas spring chambers results in a lower maximum pressure. The seals will have a greater chance of containing the pressurized gas with a lower maximum pressure. On the other hand; the total machine length should be kept as small as possible.

The plastic tube stator support is a mechanical weakness, due to loss of copper volume, high inner surface roughness, relatively low tolerance for mechanical impact and low tolerance for temperature increase. Alternative solutions might be required.

6.2 Electromagnetic design

The electromagnetic design aims to achieve a target performance comparable to Wassara drill hammer products. The electric machine part of the 2B prototype consists of several readily available parts, and the basic structure is a further evolution of earlier design. This was believed to fulfill the target performance, but restraints to machine dimensions and achievable power density limits the output power of 2B to approx. $\frac{1}{2}$ of the desired quantity. Consequently, testing of the prototype can be performed with suitably smaller drill bit diameters.

There are several ways to increase the power density. A system with forced water-cooling will transfer heat more effectively than the fan-cooled type presented here. This increases the allowed current density, and hence the power output. Also, a three-phase topology has not been discussed for 2B, but using 3 phases would increase the utilization of the windings, and hence the power density.

For the chosen wire type, AC resistance seems to be an irrelevant issue. The rectangular shape of the wire yields a high fill factor. Additionally, the wire dimensions result in a number of turns very close to what is predicted suitable for yielding the desired stator voltage of $u < 230$ V. The chosen wire type seems therefore fit for the application.

The estimated maximum magnetic field density in the back-iron is approx 1.8 T. This high value can result in unnecessary high iron losses. The high flux density also indicates that a significant leakage flux will occur. A thicker back-iron layer, in the radial direction would result in more moderate values and lower iron losses.

The estimations on power loss are not very accurate, because of their complexity. The complexity of the mechanical interface between piston and plastic tube makes power loss estimation difficult, and therefore ignored in this thesis. Nevertheless, friction losses will inevitably occur. There are two ways of estimating efficiency; simplified to a function of input current; or based on comparing estimated input and output power. The calculation in appendix B.15 shows that these methods yield ambiguous results. This implies that the general assumptions, as well as the calculations on power loss and performance, made in the course of this thesis, should be further refined.

The parameters estimated are presented in appendix D-4. These can be used as indications to dimensioning of the test equipment.

6.3 Moving mass analysis

The theory of the moving mass equivalent provides a method for brief and simple calculations of important machine parameters. It is stated that through the relation of piston mass versus stator mass, corresponding time-dependent relations for these parameters can be found:

- Displacement.
- Speed.
- Acceleration.
- Kinetic energy.

The moving mass equivalent can be used for calculations of:

- Total kinetic energy. Calculating for $x = 0$ yields total stored energy of the system.
- Resonance frequency. $m_{EQ} < m_P$, so according to Xiao et. al (2010) the resonance frequency is bigger in a system where both stator and piston are free to move.

A correlating comparison to numerical values based on the laws of mechanical movement implies the validity of the moving mass equivalent theory.

The initial assumptions of the moving mass equivalent theory limit the extent of validity. There will be friction and non-linearities in the relations of force, displacement, speed and acceleration. Also, two gas springs can never be exactly equal, and external forces will occur. Adapting the mass equivalent theory to be valid for a load simulation, will require implementation of a mathematical representation of the load for a further refinement of the theory.

7 Conclusion

7.1 Design and assembly

Standing on the shoulders of earlier development, the design for a high frequency drill hammer prototype, named 2B, has been described. Alternate solutions have been discussed for possible re-design and considerations in later work. Guidelines for assembling the machine parts were proposed.

7.2 Performance

Assumed performance, in terms of power input and output, resonance frequency and recommended bit size, have been calculated. Design and performance parameters are collected in a datasheet draft (see appendix D-4).

The results imply that 2B will be able to perform high hammering frequencies, and is therefore suitable for testing the results of increasing frequency in hammer drilling. The obtainable power output comparable to existing drill hammers. Cooling methods and use of three-phase windings can enhance the force density considerably.

7.3 Applicable analysis method

A new theory of a moving mass equivalent, valid for a no-load ideal operation case, has been proposed. This theory yields a method to compare the motion of two coupled objects to the masses of the objects. The method also contributes to simpler calculations of resonance frequency and stored energy in present and future Resonator prototypes and applications.

This method has been theoretically substantiated, and verified in comparison to analytical methods.

7.4 Epilogue - Further work

Completing the building of the 2B prototype succeeds the submission of this thesis with a matter of weeks. Validation of the suggested performance parameters, and exploring the functionality of the chosen design, must be done through extensive practical testing. Testing, followed by thorough test analyses should be completed before deciding details on the next evolutionary step of the Resonator concept.

Testing of 2B during no-load operation can verify the validity of the mass equivalent theory. The method can be further refined for approaching valid analyses of actual operation of 2B, or similar machines, by mathematically defining the external load experienced during drill hammer operation.

Reference list

2009. W50_0902 / W80_0902. *In*: WASSARA (ed.). Wassara.
- ÅM, K., AL-KASIM, F., BJERKEDAL, N., GJERDSETH, A. C., KINDEM, S. E., SKAUGE, A., SKJÆRPE, T., SUND, B. A., SÆTRE, J. J. & WIBORG, R. 2010. Økt utvinning på norsk kontinentalsokkel. Oslo: Olje- og Energidepartmentet.
- BARTNIK, M. 2006. *Percussion hammers for hard rock drilling*. Master, NTNI.
- BERGE, E. A. 2005. *Design of a reciprocating linear synchronous machine*. Master, Norwegian University of Science and Technology.
- BOLDEA, I. & NASAR, S. A. 1997. *Linear Electric Actuators and Generators*, Cambridge, U.S.A., Cambridge University Press.
- BOSTAD, A. & LI, P. 2010. Test no 2: pressure vs resonance frequency. Ås: University of Life Sciences.
- BRENNVALL, J. E. & NILSSEN, R. 2005. *Working machine with an electromagnetic converter*. International patent application.
- BRENNVALL, J. E. & NILSSEN, R. 2010. *Working machine with an electromagnetic converter.pdf*. US patent application 10/584,802.
- DAHLSTRÖM, M. 2011. Type to BOSTAD, A.
- DAHRENTRÅD 2011. damid e_0904. *In*: DAHRENTRÅD (ed.). Jonslund.
- DAVIDDARLING.INFO. 2011. www.daviddarling.info/encyclopedia/H/hysteresis_loop.html [Online]. [Accessed 28.04.11 2011].
- DONAHUE, J., BEAN, A., WILLIAMS, R. A., TILLEY, D. G., DARLING, J. & GAO, B. 2005. Non-linear modelling of a novel gas strut. *Proceedings of the Institution of Mechanical Engineers, Part D: Journal of Automobile Engineering*, 219, 1153-1164.
- EL SHAHAT, A., KEYHANI, A. & EL SHEWY, H. 2010. Sizing a High Speed PM Generator for Green Energy Applications. *Journal of electrical systems*, 6, 16.
- EVENSEN, J. E., AALHUS, J. N., BERRE, I., BERGAN, H., KLEVEN, P. H., NÆSS, E., OLESEN, O. & ØSTHASSEL, E. 2010. Energi 21. Innsatsgruppe fornybar energi.
- GREEN, S., JUDZIS, A., CURRY, D., CHRISTENSEN, H., BLACK, A., PRASAD, U. & ROGERS, J. 2005. Single cutter impact tests investigate deep-well hammer-drilling performance. *SPE annual technical conference and exhibition*. Dallas, Texas.
- GRINDE, C. 2011. Analytical script of 2B motion. Asker: Resonator.

- HAN, G., BRUNO, M. & LAO, K. 2005. Percussion drilling in oil industry: Review and rock failure modelling. *American Association of Drilling Engineers 2005 National Technical Conference and Exhibition*. Houston, Texas: Terralog Technologies.
- HANSELMAN, D. C. 2006. *Brushless permanent magnet motor design*, The Writers` Collective.
- HÖGANÄS 2009. *Processing_Guidelines_Somaloy_3P_materials_2009_09*.
- HÖGANÄS. 2011a. *Somaloy technology* [Online]. Höganäs. [Accessed 01.04.2011 2011].
- HÖGANÄS 2011b. Summary Resonator batch1.
- HUNTSMAN 2007. Araldite 2014 data-sheet. *In: MATERIALS*, H. A. (ed.). The Woodlands, Texas.
- JACOBSEN, A. D. 2011a. Design evaluation of a reciprocating TLPMSM. Asker: Resonator AS.
- JACOBSEN, A. D. 2011b. New design of a reciprocating TLPMSM. *Resonator prototype*. Asker: Resonator AS.
- JACOBSEN, A. D. 2011c. New design of a reciprocating TLPMSM. Bærum: Resonator AS.
- JACOBSEN, A. D. 2011d. repelling force between magnets. Asker.
- JAILLOT, C. 2008. Instrumentation and testing of linear motor prototypes. Trondheim: NTNU.
- LAITHWAITE, E. R. 1975. Linear electric machines - a personal view. *IEEE*, 63, 41.
- LI, P. 2011a. Resonance frequency simulation. Asker: Resonator AS.
- LI, P. 2011b. Resonator 2B drawings. Asker: Resonator AS.
- LOCTITE 2003. loctite_3421. *In: CORPORATION*, H. L. (ed.). Dublin, Ireland.
- LU, Z. H. & CHANG, F. 2008. Dynamic model of an air spring and integration into a vehicle dynamics model. *Proceedings of the Institution of Mechanical Engineers, Part D: Journal of Automobile Engineering*, 222, 1813-1825.
- LUO, G., ZHANG, Y., XIE, J. & ZHANG, J. 2007. Vibro-impact dynamics near a strong resonance point. *Acta Mechanica Sinica*, 23, 329-341.
- NILSSEN, R. K. 2008. *Electromagnetics in power engineering*, Trondheim, NTNU - Department of Electrical Power Engineering.
- PACK-FEINDRAEHTE.DE. 2011. *pack-feindraehte* [Online]. Available: www.pack-feindraehte.de [Accessed 21.04.2011 2011].
- PAYNTER, R. T. & BOYDELL, B. J. T. 2005. *Electronics technology fundamentals*, New Jersey, Pearson Prentice Hall.
- RAMSDEN, E. 2006. *Hall-effect sensors: theory and applications*, Oxford, Newnes.
- SCHROEDER, D. V. 2000. *An introduction to thermal physics*, San Fransisco, California, Robin J. Heiden, Addison Wesley Longman.
- STEFANSSON, V. 2005. World geothermal assessment. *World geothermal congress*. Antalya, Turkey.

- SURAMAGNETS. 2011. *magnetiska material* [Online]. Sura Magnets AB. Available: http://suramagnets.se/se/produkter_och_tjanster/magnetiska-material/#ndefebmagneter [Accessed 01.04.2011 2011].
- TEODURIO, C. & CHEUFFA, C. 2011. A comprehensive review of past and present drilling methods with application to deep geothermal environment. *Workshop on geothermal reservoir engineering*. Stanford, California.
- TIPLER, P. A. & MOSCA, G. 2008. *Physics for scientists and engineers*, New York, W.H. Freeman and company.
- TOPANELIAN, E. J. 1958. Effect of low frequency percussion in drilling hard rock. *Annual fall meeting of society of petroleum engineers*. Dallas.
- TRELLEBORG 2010. in the groove all industries. *In: TRELLEBORG (ed.)*.
- UMMANENI, R., JAILLOT, C., NILSSEN, R. & BRENNVALL, J. E. 2009. Experimental characterisation of linear permanent magnet actuator with gas springs. *Electric Machines and Drives Conference*. IEEE International.
- UMMANENI, R., NILSSEN, R. & BRENNVALL, J. 2008. Demonstration Model of a Linear Permanent Magnet Actuator with Gas Springs. *International conference on electrical machines*. Vilamoura.
- VINK 2010. teknisk datablad PEEK. *In: AS, V. (ed.)*. Randers.
- WANG, J. 2011. *RE: Discussion between C. Grinde, A.D. Jacobsen and J. Wang*. Type to JACOBSEN, A. D.
- WANG, J., WEST, M., HOWE, D., LA PARRA, H. Z.-D. & ARSHAD, W. M. 2007. Design and experimental verification of a linear permanent magnet generator for a free-piston energy converter. *IEEE*, 22, 8.
- WILDI, T. 2006. *Electrical Machines, Drives and Power Systems*, USA, Pearson Prentice Hall.
- XIAO, J., LI, Q. & HUANG, Z. 2010. Motion characteristic of a free piston linear engine. *Applied Energy*, 87, 1288-1294.
- ZHANG, S. 2009. Oscillatory motion application of tubular linear permanent magnet machine. *IECON '09*. IEEE.

Appendices

A Basic theory

A.1 Newton`s 2. law

The acceleration \vec{a} of an object with mass m is directly proportional to the net force \vec{F} acting on it. The mass of the object is the constant of proportionality (Tipler and Mosca, 2008):

$$\vec{F} = m\vec{a} \quad (0-1)$$

A.2 Newton`s 3. law

When a force \vec{F}_{12} is exerted by object 1 on object 2, a force \vec{F}_{21} , equal in magnitude and opposite in direction, is exerted by object 2 on object 1 (Tipler and Mosca, 2008):

$$\vec{F}_{12} = -\vec{F}_{21} \quad (0-2)$$

A.3 Friction force

Static friction force f_{Sf} hinders two surfaces in contact from relative movement, in spite of an exerted force F_e acting in a direction such as to cause a relative movement. It is proportional to the normal force F_N pressing the surfaces together and the material-, area- and temperature-dependent coefficient of static friction μ_{Sf} (Tipler and Mosca, 2008):

$$f_{Sf} \leq f_{Sf,max} = \mu_{Sf}F_N \quad (0-3)$$

When $F_e > F_{Sf,max}$, the static friction is zero.

Kinetic friction force f_{Kf} is the force acting to oppose the motion between two surfaces in contact. It is proportional to the normal force F_N and the material-, area- and temperature-dependent coefficient of kinetic friction μ_{Kf} (Tipler and Mosca, 2008):

$$f_{Kf} = \mu_{Kf}F_N \quad (0-4)$$

A.4 Work, power and force

Work W is energy transferred into or out from a system (Schroeder, 2000). Work can be expressed as the integral of an exerted variable power $p(t)$ during the time dt (Tipler and Mosca, 2008):

$$W = \int p(t) dt \quad (0-5)$$

Work can also be expressed as the integral of the variable force $f(x)$ exerted on an object being displaced a distance dx (Tipler and Mosca, 2008):

$$W = \int f(x) dx \quad (0-6)$$

A.5 Magnetic flux density

The magnetic flux density \vec{B} [T] is the amount of magnetic flux Φ [Wb] flowing through the area element dA [m²] on the surface S . \hat{n} is the normal vector to the surface (Tipler and Mosca, 2008):

$$\Phi = \int_S \vec{B} \cdot \hat{n} dA \quad (0-7)$$

The field strength H [A/m] is the intensity change of the magnetic field due to the interaction of \vec{B} with the material it encounters. μ [H/m] is the magnetic permeability of the material (Hanselman, 2006).

$$\vec{B} = \mu \vec{H} \quad (0-8)$$

The relative permeability $\mu_r = \mu / \mu_0$, defines a given material's ability to conduct magnetic flux. The magnetic constant $\mu_0 = 4\pi \cdot 10^{-7} \text{ H/m}$ is equal to the permeability μ of vacuum.

A.6 Biot-Savart law

The magnetic field $d\vec{B}$ produced by a current element $I d\vec{l}$ [Am] depends on the permeability μ of the surrounding material, and has a revolving direction perpendicular to the current direction. In a distance r [m] from the current element, the magnetic flux density due to the current element is (Tipler and Mosca, 2008):

$$d\vec{B} = \frac{\mu}{4\pi} \frac{I d\vec{l} \times \hat{r}}{r^2} \quad (0-9)$$

A.7 Ohm`s law for magnetic circuits

An analysis of the magnetic circuit can be viewed analogous to an electric circuit. Both magnetic flux Φ and current I [A] can be defined as flow in a closed path. As electromotive force, voltage U [V] is the driving force of the current I , constrained by the electric resistance R_{el} [Ω] of the electrically conducting material. Analogous; the magnetomotive force F_{MMF} [A] is the driving force of the magnetic flux Φ , constrained by the magnetic reluctance R_m [$A/Wb = 1/H$] of the magnetically permeable material. This is expressed in Ohm`s law for magnetic circuits (Hanselman, 2006):

$$F_{mmf} = \Phi R_m \quad (0-10)$$

A.8 Magnetic permeance and reluctance

Permeance P_m [H] defines the ability to convey magnetic flux for a material of a defined volume. It is a product of the materials permeability μ on the volume defined by the cross section A (normal to the direction of the magnetic field) over the length l [m] Permeance can also be described as the inverse of reluctance (Hanselman, 2006):

$$P_m = \mu A / l = 1 / R_m = \Phi / F_{mmf} \quad (0-11)$$

A.9 Faraday`s law

A change in magnetic flux $d\Phi/dt$ [$\frac{Wb}{s}$] perpendicular to the plane enclosed by an electrical wire of N turns causes an induced voltage ε [V] between the connection points (Wildi, 2006):

$$\varepsilon = -N \frac{d\Phi}{dt} \quad (0-12)$$

A.10 Electric linear machines

Electric linear machines move along one axis, in one or both directions. The same basic energy conversion principles apply for linear machines as for rotary machines. Laithwaite (1975) defines the elementary difference: "A linear motor can be defined as being the result of a cylindrical rotary machine which has been mentally split along a radial plane an unrolled." Re-rolling the stator on a perpendicular axis creates a classical tubular design, as shown in Figure 0-1.

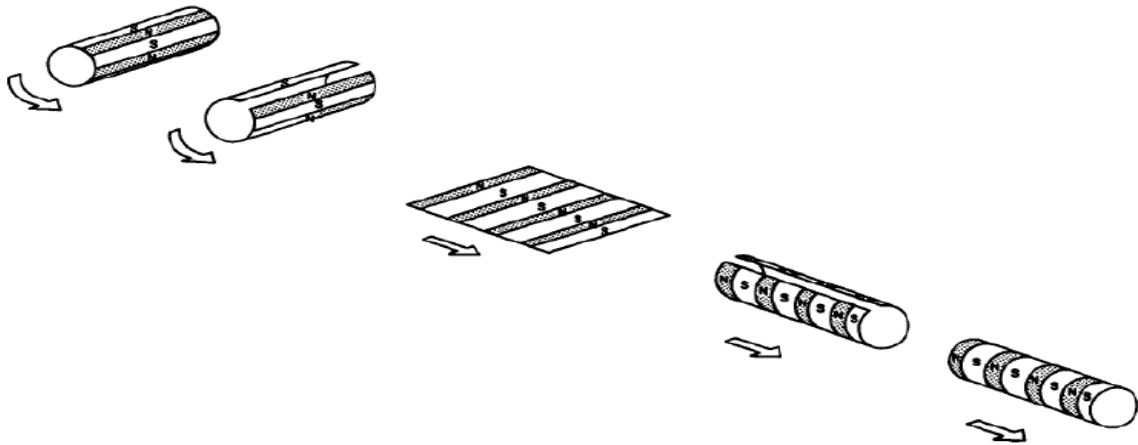


Figure 0-1: The difference of linear machines versus rotary machines can be thought as splitting the stator and unrolling it (Boldea and Nasar, 1997).

A.11 Lenz' law

The negative sign in Faraday's law is understood by means of Lenz's law: "The induced voltage ε acts in such a direction as to oppose the motion or change causing it." (Tipler and Mosca, 2008).

A.12 Voltage induced in a conductor

A relative motion between current-carrying coils and a magnetic field yields an opposing reaction according to Lenz' law. Described with reference to the conductors, the induced voltage ε , called back-emf, is the product of the magnetic flux density B , the active conductor length l , and the relative speed $v_{rel}(t)$ (Wildi, 2006):

$$\varepsilon = B \cdot l \cdot v_{rel}(t) \quad (0-1)$$

A.13 Fill factor

Using copper, the geometrical dimensions define the differences in resistance of conductor types. As long as the number of turns is given, the fill factor FF can be used to compare DC resistance. Here, the fill factor is defined as the sum of copper cross section area A_C divided by the total cross section area of the air gap between rotor and back-iron A_G , alternatively the sum of copper volume V_C divided by air gap volume V_G :

$$FF = \frac{\sum A_C}{A_G} = \frac{\sum V_C}{V_G} \quad (0-2)$$

A.14 Efficiency

The efficiency of a converter describes its ability to transfer input from a source to the converted output. In this context both energy $E[\text{J}]$ and power $P[\text{W}]$ can be used as parameters:

$$\eta_E = \frac{E_{out}}{E_{in}} \quad \eta_P = \frac{P_{out}}{P_{in}} \quad (0-3)$$

For a given time span of steady-state operation these efficiencies are equal.

The difference between input and output is the energy or power lost during conversion:

$$E_{loss} = E_{in} - E_{out} \quad P_{loss} = P_{in} - P_{out} \quad (0-4)$$

A.15 Hooke`s law

When a spring is stretched or compressed from its neutral position by a distance x , it exerts an opposite force decided by the spring constant $k[\text{N/m}]$ (Tipler and Mosca, 2008):

$$F = -kx \quad (0-5)$$

k is considered constant for a limited displacement, and is not valid when the spring material is permanently deformed.

A.16 Definition of pressure

The definition of pressure $p[\text{Pa}]$ is the force F pr unit area A exerted by a volume of gas or fluid on its surroundings (Tipler and Mosca, 2008):

$$p = F/A \quad (0-6)$$

A.17 Heat transfer

The first law of thermodynamics states that “The change in the internal energy of the system $\Delta E_{int} [\text{J}]$ equals the heat transfer into the system Q_{in} plus the work done on the system W_{on} ” (Tipler and Mosca, 2008):

$$\Delta E_{int} = Q_{in} + W_{on} \quad (0-7)$$

Heat is the transport of energy due to a temperature difference dT , hence; heat flows spontaneously from a warmer to a colder reservoir. Conduction of heat, dQ/dt , depends on the ability of the material to conduct heat, which can be described with the thermal conductivity k_T (Tipler and Mosca, 2008):

$$\frac{dQ}{dt} = -k_T A \frac{dT}{dx} \quad (0-8)$$

A is the cross-sectional area and dx is the length over which the heat conducts.

B Calculations

B.1 Gas spring area increase:

$$\text{Area increase factor} = \frac{\text{new area}}{\text{old area}} = \frac{4 \cdot (63\text{mm}/2)^2 \pi - 2 \cdot (25\text{mm}/2)^2 \pi}{2 \cdot (47\text{mm}/2)^2 \pi} = 3,311$$

B.2 Gas spring piston area difference:

$$\text{Piston area diff. factor} = \frac{A_{\text{spring}2}}{A_{\text{spring}1}} = \frac{(63\text{mm}/2)^2 \pi - (25\text{mm}/2)^2 \pi}{(63\text{mm}/2)^2 \pi} = 0,843$$

B.3 Moving mass equivalent

$$\frac{m_S}{m_P} = \frac{v_P(t)}{v_S(t)} \rightarrow \frac{v_P(t) + v_S(t)}{v_S(t)} = \frac{m_S + m_P}{m_P} \quad v_{\text{rel}}(t) = v_P(t) + v_S(t)$$

$$E_{K,TOT} = \frac{1}{2} m_{EQ} v_{\text{rel}}(t)^2 = \frac{1}{2} m_P v_P(t)^2 + \frac{1}{2} m_S v_S(t)^2$$

$$\begin{aligned} \rightarrow m_{EQ} &= m_P \left[\frac{v_{P,\text{max}}}{v_{S,\text{max}} + v_{P,\text{max}}} \right]^2 + m_S \left[\frac{v_{S,\text{max}}}{v_{S,\text{max}} + v_{P,\text{max}}} \right]^2 \\ &= m_P \left[\frac{m_S}{m_S + m_P} \right]^2 + m_S \left[\frac{m_P}{m_S + m_P} \right]^2 \end{aligned}$$

$$= \frac{m_P m_S (m_P + m_S)}{(m_S + m_P)^2}$$

$$\rightarrow m_{EQ} = \frac{m_P m_S}{m_P + m_S}$$

B.4 Hammer amplitude

$$\frac{m_S}{m_P} = \frac{x_P(t)}{x_S(t)} \rightarrow \frac{x_P(t) + x_S(t)}{x_S(t)} = \frac{m_S + m_P}{m_P} \quad x_{rel}(t) = x_P(t) + x_S(t)$$

$$\rightarrow x_S(t) = x_{rel}(t) \frac{m_P}{m_S + m_P}$$

B.5 Maximum stator acceleration

$$\underline{a_{max,S}} = \omega v_{S,max} = \omega v_{rel,max} \frac{m_P}{m_S + m_P} = 2\pi \cdot 100\text{Hz} \cdot \frac{10\text{m}}{\text{s}} \cdot \frac{9\text{kg}}{20\text{kg}} = 2825 \text{ m/s}^2 = \underline{\underline{288g}}$$

B.6 Copper fill factor

3 layers of $N_L = 20$ turns each, with slightly different diameters. Including insulation, the width of the wire was 2,0 mm. Each diameter corresponds to the center of the wire:

$$d_1 = 51.5 \text{ mm} \quad , \quad d_2 = 55.5 \text{ mm} \quad , \quad d_3 = 59.5 \text{ mm}$$

Length of copper wire in one coil:

$$l_C = N_L \pi [d_1 + d_2 + d_3] = 18\pi [51.5 + 55.5 + 59.5] \text{ mm} = 9.42 \text{ m}$$

Copper volume pr coil:

$$V_C = h_c w_c l_C = 2.35 \text{ mm} \cdot 1.85 \text{ mm} \cdot 9.42 \text{ m} = 40.93 \cdot 10^{-6} \text{ m}^3$$

Total air gap volume for the coil, from permanent magnet (\varnothing_{MO}) to back-iron (\varnothing_{BI}), in coil pitch τ_p height:

$$V_G = \pi \cdot \tau_p \left(\left[\frac{\varnothing_{BI}}{2} \right]^2 - \left[\frac{\varnothing_{MO}}{2} \right]^2 \right) = \pi \cdot 47 \text{ mm} \left(\left[\frac{62.0 \text{ mm}}{2} \right]^2 - \left[\frac{46.5 \text{ mm}}{2} \right]^2 \right)$$

$$= 62.08 \cdot 10^{-6} \text{ m}^3$$

Which yields the copper fill factor:

$$FF = \frac{\sum V_C}{V_{AG}} = \frac{40.93 \cdot 10^{-6} \text{ m}^3}{62.08 \cdot 10^{-6} \text{ m}^3} = 0.659$$

B.7 Copper coil DC resistance

Copper resistivity at 25 °C: $\rho_C = 0.01709 \text{ } \Omega\text{mm}^2/\text{m}$ (Dahrentråd, 2011).

Copper wire cross-section $A_{CW} = 2.35 \text{ mm} \cdot 1.85 \text{ mm} = 4.35 \text{ mm}^2$.

Total copper length $l_{TOT} = l_C \cdot n_C = 9.42 \text{ m} \cdot 9 = 84.8 \text{ m}$. Length of the copper wire is adjusted to 85 m for connections.

$$R_{DC} = \rho \cdot l/A = 0.01709 \text{ } \Omega\text{mm}^2/\text{m} \cdot 85 \text{ m} / 4.35 \text{ mm}^2 = 0.334 \text{ } \Omega$$

Adjusting for temperature increase up to 150 °C with the temperature coefficient $3.9 \cdot 10^{-3} \text{ K}^{-1}$:

$$R_{DC,t} = 0.373 \text{ } \Omega \cdot (1 + 125 \text{ K} \cdot 3.9 \cdot 10^{-3} \text{ K}^{-1}) = 0.497 \text{ } \Omega$$

B.8 AC / DC resistance

Referring to Figure 3-4, the geometrical dimensions of the rectangular copper wire for calculating k_C are $w_s = 2.35 \text{ mm}$ and $h = 1.85 \text{ mm}$. Copper resistivity is $\rho_C = 1.709 \cdot 10^{-8} \text{ } \Omega\text{m}$ (Dahrentråd, 2011). Skin depth is given for nominal frequency $f = 100 \text{ Hz}$:

$$\delta_{100 \text{ Hz}} = \sqrt{2\rho_C / \omega\mu_C} = \sqrt{\frac{2 \cdot 1.709 \cdot 10^{-8} \text{ } \Omega\text{m}}{2\pi \cdot 100 \text{ Hz} \cdot 4\pi \cdot 10^{-7} \text{ H/m}}} = 6,58 \text{ mm}$$

Relating R_{DC} and R_{AC} with the factor k_C :

$$k_C = \frac{R_{AC}}{R_{DC}} = \left(\frac{w_s \cdot h}{3 \cdot \delta^2}\right)^2 = \left(\frac{2.35 \text{ mm} \cdot 1.85 \text{ mm}}{3 \cdot (6.58 \text{ mm})^2}\right)^2 = 0.0012$$

B.9 Mid section casing outer surface

$$A = O_{ms} \cdot h_{ms} = \emptyset_C \pi \cdot h_{ms} = 0.075 \text{ m} \cdot \pi \cdot 0.652 \text{ m} = 0.154 \text{ m}^2$$

B.10 Gas spring surface

Cylinder diameter $\emptyset_C = 75 \text{ mm}$

Cylinder length $L_C \approx 80 \text{ mm}$

Flange diameter $\emptyset_F = 95 \text{ mm}$

Total gas spring surface area, including both ends:

$$A_{GSS} \approx 2 \cdot \left[\pi \left(\frac{95 \text{ mm}}{2} \right)^2 + \pi \cdot 75 \text{ mm} \cdot 80 \text{ mm} \right] = 51.9 \cdot 10^{-3} \text{ m}^2$$

B.11 Gas spring max temperature

Assuming a compression factor $5 = V_{max} / V_{min}$, minimum temperature $T_{GS,min} = 300 \text{ K}$, and a polytropic coefficient $\gamma = 1.5$, calculating with

$pV^\gamma = \text{constant}$ and $p^V/T = \text{constant}$:

$$T_{GS,max} = T_{min} \frac{p_{max} V_{min}}{p_{min} V_{max}} = 670 \text{ K}$$

B.12 Stator mass

No.	QTY	Part Number	Description	Mass	Total
1	1	DH2B-P-022-A01	Coil inner support tube	0.141	0.141
2	2	DH2B-P-024-A02	Stator ending support	0.127	0.254
3	24	DH2B-P-023-B01	SMC ring	0.170	4.080
4	1	DH2B-P-025-A01	Sensor coil 6 x 66	0.028	0.028
5	9	DH2B-P-021-A01	Coil 50 x 61.7 x 49.85	0.409	3.681
6	1	DH2B-P-025-B01	Sensor coil 2 X 66	0.009	0.009
7	2	DH2B-P-001-C01	Gas spring chamber	1.573	3.146
8	2	DH2B-P-012-B01	Gas spring cylinder ending plate B	1.140	2.280
9	2	DH2B-P-019-A01	Gasket	0.002	0.004
10	12	ASME B18.21.2M - 5	Helical Spring Lock Washers	0.000	0.000
11	12	ISO 4762 - M5 x 30	Hexagon Socket Head Cap Screw	0.006	0.072
12	4	DH2B-P-016-B01	Gas spring rod seal Stepseal	0.001	0.004
13	2	DH2B-P-017-A01	Gas spring rod seal wear ring	0.001	0.002
14	4	DH2B-P-041-B01	Plug NPT 1 over 4 Hex	0.020	0.080
15	4	DH2B-P-042-B01	Plug M10x1 Hex Head	0.020	0.080
16	4	DH2B-P-043-B01	Plug M16x2 Hex Head	0.070	0.280
17	1	DH2B-P-031-B01	Outer casing	3.000	3.000
18	2	DH2B-P-033-B01	Casing outer flange	0.146	0.292
19	12	ANSI B18.3.1M - M5 x 55	Forged Socket Head Cap Screw	0.010	0.120
20	12	ISO 7092 - ST 5 - 140 HV	Plain washers	0.000	0.000
21	12	ASME B18.21.2M - 5	Lock washer	0.000	0.000
22	12	ISO 4034 - M5	Hexagon nut	0.002	0.024
					17.577

Table B-1: Summing of stator components yielding total stator mass $m_s = 17.58$ kg (Li, 2011b).

B.13 Piston mass

No.	QTY	Part Number	Description	Mass	Total
1	10	DH2B-P-001-A01	Magnet	0.479	4.790
2	9	DH2B-P-003-A01	Magnet separator	0.191	1.719
3	2	DH2B-P-003-B01	Magnet separator with sealing groove	0.239	0.478
4	1	DH2B-P-002-A01	Piston rod M10x652	0.254	0.254
5	2	DH2B-P-E04-A01	PGS3 Sealing set	0.003	0.006
2	2	DH2B-P-013-A01	Gas spring piston	0.285	0.570
3	2	DH2B-P-014-A01	Gas spring piston rod	0.388	0.776
8	2	DH2B-P-018-A01	Gas spring piston seal wear ring	0.001	0.002
10	2	DH2B-P-015-A01	Gas spring piston seal PGS3	0.004	0.008
					8.603

Table B-2: Summing of piston components yielding total piston mass $m_p = 8.60$ kg (Li, 2011b).

B.14 Gas spring pressures, constant amplitude 15.9 mm and frequency 100 Hz

Double chamber length $x_C = 24 \text{ mm} \cdot 2 = 48 \text{ mm}$ yields initial pressure
 $p_0 = 6.0 \text{ MPa} \cdot 2 = 12.0 \text{ MPa}$:

$$k_{\text{comp},48} = \frac{48 \text{ mm} - 15.9 \text{ mm}}{48 \text{ mm}} = 0.66875$$

$$p_{\text{max},48} = \frac{12.0 \text{ MPa}}{(0.66875)^{5/3}} = 23.5 \text{ MPa}$$

Chamber length $x_C = 24 \text{ mm} \cdot 1.5 = 36 \text{ mm}$ yields initial pressure
 $p_0 = 6.0 \text{ MPa} \cdot 1.5 = 9.0 \text{ MPa}$:

$$p_{\text{max},36} = \frac{9.0 \text{ MPa}}{\left[\frac{36 \text{ mm} - 15.9 \text{ mm}}{36 \text{ mm}} \right]^{5/3}} = 23.8 \text{ MPa}$$

B.15 Efficiency calculations, nominal case

Method 1: $\eta_1 = 1 - \left(\frac{i_N^2 \cdot 0.497 + 230}{i_N \cdot u_N} \right) = 1 - \frac{(21 \text{ A})^2 \cdot 0.497 \text{ } \Omega + 230 \text{ W}}{21 \text{ A} \cdot 219 \text{ V}} = 0.9$

Method 2: $\eta_2 = \frac{P_{\text{out}}}{P_{\text{in}}} = \frac{3.3 \text{ kW}}{4.6 \text{ kW}} = 0.72$

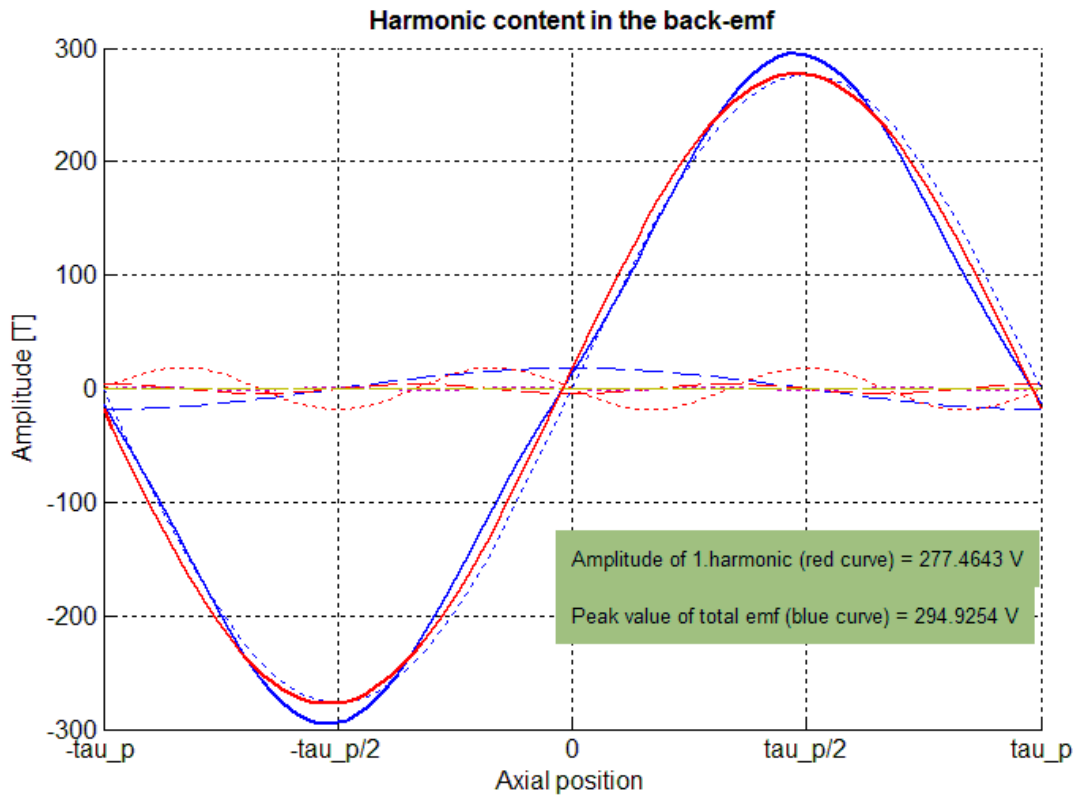
C List of tables and figures

Table 3-1:	26
Table 4-1:	32
Table 4-2:	33
Table 4-3:	36
Table 4-4:	38
Table 4-5:	46
Table 4-6:	58
Table 5-1:	71
Table B-1:	92
Table B-2:	92

Figure 3-1:	17
Figure 3-2:	18
Figure 3-3:	19
Figure 3-4:	21
Figure 3-5:	22
Figure 3-6:	24
Figure 3-7:	26
Figure 3-8:	28
Figure 4-1:	31
Figure 4-2:	35
Figure 4-3:	35
Figure 4-4:	39
Figure 4-5:	40
Figure 4-6:	41
Figure 4-7:	43
Figure 4-8:	44
Figure 4-9:	45
Figure 4-10:	50
Figure 4-11:	51
Figure 4-12:	52
Figure 4-13:	53
Figure 4-14:	54
Figure 4-15:	55
Figure 4-16:	55
Figure 4-17:	56
Figure 4-18:	57
Figure 5-1:	63
Figure 5-2:	65
Figure 5-3:	68
Appendix A-1:	86
Appendix D-1:	95
Appendix D-2:	Error! Bookmark not defined.
Appendix D-3:	Error! Bookmark not defined.
Appendix D-4:	Error! Bookmark not defined.

D Figures

D1. Induced voltage



Appendix D.1 (D-2): Distribution of induced voltage in the coils (Jacobsen, 2011b).

E Script

E.1 Analytical script of 2B motion by Grinde (2011)

```

//////
m1=8;
m2=45 ;
k1=5e6; // Combined linear stiffness of the gas springs
b1=0.0;

mstar=m1*m2/(m1+m2);
f_estimate=1/(2*pi)*sqrt(k1/mstar)
////////////////////////////////////
// z(1) is the outer mass displacement
// z(2) is the inner mass displacement
// coordinate system

function zdot=ff(t, z)
    x1=z(1),
    x2=z(2),
    v1=z(3),
    v2=z(4),
    zdot(1)=v1,
    zdot(2)=v2,
    zdot(3)=(1/m1)*(-b1*v2-k1*x2),
    zdot(4)=(1/m2)*(-m2*zdot(3)+b1*v2+k1*x2)
endfunction
////////////////////////////////////
sample_rate=30000;
t = 0:1/sample_rate:0.1;
N=size(t, '*'); //number of samples
////////////////////////////////////
// Solving
Amp=0.5
[y]=ode("rkf",[Amp;-((Amp)+(Amp)*(m1/m2));0;0],0,t,ff);
//[y]=ode("rkf",[ (m2/m1)*Amp;-Amp;0;0],0,t,ff);
z1=y(1,:);
z2=y(2,:);
z3=z1+z2;
v1=y(3,:);
v2=y(4,:);
v3=v1+v2

```

```
acc1=diff(v1)
acc2=diff(v2)
clf()
subplot(2,3,1)
//plot(t,[z1',z2',z3'])
plot(t,[z1',z3'])
legend("z1","z3")

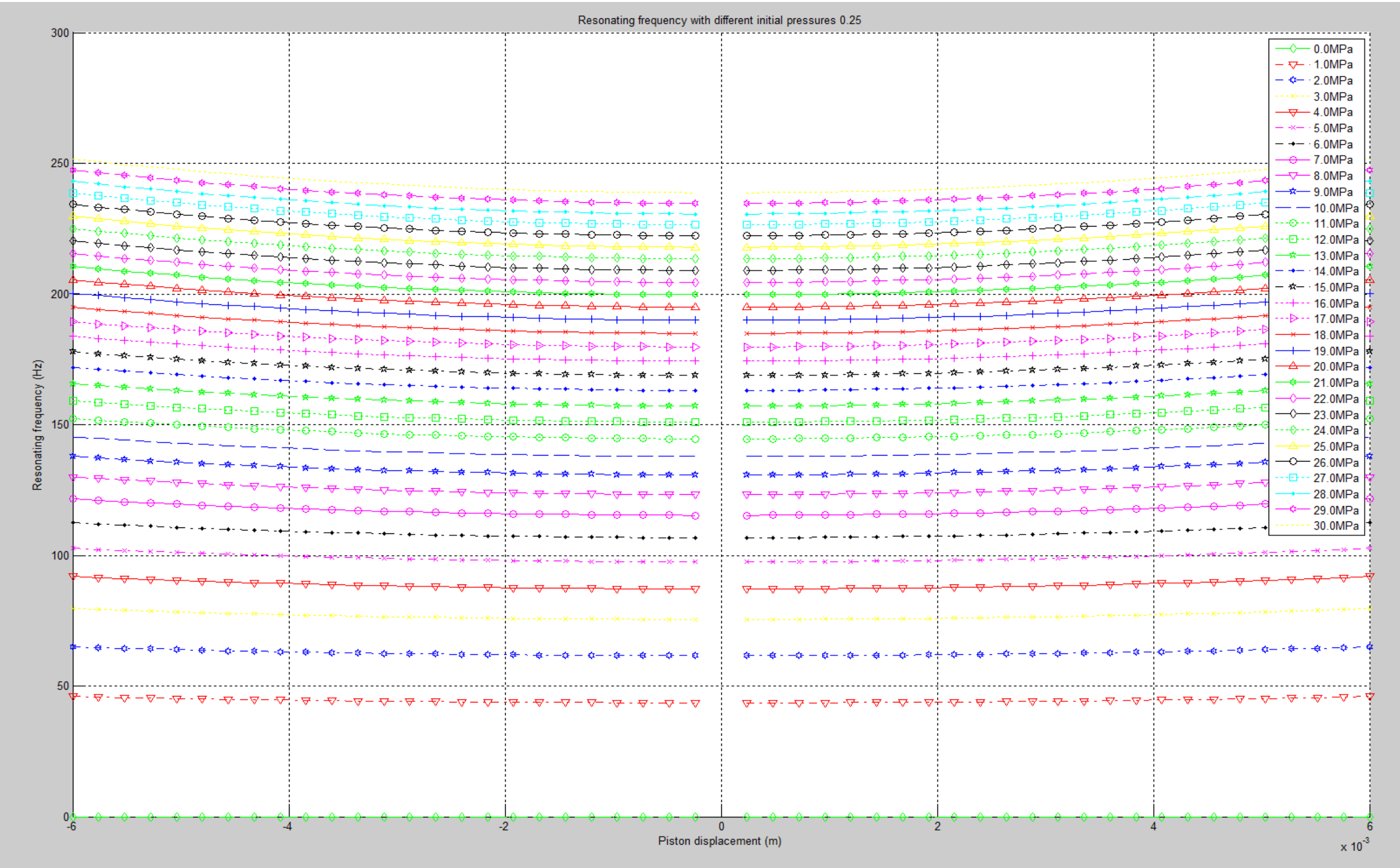
y=fft(z1)
//the fft response is symmetric we retain only the first N/2 points
f=sample_rate*(0:(N/2))/N; //associated frequency vector
n=size(f, '1')
//clf()
subplot(2,3,2)
plot2d(f,abs(y(1:n)))

frange=find(f>20); // Extract frequencies above 20 Hz
displacementdata=abs(y(1:n));
localpeak=max(displacementdata(frange));
maxFreq=f(find(localpeak==displacementdata))

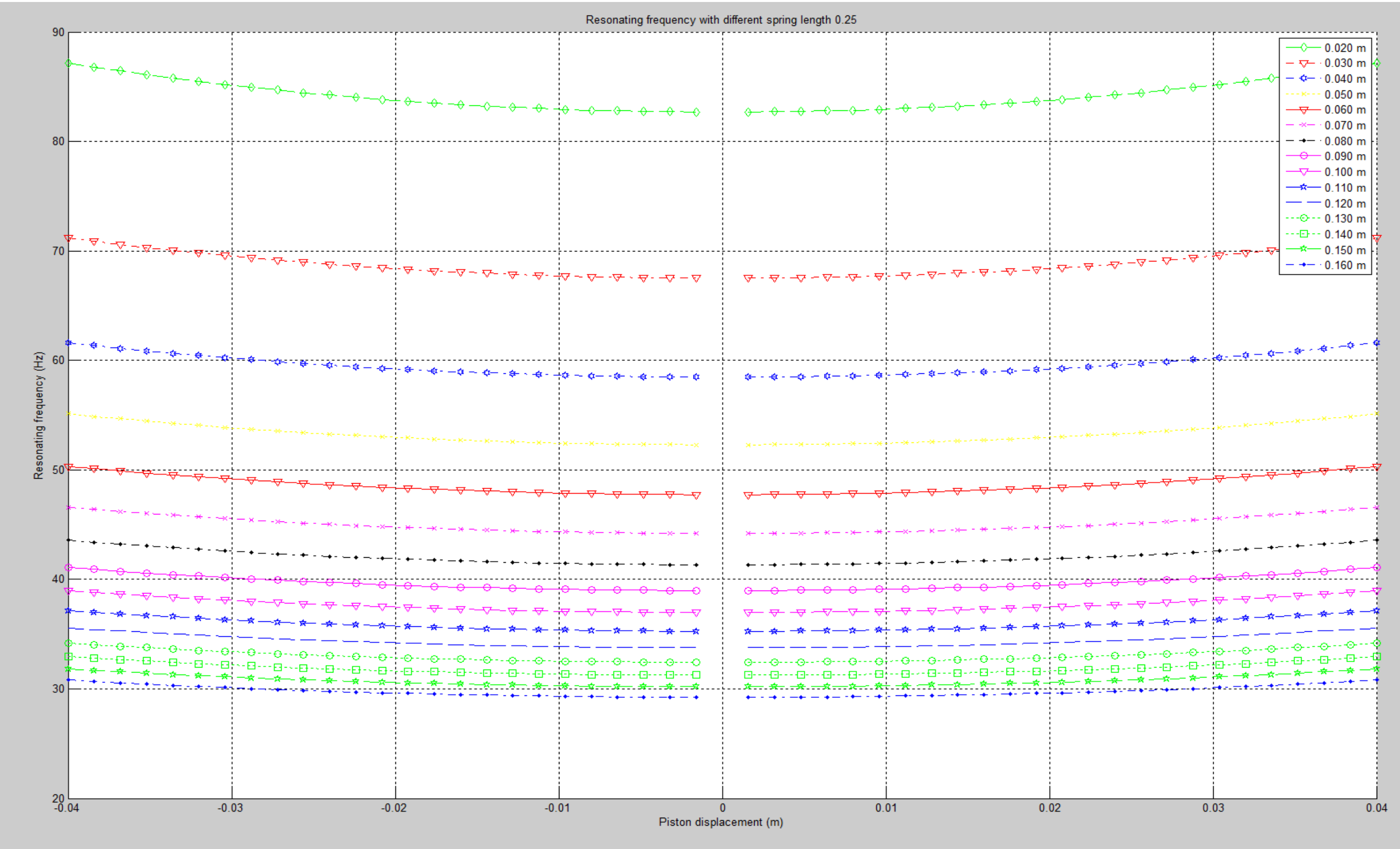
////////////////////////////////////
//
fdiff=maxFreq-f_estimate

KE1=v1^2*0.5*m1;
KE2=v2^2*0.5*m2;
KE3=v3^2*0.5*m2;
subplot(2,3,3)
plot2d(t,[v1',v3'])

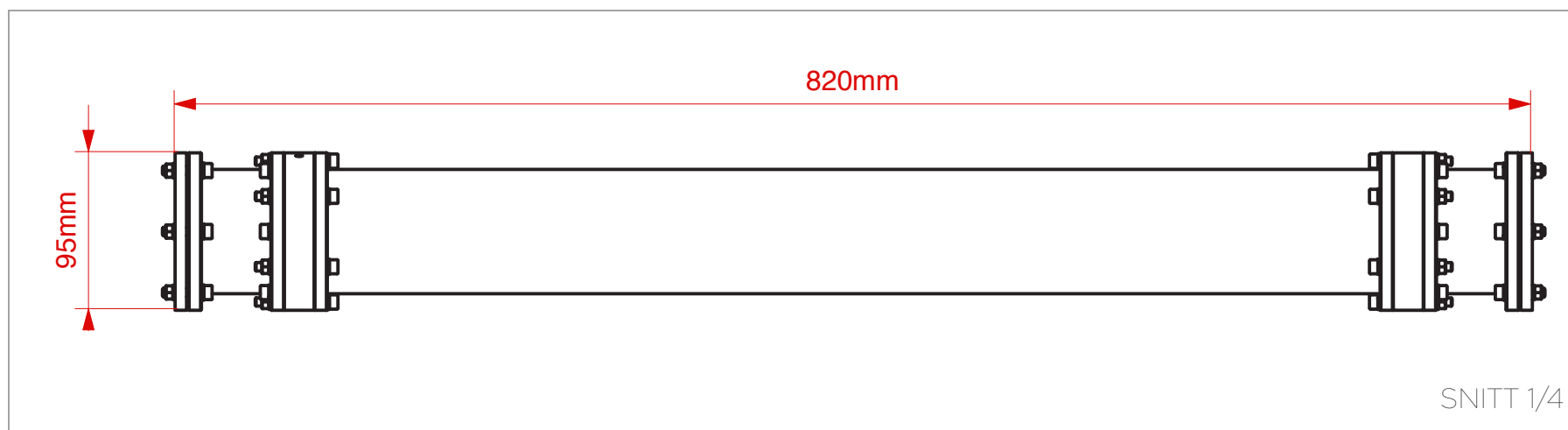
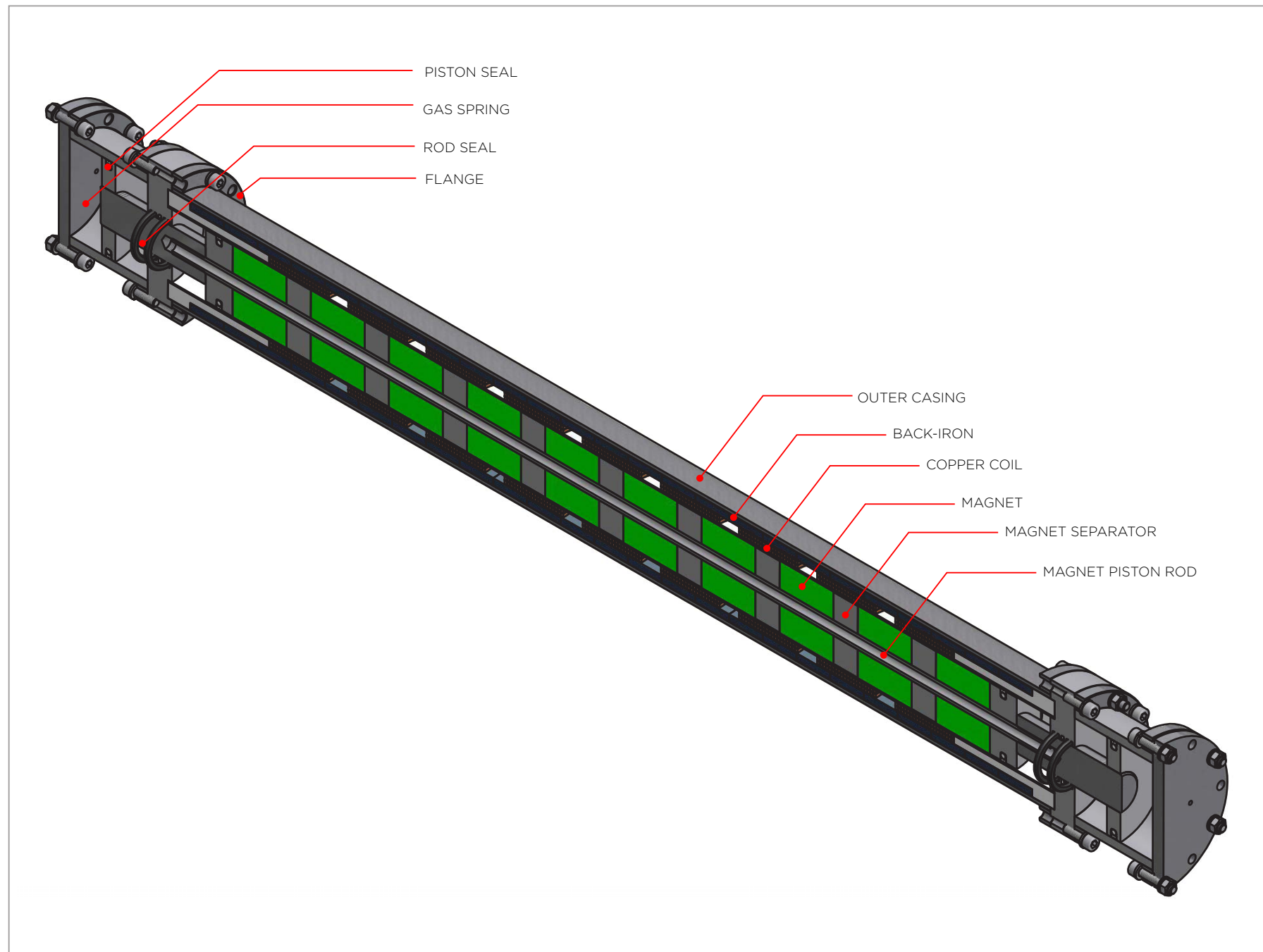
subplot(2,3,4)
plot2d(z1,KE1)
legend("KE outer mass ")
subplot(2,3,5)
plot2d(z2,KE2)
legend("KE inner mass, local to outer mass coordinates")
subplot(2,3,6)
plot2d(z3,KE3)
legend("KE inner mass, global coordinates")
```



Appendix D.2: Simulation results: Resonance frequency plotted for different initial gas spring pressures (Li, 2011a). The chamber length is 24 mm. An initial pressure of 6.0 MPa yields a resonating frequency of > 100 Hz.



Appendix D.3: Simulation results: Resonance frequency plotted for different gas spring chamber lengths (Li, 2011a). Increasing chamber length by the factor 2 yields a decrease in resonance frequency of $\sim\sqrt{2}$. This can be compensated for by increasing initial pressure by the factor 2.



2B DRILL HAMMER PROTOTYPE

Technical specifications - Nominal values

Length	L_{2B}	820 mm
Diameter	\varnothing_{2B}	95 mm
Hammer weight	m_{2B}	26.2 kg
Hole size diameter	\varnothing_h	32 mm
Hammer frequency	f_N	100 Hz
Hammer amplitude	$x_{S,max}$	5.2 mm
Gas spring initial pressure	p_0	6.0 MPa
Gas spring maximum pressure	p_{max}	36.7 MPa
Electric frequency	f_{el}	100 Hz
Current	I_n	21 A
Voltage	U_n	219 V
Electric power input	P_{in}	4.6 kW
Mechanical power output	P_{out}	3.3 kW
Motor efficiency	η	0.7 - 0.9
Energy per blow	E_b	33 J
Ambient temperature	T_a	< 25 °C